

**ÇUKUROVA UNIVERSITY
INSTITUTE OF NATURAL AND APPLIED SCIENCES**

PhD THESIS

Ahmet AYDIN

**DEVELOPMENT OF A NEW EXTERNAL FIXATOR SYSTEM FOR
AUTOMATED BONE FIXATION: THEORY AND IMPLEMENTATION**

DEPARTMENT OF ELECTRICAL AND ELECTRONICS ENGINEERING

ADANA, 2015

ÇUKUROVA UNIVERSITY
INSTITUTE OF NATURAL AND APPLIED SCIENCES

**DEVELOPMENT OF A NEW EXTERNAL FIXATOR SYSTEM FOR
AUTOMATED BONE FIXATION: THEORY AND IMPLEMENTATION**

Ahmet AYDIN

PhD THESIS

DEPARTMENT OF ELECTRICAL AND ELECTRONICS ENGINEERING

We certify that the thesis titled above was reviewed and approved for the award of degree of the Doctor of Philosophy by the board of jury on 06/08/2015.

.....
Asst. Prof. Dr. M. Kerem ÜN
SUPERVISOR

.....
Prof. Dr. İ. Deniz AKÇALI
MEMBER

.....
Assoc. Prof. Dr. Mustafa ORAL
MEMBER

.....
Asst. Prof. Dr. Serdar YILDIRIM
MEMBER

.....
Asst. Prof. Dr. Mehmet K. BARAN
MEMBER

This PhD Thesis is written at the Department of Institute of Natural And Applied Sciences of Çukurova University.

Registration Number:

Prof. Dr. Mustafa GÖK
Director
Institute of Natural and Applied Sciences

Not: The usage of the presented specific declarations, tables, figures, and photographs either in this thesis or in any other reference without citations is subject to "The law of Arts and Intellectual Products" number of 5846 of Turkish Republic

ABSTRACT

PhD THESIS

DEVELOPMENT OF A NEW EXTERNAL FIXATOR SYSTEM FOR AUTOMATED BONE FIXATION: THEORY AND IMPLEMENTATION
--

Ahmet AYDIN

**ÇUKUROVA UNIVERSITY
INSTITUTE OF NATURAL AND APPLIED SCIENCES
DEPARTMENT OF ELECTRICAL AND ELECTRONICS ENGINEERING**

Supervisor: Asst. Prof. Dr. Mustafa Kerem ÜN
Year:2015, Pages:127

Jury: Asst. Prof. Dr. Mustafa Kerem ÜN
: Prof. Dr. İbrahim Deniz AKÇALI
: Assoc. Prof. Dr. Mustafa ORAL
: Asst. Prof. Dr. Serdar YILDIRIM
: Asst. Prof. Dr. Mehmet Kadir BARAN

In the field of orthopedics, external fixators are widely used for treatment of extremity deformities. However, the adjustment of such a system is usually done by hand based on the experience of the clinician. Computer-assisted systems exist where treatment is planned with a software after processing radiological images. Such system takes some radiological and clinical data as input and calculates the configuration of the external fixator that will align the bone fragments to their anatomical axes. Yet, existing computer-assisted systems have various limitations and constraints. In this study, a new automatized system and an associated graphical user interface have been developed, that will minimize the human intervention and the related error, simplify the utilization of the external fixators and improve the quality of the service. In particular, methods have been proposed to complete the bone images blocked by the parts of the fixators and to automatically locate the fixator rings on the image. Furthermore, a new fixator that can be configured to different settings and its mathematical theory have also been presented in this work. The potential use and advantages of this new design are described in detail.

Key Words: External fixator, medical image processing, inverse kinematics, ellipse fitting, orthopedics

ÖZ

DOKTORA TEZİ

OTOMATİK KEMİK DÜZLETME İÇİN YENİ BİR HARİCİ FİKSATÖR SİSTEMİNİN GELİŞTİRİLMESİ: TEORİ VE UYGULAMASI

Ahmet AYDIN

**ÇUKUROVA ÜNİVERSİTESİ
FEN BİLİMLERİ ENSTİTÜSÜ
ELEKTRİK ELEKTRONİK MÜHENDİSLİĞİ BÖLÜMÜ**

Danışman: Yrd. Doç. Dr. Mustafa Kerem ÜN
Yıl:2015, Sayfa:127

Juri: Yrd. Doç. Dr. Mustafa Kerem ÜN
: Prof. Dr. İbrahim Deniz AKÇALI
: Doç. Dr. Mustafa ORAL
: Yrd. Doç. Dr. Serdar YILDIRIM
: Yrd. Doç. Dr. Mehmet Kadir BARAN

Ortopedi alanında, kol ve bacak kırıklarının tedavisinde harici fiksatorler yaygın olarak kullanılmaktadır. Fakat bu sistemlerin kullanımı genellikle tecrübeli doktor veya teknisyenler tarafından manuel olarak yapılmaktadır. Bilgisayar destekli sistemler, radyolojik görüntülerin işlenerek tedavi planlamasının yapıldığı yazılımlarla kullanılabilir. Bu tarz sistemler, giriş olarak radyolojik ve klinik verileri alarak, kemik parçalarını anatomik eksenlerine hizalayacak harici fiksator kurgusunu hesaplamaktadır. Mevcut sistemler kullanım konusunda değişik limit ve kısıtlamalara sahiptir. Bu çalışmada, insan müdahalesini ve buna bağlı hataları azaltacak, mevcut sistemlerdeki bazı kısıtlamaları giderek harici fiksatorün kullanımını kolaylaştıracak ve sunulan hizmetin kalitesini arttıracak, otomasyon düzeyi artırılmış yeni sistem ve ilgili grafik arayüzü geliştirilmiştir. Özellikle, fiksatorün metalik yapısından kaynaklanan kemiklerdeki görüntü kaybını giderecek ve fiksator halkalarının otomatik olarak tespit edilmesinin sağlayacak yöntemler önerilmiştir. Buna ek olarak, değişik konfigürasyonlarda kurgulanabilen yeni bir harici fiksator ve bu fiksatorün matematik modeli sunulmuştur. Bu yeni fiksatorün kullanım potansiyeli ve avantajları detaylarıyla verilmiştir.

Anahtar Kelimeler: Harici fiksator, medikal görüntü işleme, ters kinematik, eliptik uydurma, ortopedi

ACKNOWLEDGMENTS

PhD was a long journey and my chance was having great people around during this period.

First of all, I would like to thank my supervisor Assist. Prof. Dr. M. Kerem ÜN for his support, patience and guidance. He is a great role model for me with his academic and personal life. I had the chance of meeting Prof. Dr. İbrahim Deniz AKÇALI in the very beginning of my academic life and learned a lot from him. He has a big impact on my academic background and I am grateful to him for that. I am thankful to Assoc. Prof. Dr. Mustafa ORAL for his guidance and support both in my academic carrier and personal life. I also want to thank my committee members Assist. Prof. Dr. Mehmet Kadir BARAN and Assist. Prof. Dr. Serdar YILDIRIM for their valuable input.

This thesis is prepared as a part of a scientific project and I want to thank all project members for their contribution during this time.

I want to thank to my parents for their endless support in every stage of my life. I want to thank to my brothers and sister for always being there for me.

I am grateful to my wife Emine for her patience, support and love. The road to PhD degree has many ups and downs. She was always there to keep me on my feet in difficult times. Life is meaningful with her.

The financial support of the Scientific and Technological Research Council of Turkey (TÜBİTAK) during my Ph.D. is gratefully acknowledged.

CONTENTS	PAGE
ABSTRACT	I
ÖZ	II
ACKNOWLEDGMENTS	III
CONTENTS	IV
LIST OF TABLES	VIII
LIST OF FIGURES	X
1. INTRODUCTION.....	1
1.1. Background and Motivation	1
1.2. Overview of Ring Fixator Systems	5
1.3. Contributions of the Thesis.....	11
1.4. Thesis Outline.....	11
2. GOUGH – STEWART PLATFORM AS EXTERNAL FIXATOR.....	13
2.1. Inverse Kinematic Studies of the Gough – Stewart Platform.....	13
2.1.1. Derivation of 3D Geometric Parameters from AP and L Images	13
2.1.2. Derivation of Transformations and Strut Length Calculation.....	17
2.2. Extending the Theory to Oblique View Case.....	23
2.2.1. Direct Theoretical Data Transformation	24
2.2.1.1. Relationship between L and L' – Views.....	24
2.2.1.2. Relationship between AP and AP' – Views	27
2.2.1.3. Combining the Data Obtained from AP' and L'	29
2.2.1.4. Obtaining qx and qy	31
2.2.2. Using Point Data to Transfer Oblique Data to Normal.....	34
2.2.3. Graphical User Interface to Test the Oblique View Theory	37
3. A NOVEL EXTERNAL FIXATOR: THE LAMBDA FIXATOR	41
3.1. Motivation for the New Design	41
3.2. Inverse Kinematic Studies of the Lambda Fixator	41
3.2.1. Development of the Mathematical Model.....	42
3.2.2. Calculation of Strut and Rod Lengths	45

3.2.3. The Graphical User Interface for Inverse Kinematic Algorithm Calculations of Lambda Fixator	48
3.2.4. Test of the Algorithm and GUI	50
4. COMPLETION OF BONE IMAGE	53
4.1. Introduction	53
4.2. Segmentation of the Bone and the External Fixator	54
4.3. Removing the Fixator in the X-ray Image	60
4.4. Combining Bone Parts through Convex Hull	62
4.5. Alignment with Pre-operation Bone Fragments	63
4.5.1. Alignment using Grid Search	63
4.5.2. Alignment using Bone Axes	65
5. LOCATING THE DISTAL RING IN THE FIXATOR IMAGE	69
5.1. Introduction	69
5.2. Finding Interpolation Points on Distal Ring	69
5.3. Ellipse Fitting without Major Axis Constraint	71
5.3.1. Direct Fitting Method	71
5.3.2. Fitting with Least Squares Minimization	73
5.3.3. Testing of the Direct Ellipse Fitting Algorithm	74
5.3.4. Testing of the Least Squares Ellipse Fitting Algorithm	75
5.4. Ellipse Fitting with Major Axis Constraints	77
5.4.1. Constrained Direct Fitting	78
5.4.2. Constrained Fitting with Least Squares Minimization	79
5.4.3. Test of the Constrained Ellipse Fitting Algorithms	81
5.5. Manuel Fitting: Moving Ellipse	83
6. INTEGRATED GRAPHICAL USER INTERFACE	85
6.1. Preparation for Measurement	86
6.2. Measurement Procedure	87
6.3. Helper Functions and Tools	93
6.4. Complete System Test – 1	94
6.4.1. Preparation of the Fixator System	94
6.4.2. Preparation of the X-ray images	95

6.4.3. Measurement of X-ray Parameters.....	96
6.4.4. Obtaining the Clinical Data.....	98
6.4.5. Calculating the System Configuration and Test of the GUI Results.....	100
6.5. Complete System Test – 2.....	103
7. CONCLUSION	109
7.1. Concluding Remarks and Discussion.....	109
7.2. Future Research	111
REFERENCES.....	113
CURRICULUM VITAE	119
APPENDIX A: COMMON IMAGE PROCESSING TOOLS	123
A.1. Contrast Limited Adaptive Histogram Equalization	123
A.2. Canny Edge Detection Algorithm	124
A.3. Morphological Erosion	125
A.4. Removing Small Objects in a Binary Image	127

LIST OF TABLES**PAGE**

Table 5.1. Parameters of the source ellipse and the ellipses obtained as a result of the unconstrained and constrained least square minimization fitting algorithms.	82
Table 6.1. Connection configuration for module 1	99
Table 6.2. Connection configuration for module 2	99
Table 6.3. Connection configuration for module 3	100

LIST OF FIGURES	PAGE
Figure 1.1. Medical naming convention of the planes (Bridwell, 2010).	2
Figure 1.2. Two main types of external fixators. (a) Pin: Unilateral Fixator and (b) Ring: Illizarov Fixator	3
Figure 1.3. Taylor Spatial Frame (Smith&Nephew, 2015).....	4
Figure 1.4. Taylor Spatial Frame (Taylor et al., 1999)	6
Figure 1.5. The rods used by Koo et al. (2002).....	6
Figure 1.6. Adam Frame	8
Figure 1.7. SUV external fixator (Solomin et al., 2015).....	8
Figure 1.8. The locking of the struts to the rings in TrueLok-Hex.	9
Figure 1.9. Rapid adjustment of the struts in TrueLok-Hex.	9
Figure 1.10. External fixator designed by Karidis (2009).....	10
Figure 2.1. View – position relation of the rod	14
Figure 2.2. (a) Lateral and (b) Anterior – Posterior views of the rod	14
Figure 2.3. The biomechanical system and location of the coordinate systems.	18
Figure 2.4. View – position relations of the biomechanical system for (a) <i>AP</i> and (b) <i>L</i> views.	18
Figure 2.5. Relative angular orientation of the rings and the bone fragments	19
Figure 2.6. Angular positions of the joints at (a) the proximal and (b) the distal rings.	19
Figure 2.7. Flowchart of the mathematical model	24
Figure 2.8. Lateral view and <i>L'</i> - view	25
Figure 2.9. <i>L'</i> - view	26
Figure 2.10. <i>AP</i> and <i>AP'</i> views	27
Figure 2.11. <i>AP'</i> view.....	28
Figure 2.12. <i>L'</i> view and proximal ring plane	31
Figure 2.13. <i>AP'</i> view and proximal ring plane	33
Figure 2.14. View – Position relations and reference Points	35
Figure 2.15. Data creation and algorithm test GUI.....	38
Figure 3.1. Lambda fixator.....	42

Figure 3.2.	(a) Lambda module and (b) naming convention used during calculations.	43
Figure 3.3.	Eight different connection types.	44
Figure 3.4.	Graphical User Interface for inverse kinematic calculations of lambda fixator	49
Figure 3.5.	Connection case selection	49
Figure 3.6.	Configuration for initial (a) and final (b) positions of the lambda fixator.....	50
Figure 3.7.	Test data and results.....	51
Figure 4.1.	Flowchart of the bone image completion procedure	54
Figure 4.2.	Input image used to segment bone from soft tissue.....	56
Figure 4.3.	Input image used to segment the external fixator from bone and soft tissue.	56
Figure 4.4.	Results for segmentation of the bone from the soft tissue. The numbers indicate the test method.....	57
Figure 4.5.	Results for segmentation of the fixator from rest of the image. The numbers indicate the test method.....	58
Figure 4.6.	Interactive threshold selection in the GUI.	59
Figure 4.7	(a) The original input image and (b) the segmented fixator (image inverted for better visualization).....	60
Figure 4.8.	(a) The image after filtering the fixator and (b) the result of the morphological erosion (images are inverted for better visualization).	61
Figure 4.9.	Result of the small object removal algorithm.	61
Figure 4.10.	(a) Pixel clusters of proximal bone fragment and (b) the associated convex hull.....	62
Figure 4.11.	(a) The bone fragment segmented from pre-operation X-ray image and (b) the result of the hole filling algorithm.....	63
Figure 4.12.	Result of the bone alignment process. The contour and center line obtained from pre-operation X-ray image is drawn on the fixator system image after alignment process (blue line).....	65

Figure 4.13	The (a) pre-operative and (b) post-operative images used	66
Figure 4.14	The bone fragment axes and osteotomy path drawn on the (a) pre-operative and (b) post-operative images.	67
Figure 4.15	(a) Proximal and (b) distal fragments of the pre-operative image	67
Figure 4.16	The edges of the aligned fragments drawn on the post-operative image.....	68
Figure 5.1.	(a) Input image for ellipse fitting and (b) the output after Otsu Thresholding	70
Figure 5.2.	(a) The thresholded image after morphological erosion (b) and after the removal of the pixel clusters with area larger than 50 pixels.	70
Figure 5.3.	The obtained data points are shown with red dots.....	71
Figure 5.4.	Result of the direct ellipse fitting method. By clicking on the screen, random points are created (red dots). An ellipse is fitted on these points (blue curve).	74
Figure 5.5.	The result of the direct ellipse fitting method applied on reference points (shown in red) obtained at the image processing stage from (a) Gough-Stewart Platform External Fixator and (b) Lambda Fixator.....	75
Figure 5.6.	The result of the least square fitting method without constraints. The source ellipse is given in blue line, the guessed ellipse in green line and noisy data point in blue dots.	76
Figure 5.7.	The result of the least square fitting method applied on reference points (shown in red) obtained at the image processing stage from (a) Gough-Stewart Platform External Fixator and (b) Lambda Fixator.....	77
Figure 5.8.	The reference point indicated with the arrow is removed.	78
Figure 5.9.	The result of the ellipse fitting without the rightmost reference points.....	78
Figure 5.10.	Semi major axis constrained direct ellipse fitting applied to the X-Ray image.	81

Figure 5.11. The visual result of the least square fitting method. The blue ellipse is the source ellipse used to create data points. The green ellipse is obtained without <i>ra</i> constraints, and the red ellipse is obtained with <i>ra</i> constraints.	82
Figure 5.12. The result of the least square fitting method with semi major axis constraint.....	83
Figure 5.13. Ellipse created on the image (a) and its position after manual fitting (b).....	84
Figure 6.1. The GUI with its items numbered.....	85
Figure 6.2. Rotate menu	86
Figure 6.3. Parameters measured from (a) Anterior – Posterior and (b) Lateral X-ray images.....	87
Figure 6.4. Proximal ring axis point selection	88
Figure 6.5. Virtual and actual proximal ring axes and <i>z</i> –axis.....	89
Figure 6.6. Distal Ring: selected points (1, 2, 3, 4) and obtained ellipse with <i>w</i> –axis of the <i>uvw</i> –coordinate system.	90
Figure 6.7. Bone Axis: Selected points (1, 2) and the resulting bone fragment axis	91
Figure 6.8. Measurement screen.	92
Figure 6.9. Dialog window to add text.....	93
Figure 6.10. Lambda fixator with an artificial bone	95
Figure 6.11. X-ray images of the fixator system from (a) <i>AP</i> and (b) <i>L</i> views.....	96
Figure 6.12. Measurement GUI with measured <i>AP</i> X-ray image	97
Figure 6.13. Measurement GUI with measured <i>L</i> X-ray image.....	97
Figure 6.14. Axial image of the system.	98
Figure 6.15. Calculation GUI with input data entered and the results are calculated.	101
Figure 6.16. System configuration after the strut lengths are set to their final values as obtained from the GUI.	102
Figure 6.17 Initial configuration of the system for Test -2.	103
Figure 6.18 Measured <i>AP</i> image of Test -2	104

Figure 6.19	Measured L image of Test -2.....	104
Figure 6.20	Axial image of the system for Test -2.....	105
Figure 6.21	The measurement data and the calculation results for Test -2.....	106
Figure 6.22	Result of the Test – 2: the aligned position of the system	107
Figure A.1.	Redistributing the clipped histogram values among all the bins at CLAHE, (Wikipedia, 2015).....	123
Figure A.2.	(a) Input image taken from Transmission Electron Micrograph and (b) after applying CLAHE with 50 block size 256 histogram bins and 2.5 maximum slope (Saalfeld, 2010).	124
Figure A.3.	Different structure elements with their origin is in the center. (a) 3x3 Square, (b) 3x3 Star and (c) 7x7 Disk structure element.....	126
Figure A.4.	(a) Binary input image and (b) the output after erosion with 3x3 Square structure element (Robert Fisher, 2004)	127

1. INTRODUCTION

1.1. Background and Motivation

External fixators are extensively used in orthopedics in order to reduce fractures or correct bone deformities. They consist of a strut or a group of struts, brought together to construct an extensive frame which is then connected externally to the bone fragments in order to stabilize them (Seligson and Pope, 1982).

External fixators are firstly used by Hippocrates nearly 2500 years ago for treatment of fractures and then popularized with studies of Malgaigne, Parkhill, and Della Mano (Parkhill, 1983; Sisk, 1983; Eren and Eralp, 1999). Due to improper usage of the external fixators and consequently obtained poor clinical results, external fixation has lost its popularity in the 60's. As the scientific understanding about the process of fixation grew in time, the clinical process had been more refined and proper mechanical design and better material technologies had been utilized. As a result, the external fixators have regained its popularity in 70's. (Behrens, 1982; Hughes and Sauer, 1982; Pope and Evans, 1982; Seligson and Pope, 1982; Fernández, 1985; Paul, 2003; Paley, 2015)

Bone fractures are common occurrences that are treated by conventional means in most cases. Sometimes, a fracture can be complex involving multiple fragments or a problematic physiological location. In those instances, an external fixator may be necessary for a proper treatment.

In the treatment of bone deformities, a fixation system is absolutely necessary. Bone deformities are pathologies where long bones (typically femur, tibia, and humerus) are not in their anatomically natural shape. Their origin can be congenital (i.e. from birth), developmental (i.e. appears during childhood development) or trauma-related (due to the improper healing of a fracture). Patients with bone deformities usually have difficulties in standing, walking or using their limbs, and have a reduced life quality. The deformities may be classified as *translational*, *rotational*, *mal-union* or *non-union*. Complex cases, where more than one type of deformity are simultaneously present, are also possible (Aglietti and Buzzi, 2002). Deformities can

be situated in different planes of the human body such as *axial*, *sagittal*, or *coronal* planes (Figure 1.1). To treat deformities, external fixators are usually used after performing an *osteotomy* (removal of some bone material). After the osteotomy, pins are attached to the bone fragments that are connected to the external fixator. Therefore, by manipulating the external fixator, the position of the bone fragments can be controlled. Hence, while the bone fragments heal during the treatment, their relative positions are adjusted in time to stimulate bone growth and allow the correction of the deformity.

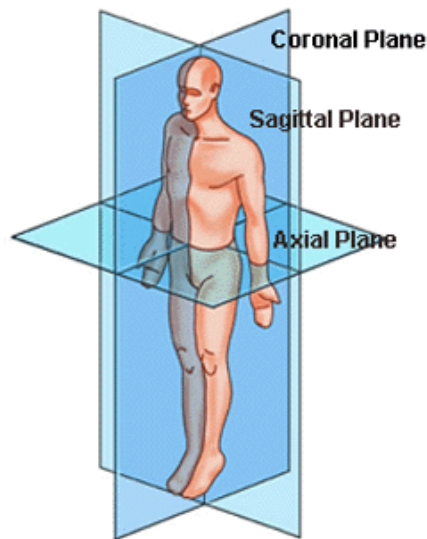


Figure 1.1. Medical naming convention of the planes (Bridwell, 2010).

There are different types of external fixators with differing usages in orthopedics. The external fixators are divided into two main groups as *pin* and *ring* (or circular) fixators (Figure 1.2). There are three types of pin external fixators; *unilateral*, *bilateral* and the combination of the unilateral and bilateral fixators in a three dimensional configuration (Paley, 2002). Linear external fixators are used for one-plane deformities and stabilizing the bone fragments in case of fracture.

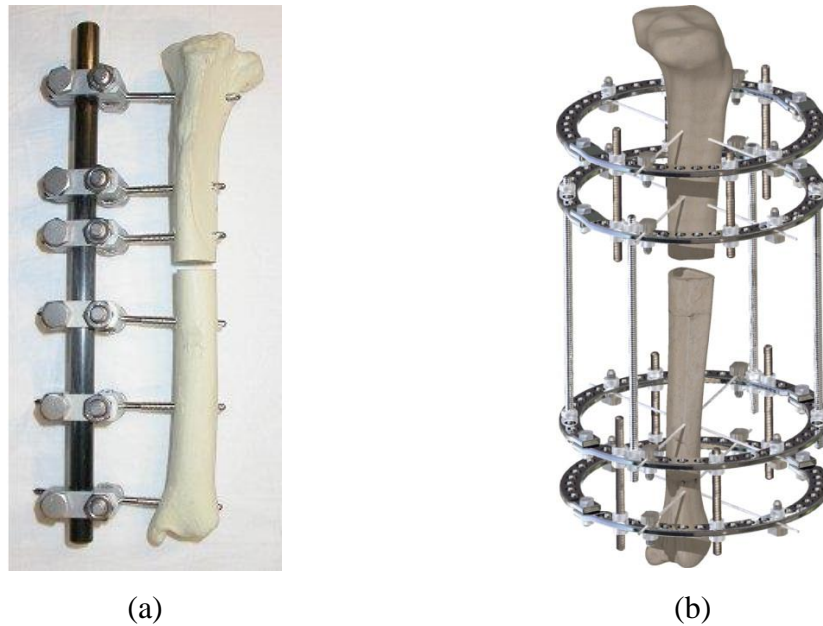


Figure 1.2. Two main types of external fixators. (a) Pin: Unilateral Fixator and (b) Ring: Illizarov Fixator

The ring fixator, invented by Ilizarov, is considered a breakthrough in the field (Ilizarov, 1992; Çakmak, 1999). Ilizarov ring fixators can be used not only for stabilizing the bone fragments in a fracture, but also for the treatment of angular deformities and limb-length discrepancies (Spiegelberg et al., 2010).

The Taylor Spatial Frame (TSF) is the most commonly used ring external fixator (Taylor et al., 1999; Taylor and Taylor, 2000). The system consists of two rings connected to each other with 6 adjustable telescopic struts at attachment points (Figure 1.3). Each strut length can be independently changed relative to the rest of the system. Therefore the bones can be moved with six degree of freedom relative to each other (Product document, (Smith&Nephew, 2015)). Such a system has two main advantages. First, the six degrees of freedom of the system gives the surgeon the flexibility to treat different types of deformities. Moreover, the system is strong enough to support the body weight of the patient, such that the patient retains his/her mobility to some extent during treatment.

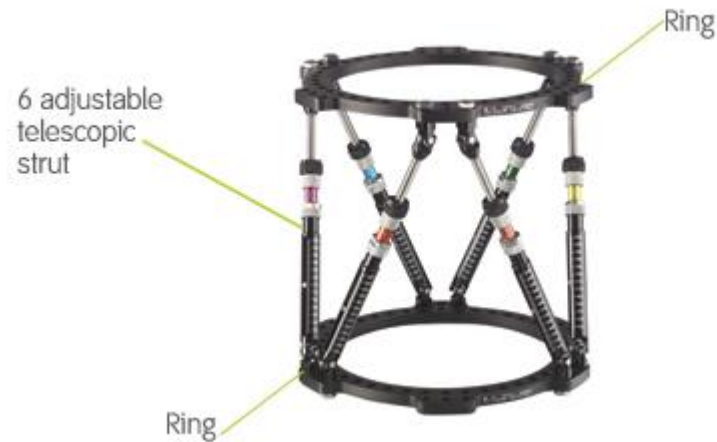


Figure 1.3. Taylor Spatial Frame (Smith&Nephew, 2015)

The relationship between the strut lengths and the relative position of the rings (and therefore of the bone fragments) is rather complex such that a mathematical model is required for the reliable use of Taylor-like ring fixators. The related mathematical model takes some input data measured on the X-Ray images and provides a prescription in terms of a timeline for the strut lengths. Once this prescription is followed, the relative position of the bone fragments evolves according to the desired treatment. The calculations involved in the mathematical model are not straightforward. Therefore, external ring fixators, especially the ones similar to TSF, typically come with an accompanying software, where parameters, required for the mathematical model, are collected by processing the X-Ray images of the patient digitally, calculations are performed according to the implemented mathematical theory and the results are provided to the user.

When setting up a fixator, there may be physiological constraints which must be taken into consideration by the surgeon. The surgeon would avoid damaging critical tissues such as major nerves or arteries. Similarly, the mobility of the patient (which is usually desirable for proper treatment) should not be disturbed much by the presence of fixator. All these concerns affect the way a fixator is attached to the patient by the surgeon.

On the other hand, most of the computer-assisted, Taylor-like fixator systems impose different physical constraints on the usage of the frame. For example, in TSF, both bone fragments must be attached perpendicular to the ring plane. Also, the struts

must be connected to predefined spots in the rings. Besides possible physiological constraints, these also impose certain limitations in the surgical procedure.

The physical constraints of the frame basically reflect the assumptions associated with the mathematical theory. For example, the requirement that the bone fragments should be perpendicular to the ring planes in TSF most likely simplifies the utilized mathematical model and the resulting computation. Hence, if certain assumptions in the mathematical theory could be relaxed, that would lead to a smaller number of constraints to be imposed on the physical frame. The practical consequence of this would be a higher level of flexibility when setting up the fixator frame surgically. In other words, it would be an advantage for the surgeon, if he/she is allowed to connect the struts to any ring hole he/she wishes, or does not have to worry about if bone fragments are perpendicular to the ring planes or not.

It would be desirable to develop an improved external fixator and software in the view of the limitations and drawbacks of the current systems. With that, a new mathematical theory has to be developed and implemented as well. A more flexible system as such may bring certain complications with itself. The possibility of a *singular configuration* where the frame loses its rigidity and becomes clinically not acceptable has to be taken into consideration.

1.2. Overview of Ring Fixator Systems

TSF is the first ring fixator system based on a (3-3) type Gough-Stewart Platform (or *hexapod*). It consists of 6 struts connecting two rings at 12 pre-defined fixed points (Gough and Whitehall, 1962; Stewart, 1965), (Figure 1.4). Since then, a number of improvements has been proposed on TSF system and, inspired from TSF, other hexapod systems have also been developed.

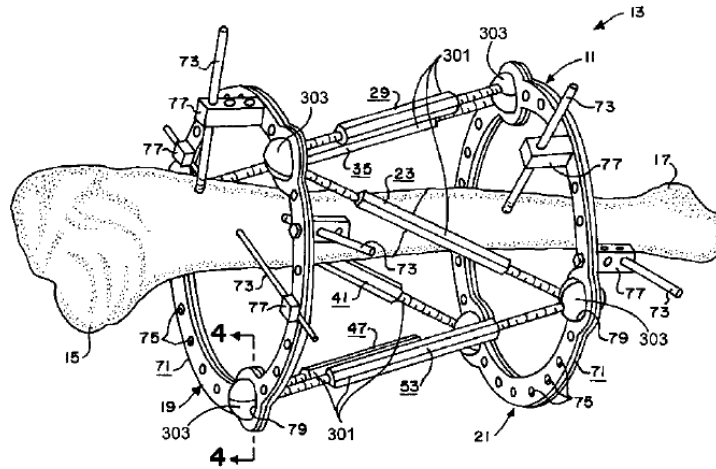


Figure 1.4. Taylor Spatial Frame (Taylor et al., 1999)

Koo, Han et al use the same system with Taylor, except modify the struts, such that it possible to read the length of the rod digitally (Koo et al., 2002), (Figure 1.5). For the motorized fixator system, this length information can be feedback to the computer to make the system ready for automatic adjustment of the distraction rate and frequency during treatment.

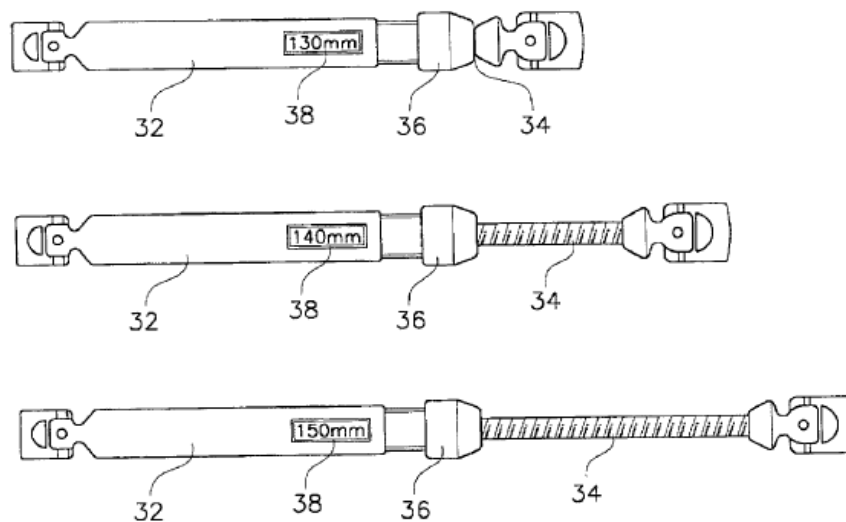


Figure 1.5. The rods used by Koo et al. (2002).

Austin et al. (2004) use an external fixator similar to the TSF. In their patent, they described a computer software which is developed to manipulate the system in a virtual environment.

Haskell (2014) has patented a computer software for easier use of the TSF. It is claimed that the developed graphical user interface generates a virtual copy of the fixator. The virtual fixator is superimposed on the digital X-Ray image of the patient. By applying translation, rotation and azimuthal rotation, its parts are aligned on the X-ray image. This aligned configuration is used in the generation of the timeline of the treatment.

Smart Correction is one of the computer-assisted external fixator systems currently available on the market (Ortho, 2015). It is based on the TSF and a method similar to the one developed by Haskell (2014). After the fixator is mounted to the patient's limb, the strut lengths are entered to the system. The number of the hole, closest to the X-ray source during X-ray imaging, is also fed to the system. This hole is used to pinpoint the AP direction, hence indicates the rotational position of the system with respect to the imaging plane.

Spider Frame, developed in Turkey, is another computer-assisted external fixator system on the market (Tasarimmed, 2015). The company has developed a software named *Spiderfix*, based on artificial neural networks, to control TSF frame.

Adam frame is also developed in Turkey in 2009 by the ISIN Company. The system, different than the TSF, uses standard four strut connection of Illizarov device and support these four strut with extra four stabilizer arms (Figure 1.6). Therefore the system has the advantage of the Illizarov device combined with octopod design (Paley, 2011). It should be noted that, commercially, this frame is no longer available.



Figure 1.6. Adam Frame

SUV is a relatively new external fixation system with a different design than the TSF (Takata et al., 2013). It is produced by Ortho-SUV company (Solomin et al., 2015). Only three of the struts are connected to each ring, and the other three struts are connected to the sides of another strut (Figure 1.7). The associated mathematical theory of this fixator system is not revealed. The design resembles the lambda fixator system that we will introduce in Chapter 3, although it does not seem to possess the connection flexibility that our proposed system possesses. The SUV external fixator system is considered one of the most modular systems available (Paley, 2011).



Figure 1.7. SUV external fixator (Solomin et al., 2015)

TrueLok-Hex, developed by the Italian company Orthofix (Orthofix, 2015), is one of the ring external fixators that has a TSF-like design. In their mathematical model, they relax the constraint of the TSF where the bone fragment has to be perpendicular to the reference ring. They also have developed a strut model which can be fixed to the rings in a simple manner and have a design to enhance rapid adjustment (Ross et al., 2013), (Figure 1.8 and Figure 1.9).



Figure 1.8. The locking of the struts to the rings in TrueLok-Hex.

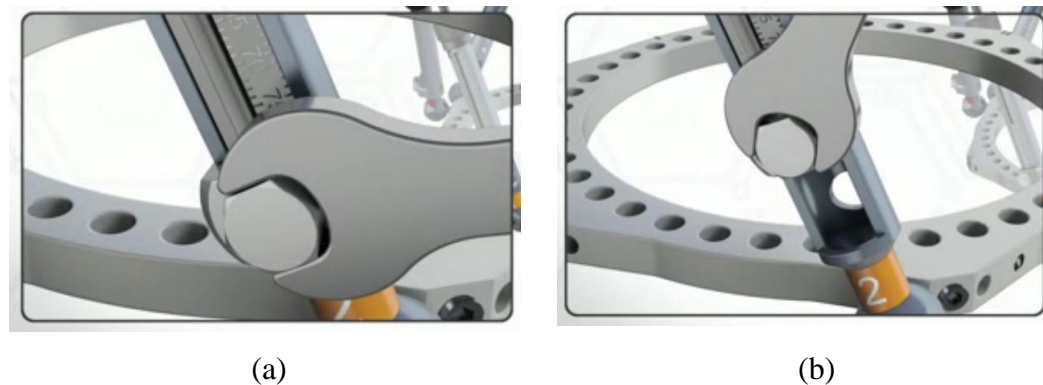


Figure 1.9. Rapid adjustment of the struts in TrueLok-Hex.

Tang et al. (2012) have developed a computer software to be used for surgery planning with the TSF. The developed software utilizes the CT scans of both limbs of patient. The image of the deformed bone is flipped around the vertical axis and cut into two pieces. Then, these pieces are fitted to the healthy bone image. Therefore, the bone fragment positions before and after treatment are obtained. All the parameters needed

for the reduction procedure, such as length, angulation, translation and rotation, are derived from these two positions.

One of the problems common to the ring fixator systems is the bone image being partially blocked by the metallic struts in the X-ray films. As a solution to this problem, Karidis and Stevens (2009) designed a strut with minimal X-Ray absorption. In a separate patent, to minimize the data loss, Karidis (2009) also proposed some structural changes in the fixator system such that the deformity area will be blocked less by the struts (Figure 1.10).

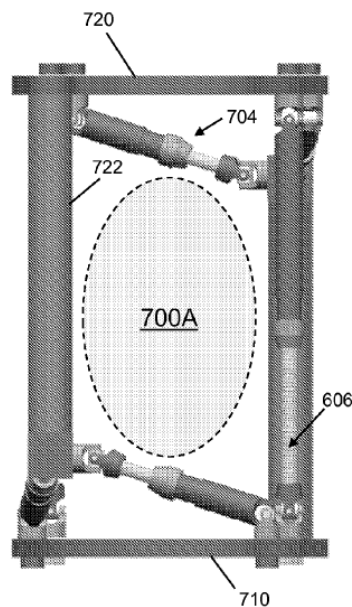


Figure 1.10. External fixator designed by Karidis (2009)

Current systems of external ring fixators have been used successfully for some time in the treatment of complex deformities. Yet, as we have outlined above, they can still be improved in order to simplify the orthopedist's work, by shortening the operation time and easing their installment, thereby increasing the patient's comfort. In this doctoral research, we have tried to accomplish a number of such improvement as summarized in the next section.

1.3. Contributions of the Thesis

- In the existing computer-assisted systems, the X-ray film has to be taken in such a way that the proximal ring appears as a line in the image, which may be clinically inconvenient. (We will refer to this situation as *normal view*.) We have extended the theory of the previously designed external fixator, based on Gough – Stewart Platform, to involve the case where this constraint is relaxed. (We will refer to this situation as *oblique view*.)
- We have designed a new configuration of external fixator, that we believe to be easier to handle clinically, and developed its mathematical model. (The details of this new external fixator are given in Chapter 3.)
- We have developed a software and an accompanying graphical user interface (GUI) where the X-ray images are processed and mathematical calculations are performed to produce the prescription for the treatment. We have tried to automatize the process of taking measurements from the X-Ray images as much as possible to minimize human intervention

1.4. Thesis Outline

The inverse kinematics of the proposed new fixator, referred to as *lambda fixator*, is derived from the model developed previously for the external fixator which is based on the (6-6) type Gough-Stewart Platform. Hence, the mathematical theory for the (6-6) type Gough-Stewart Platform External Fixator is presented first in Chapter 2 for completeness. The theory in case of the oblique view (i.e. the case where the proximal ring does not appear as line in the X-ray image) is derived by transforming the appropriate quantities of this model in 3-dimesional space and described in detail in Chapter 2 as well.

Chapter 3 contains the derivation of the inverse kinematics of the lambda fixator.

The external fixator may block the view of the bone fragments in X-ray images. In practice, this means loss of visual data which are meant to be used in the

mathematical calculations of treatment planning. An attempt has been made to recover the lost data as described in Chapter 4.

The distal ring, from which some necessary parameters are measured, generally appears as an ellipse in the X-Ray images. In an effort to automatize this measurement process, we have tried to fit an ellipse analytically to the distal ring image and calculate the related parameters from the ellipse equation. The details of this procedure is given in Chapter 5.

An integrated graphical user interface is developed that implements the mathematical model of the fixator in the background to be used by a clinician. The X-Ray images are fed into the user interface and the necessary parameters, some measured automatically and some manually, are obtained to make the calculations for treatment. The timeline of the strut lengths corresponding to a proper treatment are output to be followed by the clinician. The graphical user interface is described in Chapter 6.

Finally, the conclusion and summary of this doctoral work are presented in Chapter 7.

2. GOUGH – STEWART PLATFORM AS EXTERNAL FIXATOR

2.1. Inverse Kinematic Studies of the Gough – Stewart Platform

The Gough-Stewart Platform, used as an external fixator, has been introduced before and the details of this study has been reported elsewhere (Akçalı et al., 2009; Akçalı et al., 2009; Aydin, 2009; Akcali et al., 2010). Here, we will present the details of the related inverse kinematic analysis of the Gough-Stewart Platform for the sake of completeness.

2.1.1. Derivation of 3D Geometric Parameters from AP and L Images

In this part of the theory, the fundamental relationship between the position of a real object in xyz coordinate system and its images is given. It is assumed that a rod is located in the xyz –coordinate system and represented with w –axis (Figure 2.1). Two perpendicular projections of the rod are obtained by looking first along the x –direction (Figure 2.2 (a)) and then along the opposite y –direction (Figure 2.2 (b)). These images are referred to as *Lateral (L)* and *Anterior – Posterior (AP)* respectively. The rod length is denoted with c and its components are referred to as c_x, c_y, c_z ; the projected lengths of the rod for L and AP images are referred to as c_L and c_{AP} , the angles between the rod and z –axis for L and AP are referred to as Ψ_L and Ψ_{AP} . The relationship that exists between the rod and its images is calculated based on this configuration. Then, a transformation matrix between the xyz –coordinate system and a moving uvw –coordinate system is calculated from this relationship. The details of the calculations are given in this section.

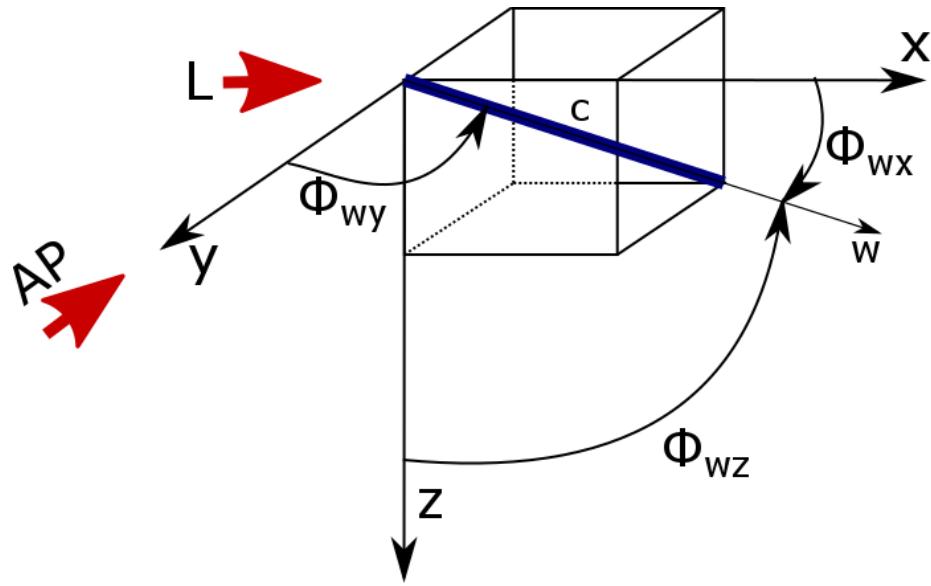


Figure 2.1. View – position relation of the rod

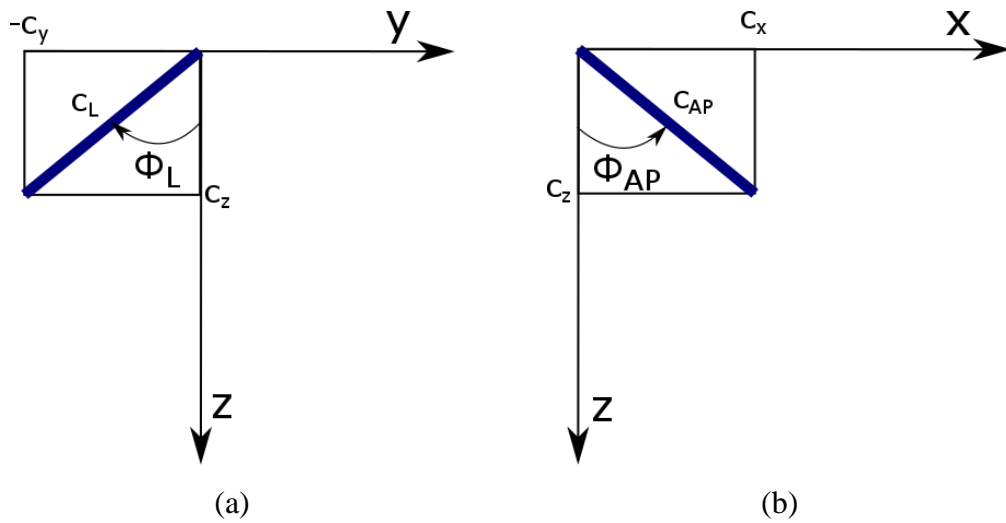


Figure 2.2. (a) Lateral and (b) Anterior – Posterior views of the rod

The following equations can be written from *AP* and *L* images and used to calculate the rod length *c*:

$$c_x = c_z \tan \Phi_{AP} \quad (2.1)$$

$$c_y = -c_z \tan \Phi_L \quad (2.2)$$

$$c^2 = c_x^2 + c_y^2 + c_z^2 \quad (2.3)$$

$$c_{AP}^2 = c_x^2 + c_z^2 \quad (2.4)$$

$$c_L^2 = c_y^2 + c_z^2 \quad (2.5)$$

By substituting Eq. (2.1) and Eq. (2.2) in Eqs. (2.3), (2.4) and (2.5)

$$c_z = \frac{c}{\sqrt{1 + \tan^2\Phi_{AP} + \tan^2\Phi_L}} \quad (2.6)$$

$$c_z = c_{AP}\cos\Phi_{AP} = c_L\cos\Phi_L \quad (2.7)$$

$$c_x = c_L\cos\Phi_L\tan\Phi_{AP} \quad (2.8)$$

$$c_y = -c_L\cos\Phi_L\tan\Phi_L \quad (2.9)$$

$$c = c_{AP}\cos\Phi_{AP}\sqrt{1 + \tan^2\Phi_{AP} + \tan^2\Phi_L} \quad (2.10)$$

If the angles between the rod and x, y, z axes are represented with $\Phi_{wx}, \Phi_{wy}, \Phi_{wz}$ respectively, it can be deduced from Figure 2.1 that

$$\cos\Phi_{wx} = \frac{c_x}{c}; \quad \cos\Phi_{wy} = \frac{c_y}{c}; \quad \cos\Phi_{wz} = \frac{c_z}{c} \quad (2.11)$$

If Eqs. (2.6) - (2.10) are substituted in Eq. (2.11), we obtain:

$$\cos\Phi_{wx} = \frac{\tan\Phi_{AP}}{\sqrt{1 + \tan^2\Phi_{AP} + \tan^2\Phi_L}} \quad (2.12)$$

$$\cos\Phi_{wy} = \frac{-\tan\Phi_L}{\sqrt{1 + \tan^2\Phi_{AP} + \tan^2\Phi_L}} \quad (2.13)$$

$$\cos\Phi_{wz} = \frac{1}{\sqrt{1 + \tan^2\Phi_{AP} + \tan^2\Phi_L}} \quad (2.14)$$

Using Eqs. (2.12) - (2.14), the vector e_w representing the rod can be written in component form as:

$$\vec{e}_w = \vec{i}\cos\Phi_{wx} + \vec{j}\cos\Phi_{wy} + \vec{k}\cos\Phi_{wz} \quad (2.15)$$

Let us assume that a moving uvw coordinate system is coincident with the xyz –coordinate system. If the uvw – coordinate system is rotated about x axis with an angle of θ_x , about y with θ_y and finally about z with θ_z , the resulting rotation matrix from uvw to xyz coordinate systems is:

$$[A_{xyz}^{uvw}] = rot[\theta_x, \theta_y, \theta_z] = [e_u, e_v, e_w] = \begin{bmatrix} e_{ux} & e_{vx} & e_{wx} \\ e_{uy} & e_{vy} & e_{wy} \\ e_{uz} & e_{vz} & e_{wz} \end{bmatrix} \quad (2.16)$$

which can be written as

$$[A_{xyz}^{uvw}] = \begin{bmatrix} \cos\theta_z\cos\theta_y & \cos\theta_z\sin\theta_y\sin\theta_x - \sin\theta_z\cos\theta_x & \cos\theta_z\sin\theta_y\cos\theta_x + \sin\theta_z\sin\theta_x \\ \sin\theta_z\cos\theta_y & \sin\theta_z\sin\theta_y\sin\theta_x + \cos\theta_z\cos\theta_x & \sin\theta_z\sin\theta_y\cos\theta_x - \cos\theta_z\sin\theta_x \\ -\sin\theta_y & \cos\theta_y\sin\theta_x & \cos\theta_y\cos\theta_x \end{bmatrix} \quad (2.17)$$

The rotation angle around z axis (θ_z) is one of the axial data which is directly entered to the calculations. Here, the x , y , z component of vector \vec{e}_w and θ_z are known, therefore θ_y and θ_x can be computed as:

$$\tan\theta_y = \frac{e_{wx}\cos\theta_z + e_{wy}\sin\theta_z}{e_{wz}} \quad (2.18)$$

$$\cos\theta_x = \frac{e_{wz}}{\cos\theta_y} \quad (2.19)$$

Therefore all elements of $[A_{xyz}^{uvw}]$ matrix can be computed (Eq. (2.17)).

2.1.2. Derivation of Transformations and Strut Length Calculation

The biomechanical system under consideration is a (6-6) type Gough-Stewart Platform mechanism along with two bone fragments attached to two rings which are named as *proximal* (top ring) and *distal* (bottom ring) rings (Figure 2.3). With this theory, two orthogonal X-ray images taken from Lateral (*L*) and Anterior – Posterior (*AP*) directions and some known parameters are used to find the configuration of the biomechanical system for initially unaligned and finally aligned positions of the bone fragments. Four coordinate systems are defined in this theory. The global *xyz* –coordinate system is located at the center of the proximal ring; the moving *uvw* –coordinate system is located at the center of the distal ring; the other two coordinate systems are located using the proximal (*x'y'z'*) and distal (*u'v'w'*) bone fragment axes (Figure 2.3). The parameters obtained from X-rays are $\beta'_{AP}, \beta_{AP}, q_x, e_x, e_z, r_x, r_z, \Psi_{AP}$ (Figure 2.4, (a)) for *AP* view and $\beta'_L, \beta_L, q_y, e_y, e_z, r_y, r_z, \Psi_L$ (Figure 2.4, (b)) for *L* view. The known parameters (entered by the clinician to the system) are the rotation angle between proximal and distal rings (δ_0) and between bone fragments (δ_{Ax}) (Figure 2.5); the angular positions of proximal ($\alpha_i, i = 1 - 6$) and distal ($\epsilon_i, i = 1 - 6$) joints (Figure 2.6) and radii of the proximal (*R*) and distal (*R*₁) rings. The parameters measured from *z* axis of the X-rays (e_z, r_z) are common for both images and can be used to cross-check some measured data.

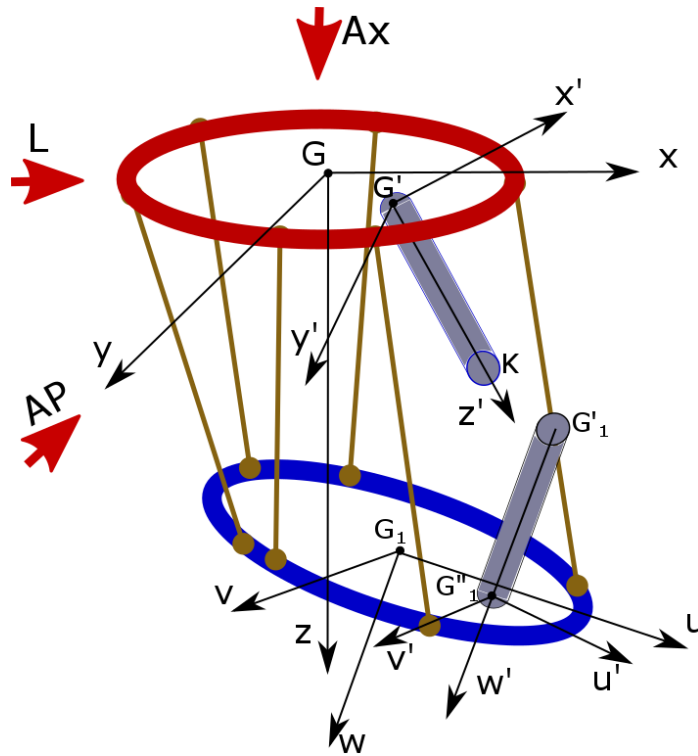


Figure 2.3. The biomechanical system and location of the coordinate systems.

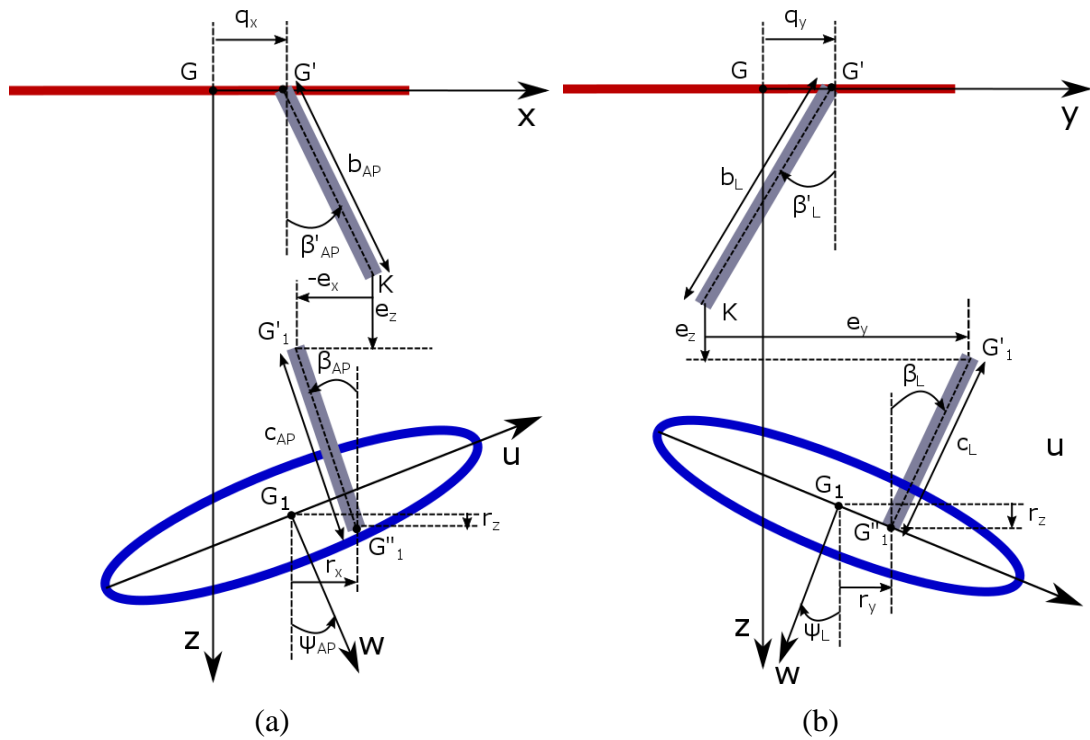


Figure 2.4. View – position relations of the biomechanical system for (a) AP and (b) L views.

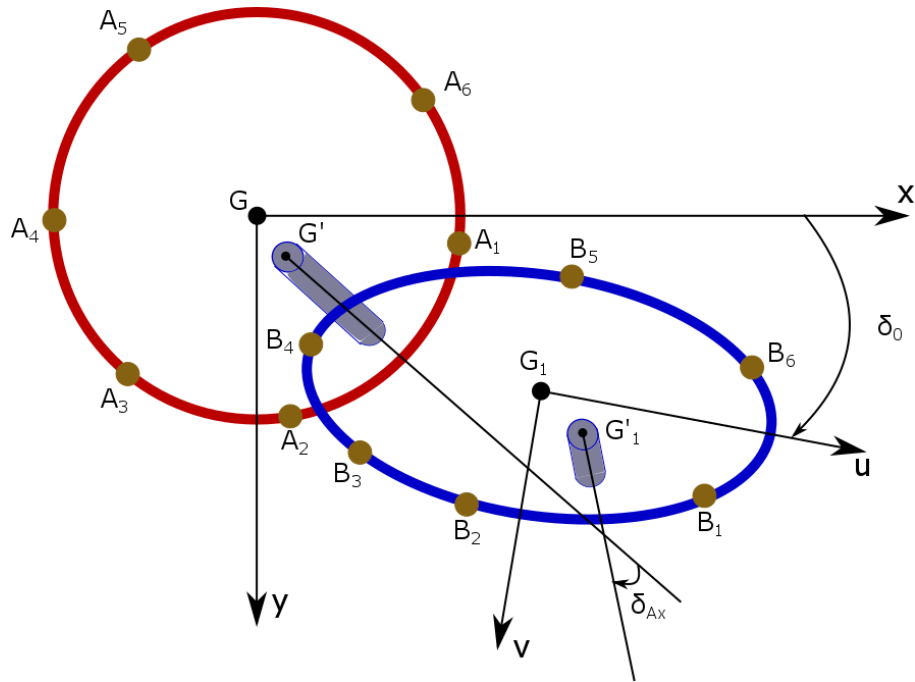


Figure 2.5. Relative angular orientation of the rings and the bone fragments

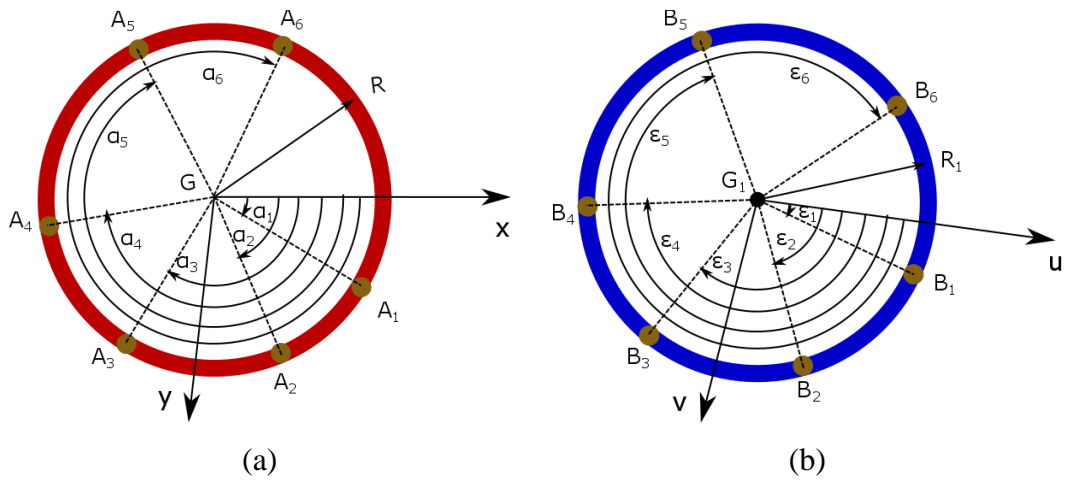


Figure 2.6. Angular positions of the joints at (a) the proximal and (b) the distal rings.

The transformation matrices between coordinate systems are obtained by applying the theory given in Section 2.1.1. The Φ_{AP} , Φ_L , θ_z values of Section 2.1.1 are replaced with the appropriate data as outlined below:

- Angles Ψ_{AP} , Ψ_L , δ_0 are used to define the transformation matrix from uvw to xyz coordinate system:

$$[A_{xyz}^{uvw}]_0 = \begin{bmatrix} e_{ux} & e_{vx} & e_{wx} \\ e_{uy} & e_{vy} & e_{wy} \\ e_{uz} & e_{vz} & e_{wz} \end{bmatrix}$$

- Angles $\beta_{AP}, \beta_L, \delta_{Ax}$ are used to define the transformation matrix from $u'v'w'$ to xyz coordinate system:

$$[A_{xyz}^{u'v'w'}]_0 = \begin{bmatrix} e_{u'x} & e_{v'x} & e_{w'x} \\ e_{u'y} & e_{v'y} & e_{w'y} \\ e_{u'z} & e_{v'z} & e_{w'z} \end{bmatrix}$$

- Angles $\beta'_{AP}, \beta'_L, 0$ are used to define the transformation matrix from $x'y'z'$ to xyz coordinate system:

$$[A_{xyz}^{x'y'z'}] = \begin{bmatrix} e_{x'x} & e_{y'x} & e_{z'x} \\ e_{x'y} & e_{y'y} & e_{z'y} \\ e_{x'z} & e_{y'z} & e_{z'z} \end{bmatrix}$$

The transformation matrix between $u'v'w'$ and uvw coordinate systems is:

$$[A_{uvw}^{u'v'w'}]_0 = [A_{xyz}^{uvw}]_0^T [A_{xyz}^{u'v'w'}]_0 \quad (2.20)$$

Here, the superscript “T” indicates the matrix transpose while indices “0” and “n” denote the initial and final positions of the system, respectively.

The coordinates of the joints on proximal and distal rings are given as:

$$x_{A_i} = R \cos \alpha_i; \quad y_{A_i} = R \sin \alpha_i \quad i = 1 - 6 \quad (2.21)$$

$$u_{B_i} = R_1 \cos \varepsilon_i; \quad v_{B_i} = R_1 \sin \varepsilon_i \quad i = 1 - 6 \quad (2.22)$$

The following vector equation can be deduced from Figure 2.3.

$$\overrightarrow{GG_1} = \overrightarrow{GG'} + \overrightarrow{G'K} + \overrightarrow{KG'_1} + \overrightarrow{G'_1G''_1} - \overrightarrow{G_1G''_1} \quad (2.23)$$

where the vectors involved can be expressed in xyz –coordinate system as:

$$\overrightarrow{GG'} = q_x \vec{i} + q_y \vec{j}; \quad \overrightarrow{G'K} = b \vec{e}_{z'} \quad (2.24)$$

$$\overline{KG'_1} = e_x \vec{i} + e_y \vec{j} + e_z \vec{k}; \quad \overline{G'_1 G''_1} = c \overline{e_{w'i}} \quad (2.25)$$

$$\overline{G_1 G''_1} = r_x \vec{i} + r_y \vec{j} + r_z \vec{k} \quad (2.26)$$

$$\overline{G'_1 K} = b (e_{z'ix} \vec{i} + e_{z'iy} \vec{j} + e_{z'iz} \vec{k}) \quad (2.27)$$

$$\overline{G'_1 G''_1} = c (e_{w'ix} \vec{i} + e_{w'iy} \vec{j} + e_{w'iz} \vec{k}) \quad (2.28)$$

Then the position of the joint with respect to the proximal ring center is calculated as:

$$\overline{G_1 B_i} = (u_{B_i} e_{ux} + v_{B_i} e_{vx}) \vec{i} + (u_{B_i} e_{uy} + v_{B_i} e_{vy}) \vec{j} + (u_{B_i} e_{uz} + v_{B_i} e_{vz}) \vec{k} \quad i = 1 - 6 \quad (2.29)$$

$$\overline{G A_i} = x_{A_i} \vec{i} + y_{A_i} \vec{j} \quad i = 1 - 6 \quad (2.30)$$

$$\overline{G B_i} = \overline{G G_1} + \overline{G_1 B_i} \quad i = 1 - 6 \quad (2.31)$$

Finally, the rod lengths for initial configuration of the biomechanical system is calculated from position vectors of the joints as:

$$L_i = |G A_i - G B_i|_0 \quad i = 1 - 6 \quad (2.32)$$

The position of the bone fragments relative to the rings does not change between initial and final positions of the system. Hence, the transformation matrices between $u'v'w'$ and uvw , and between $x'y'z'$ and xyz coordinate systems are the same for both states:

$$[A_{uvw}^{u'v'w'}]_n = [A_{uvw}^{u'v'w'}]_0 \quad (2.33)$$

$$[A_{xyz}^{x'y'z'}]_n = [A_{xyz}^{x'y'z'}]_0 \quad (2.34)$$

Similarly, the point where the bone fragments connected to the ring plane does not change in the ring coordinate system, and the following equations can be written:

$$(\overline{G_1 G''})_0 = r_u \overline{e_{u_0}} + r_v \overline{e_{v_0}} = r_x \vec{i} + r_y \vec{j} + r_z \vec{k} \quad (2.35)$$

$$r_u = r_x e_{ux_0} + r_y e_{uy_0} + r_z e_{uz_0} \quad (2.36)$$

$$r_v = r_x e_{vx_0} + r_y e_{vy_0} + r_z e_{vz_0} \quad (2.37)$$

The distal ring has been moved so the transformation matrix between uvw and xyz coordinate systems is calculated again:

$$[A_{xyz}^{uvw}]_n = [A_{xyz}^{uvw}]_n [A_{uvw}^{uvw}]_n^T \quad (2.38)$$

For the aligned state the following equalities can be written

$$[A_{xyz}^{x'y'z'}]_n = [A_{xyz}^{uvw}]_n \quad (2.39)$$

$$[A_{xyz}^{uvw}]_n = [A_{xyz}^{x'y'z'}]_0 [A_{uvw}^{uvw}]_0 \quad (2.40)$$

Finally the position vectors of the distal joints in xyz –coordinate systems is calculated as:

$$(\overline{GG_1})_n = \overline{GG'} + \overline{G'G''_1} - (\overline{G_1 G''_1})_n \quad (2.41)$$

$$\overline{G'G''_1} = (b + c) (e_{z'x'} \vec{i} + e_{z'y'} \vec{j} + e_{z'z'} \vec{k}) \quad (2.42)$$

$$(\overrightarrow{G_1 G''_1})_n = r_u \overrightarrow{e_{un}} + r_v \overrightarrow{e_{vn}} \quad (2.43)$$

$$(\overrightarrow{GB_i})_n = (\overrightarrow{GG_1})_n + (\overrightarrow{G_1 B_i})_n \quad i = 1 - 6 \quad (2.44)$$

$$(\overrightarrow{G_1 B_i})_n = u_{B_i} \overrightarrow{e_{un}} + v_{B_i} \overrightarrow{e_{vn}} \quad (2.45)$$

Since the proximal ring is stationary, the position vectors of the proximal ring joints do not change between states. And finally, the rod lengths for the aligned state of the system are calculated as:

$$L_{i_n} = |GA_i - GB_i|_n \quad (2.46)$$

2.2. Extending the Theory to Oblique View Case

In the currently used external fixator models, the X-Ray image of the bone-fixator system must be taken in such a way that the proximal ring is seen as a straight line. This constraint that simplifies the mathematical theory is not easy to impose in practice. Even for a well-trained X-ray technician, it may be difficult to align the X-ray source with proximal ring plane. Clearly, any deviation from this constraint reflect itself as an error in the mathematical model and affects the outcome. As a solution to this potential problem, the mathematical model presented in Section 2.1 is extended to cover the oblique view case where the proximal ring appears as an ellipse rather than a line in the X-ray image.

It should be noted that oblique view model is more general and the theory presented in Section 2.1 can be taken as a special case of it. With this model, one potential error source is eliminated and the clinical procedure is simplified both for the clinician and the patient.

Previously, we have indicated quantities originating from anterior-posterior and lateral X-ray images with the indices AP and L , respectively. Here, we use a prime notation (namely AP' and L') to refer to the same quantities in the oblique view. In our

approach, we transform quantities in the oblique view mathematically to their normal view counterparts and perform the calculation using the mathematical model derived for the normal view in Section 2.1 (Figure 2.7).

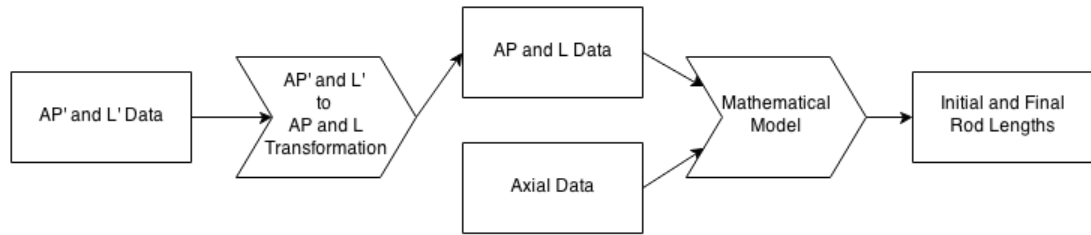


Figure 2.7. Flowchart of the mathematical model

Two approaches are presented for the conversion of the oblique view data to normal view data. The first one transforms the lengths in the oblique planes ($b_{L'}, c_{L'}, b_{AP'}, c_{AP'}$) and the angles ($\beta_{L'}, \beta'_{L'}, \beta'_{AP'}, \beta_{AP'}, \psi_{AP'}, \psi_{L'}$) to the normal plane parameters of the mathematical model. The second one translates the reference points ($G, G', K, G'_1, G''_1, G_1$) to the normal plane and the input parameters are calculated from these reference points. It is not possible to obtain all parameters from one approach alone. Hence, both methods will be used to generate the needed parameters of the currently used mathematical model.

2.2.1. Direct Theoretical Data Transformation

In this section, the relationship between newly defined L' and AP' views and currently used L and AP views will be derived. The input data in the L' and AP' images will be measured in the same manner as in the L and AP images and then these values will be transformed to their actual values in L and AP views.

2.2.1.1. Relationship between L and L' – Views

In this theory, we assume that there is a rod of length c with an xyz -coordinate system defined at its one end. As a vector, the components of this rod along x, y, z axes

are $c_x, -c_y, c_z$ which are unknown at this point. If xyz coordinate system is rotated around y -axis in the counterclockwise direction by an angle of α_y , the XYZ -coordinate system is obtained (Figure 2.8). The rod components of the rod in XYZ -coordinate system are C_X, C_Y, C_Z . L' - view corresponds to observing the XYZ -coordinate system along the x -axis. In this part, a new relationship between yz and YZ planes, which are defined at L and L' -views consequently (Figure 2.9), will be derived.

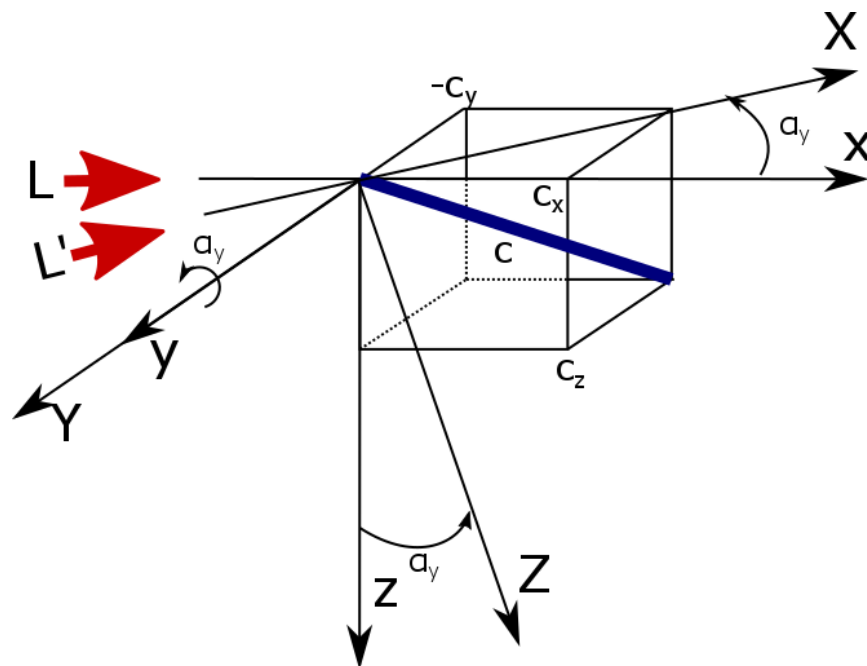


Figure 2.8. Lateral view and L' - view

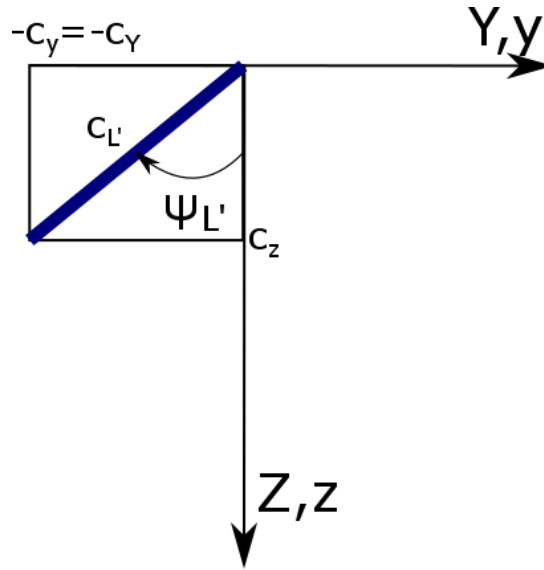


Figure 2.9. L' - view

The components of the rod in both coordinate systems are related by:

$$\begin{aligned} \begin{bmatrix} c_x \\ c_y \\ c_z \end{bmatrix} &= \begin{bmatrix} \cos \alpha_y & 0 & \sin \alpha_y \\ 0 & 1 & 0 \\ -\sin \alpha_y & 0 & \cos \alpha_y \end{bmatrix} \begin{bmatrix} C_X \\ C_Y \\ C_Z \end{bmatrix} \\ &= \begin{bmatrix} \cos \alpha_y C_X + \sin \alpha_y C_Z \\ C_Y \\ -\sin \alpha_y C_X + \cos \alpha_y C_Z \end{bmatrix} \end{aligned} \quad (2.47)$$

or, writing the individual components:

$$c_x = \cos \alpha_y C_X + \sin \alpha_y C_Z \quad (2.48)$$

$$c_y = C_Y \quad (2.49)$$

$$c_z = -\sin \alpha_y C_X + \cos \alpha_y C_Z \quad (2.50)$$

where α_y is obtained from major and minor axes of the proximal ring which is seen as an ellipse in the L image $\left(\alpha_y = \sin^{-1} \left(\frac{r_{minor}}{r_{major}} \right) \right)$. Using the above equations, the

following relations can be derived between the components and the angle $\psi_{L'}$ (Figure 2.9):

$$\tan \psi_{L'} = -\frac{C_Y}{C_Z} = -\frac{c_y}{\sin \alpha_y c_x + \cos \alpha_y c_z} \quad (2.51)$$

2.2.1.2. Relationship between AP and AP' – Views

Similar to the L' -view, if the same rod and coordinate system is rotated around x -axis in the counterclockwise direction by an angle of α_x , the $X'Y'Z'$ -coordinate system is obtained (Figure 2.10). The rod components at this coordinate system are denoted as $C_{X'}, C_{Y'}, C_{Z'}$. AP' - view corresponds to observing the $X'Y'Z'$ -coordinate system along the y -axis (Figure 2.11).

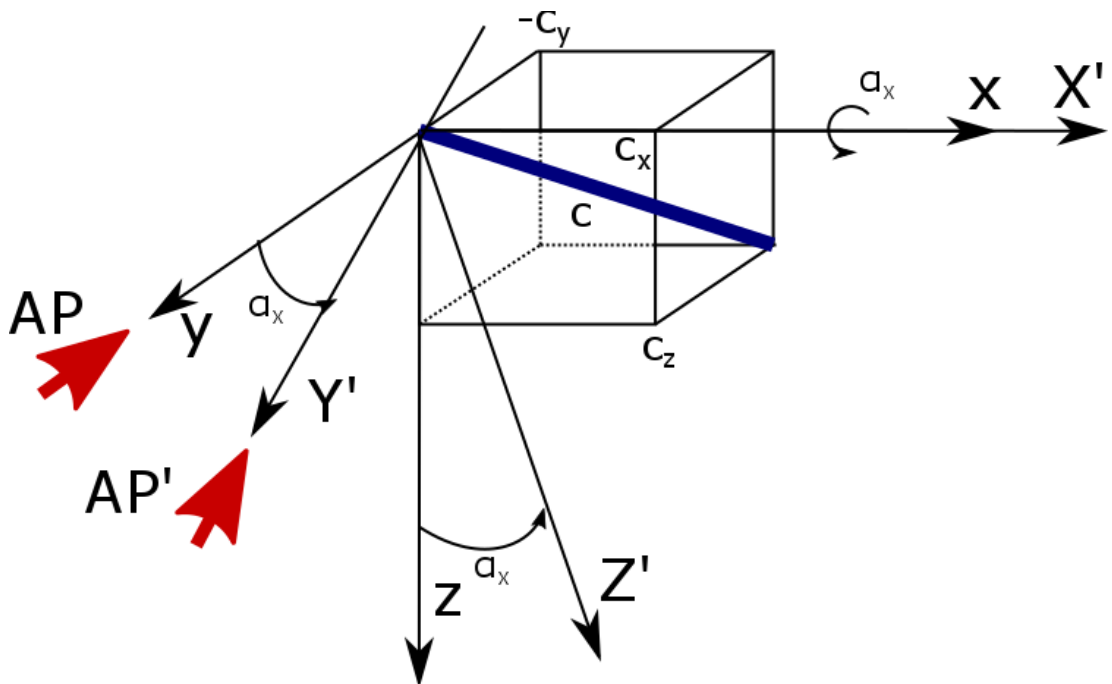


Figure 2.10. AP and AP' views

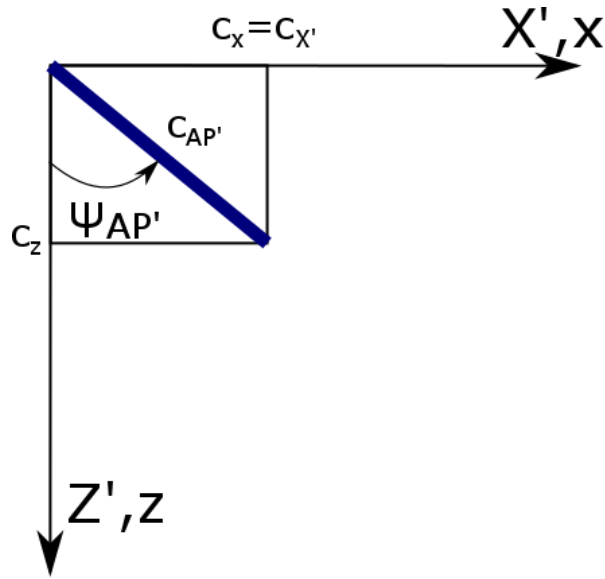


Figure 2.11. AP' view

The components of the rod in both coordinate systems are related by:

$$\begin{aligned} \begin{bmatrix} c_x \\ c_y \\ c_z \end{bmatrix} &= \begin{bmatrix} 1 & 0 & 0 \\ 0 & \cos \alpha_x & -\sin \alpha_x \\ 0 & \sin \alpha_x & \cos \alpha_x \end{bmatrix} \begin{bmatrix} C_{X'} \\ C_{Y'} \\ C_{Z'} \end{bmatrix} \\ &= \begin{bmatrix} C_{X'} \\ \cos \alpha_x C_{Y'} - \sin \alpha_x C_{Z'} \\ \sin \alpha_x C_{Y'} + \cos \alpha_x C_{Z'} \end{bmatrix} \end{aligned} \quad (2.52)$$

or, writing the individual components:

$$c_x = C_{X'} \quad (2.53)$$

$$c_y = \cos \alpha_x C_{Y'} - \sin \alpha_x C_{Z'} \quad (2.54)$$

$$c_z = \sin \alpha_x C_{Y'} + \cos \alpha_x C_{Z'} \quad (2.55)$$

where α_x is obtained from major and minor axes of the proximal ring which is seen as an ellipse in the AP image ($\alpha_x = \sin^{-1} \left(\frac{r_{minor}}{r_{major}} \right)$). Hence, such a relationship can be derived for any angle $\psi_{AP'}$ (Figure 2.11):

$$\tan \psi_{AP'} = \frac{C_{X'}}{C_{Z'}} = \frac{c_x}{-\sin \alpha_y c_y + \cos \alpha_x c_z} \quad (2.56)$$

2.2.1.3. Combining the Data Obtained from AP' and L'

When we combine the data obtained from both images, using the common components:

$$-\frac{c_y}{c_z} = \left(\sin \alpha_y \frac{c_x}{c_z} + \cos \alpha_y \right) \tan \psi_{L'} \quad (2.57)$$

$$\tan \psi_L = (\sin \alpha_y \tan \psi_{AP} + \cos \alpha_y) \tan \psi_{L'} \quad (2.58)$$

$$\frac{c_x}{c_z} = \left(-\sin \alpha_x \frac{c_y}{c_z} + \cos \alpha_x \right) \tan \psi_{AP'} \quad (2.59)$$

$$\tan \psi_{AP} = (\sin \alpha_x \tan \psi_L + \cos \alpha_x) \tan \psi_{AP'} \quad (2.60)$$

If Eq.(2.58) is substituted in Eq. (2.60), we obtain:

$$\begin{aligned} \tan \psi_{AP} = & (\sin \alpha_x (\sin \alpha_y \tan \psi_{AP} + \cos \alpha_y) \tan \psi_{L'} \\ & + \cos \alpha_x) \tan \psi_{AP'} \end{aligned} \quad (2.61)$$

$$\begin{aligned} \tan \psi_{AP} = & \sin \alpha_x \sin \alpha_y \tan \psi_{AP} \tan \psi_{L'} \tan \psi_{AP'} \\ & + \sin \alpha_x \cos \alpha_y \tan \psi_{L'} \tan \psi_{AP'} \\ & + \cos \alpha_x \tan \psi_{AP'} \end{aligned} \quad (2.62)$$

$$\tan \psi_{AP} = \frac{\sin \alpha_x \cos \alpha_y \tan \psi_{L'} \tan \psi_{AP'} + \cos \alpha_x \tan \psi_{AP'}}{(1 - \sin \alpha_x \sin \alpha_y \tan \psi_{L'} \tan \psi_{AP'})} \quad (2.63)$$

With Eq. (2.58) and Eq. (2.63), angles in AP' and L' views can be transformed to the corresponding angles in AP and L views using α_x and α_y values.

Using the lengths in L' and AP' views, namely $(c_{L'}, c_{AP'})$, lengths in L and AP views, namely (c_L, c_{AP}) , can be obtained. The following formulas can be applied in any length parameter including the strut lengths:

$$\cos \psi_{L'} = \frac{c_Z}{c_{L'}} \rightarrow c_{L'} = \frac{c_Z}{\cos \psi_{L'}} \quad (2.64)$$

$$c_{L'} = \frac{\sin \alpha_y c_x + \cos \alpha_y c_z}{\cos \psi_{L'}} = \frac{\sin \alpha_y c_z \tan \psi_{AP} + \cos \alpha_y c_z}{\cos \psi_{L'}} \quad (2.65)$$

$$c_{L'} = c_z \frac{\sin \alpha_y \tan \psi_{AP} + \cos \alpha_y}{\cos \psi_{L'}} \quad (2.66)$$

$$\cos \psi_{AP'} = \frac{c_{Z'}}{c_{AP'}} \rightarrow c_{AP'} = \frac{c_{Z'}}{\cos \psi_{AP'}} \quad (2.67)$$

$$c_{AP'} = \frac{-\sin \alpha_x c_y + \cos \alpha_x c_z}{\cos \psi_{AP'}} = c_z \frac{\sin \alpha_x \tan \psi_L + \cos \alpha_x}{\cos \psi_{AP'}} \quad (2.68)$$

$$c_z = c_L \cos \psi_L = c_{AP} \cos \psi_{AP} \quad (2.69)$$

$$c_z = \frac{c_{L'} \cos \psi_{L'}}{\sin \alpha_y \tan \psi_{AP} + \cos \alpha_y} = \frac{c_{AP'} \cos \psi_{AP'}}{\sin \alpha_x \tan \psi_L + \cos \alpha_x} \quad (2.70)$$

$$c_L = \frac{1}{\cos \psi_L} \frac{c_{L'} \cos \psi_{L'}}{(\sin \alpha_y \tan \psi_{AP} + \cos \alpha_y)} \quad (2.71)$$

$$c_{AP} = \frac{1}{\cos \psi_{AP}} \frac{c_{AP'} \cos \psi_{AP'}}{(\sin \alpha_x \tan \psi_L + \cos \alpha_x)} \quad (2.72)$$

Eq. (2.71) and Eq. (2.72) now can be used to transform rod lengths from L' and AP' views to L and AP views.

2.2.1.4. Obtaining q_x and q_y

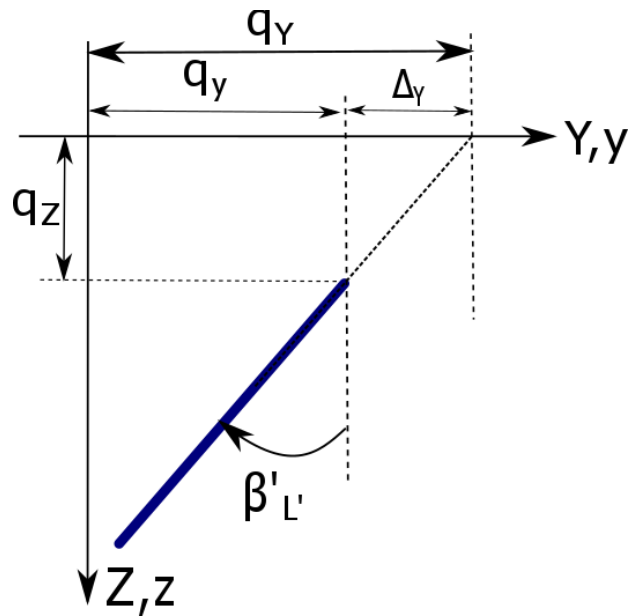


Figure 2.12. L' view and proximal ring plane

q_x and q_y are two perpendicular distance values which describe the position of the point where the bone intersects the ring plane with respect to the ring center. If the ring plane appears as a straight line on the X-ray images (AP and L images), q_x and q_y can be easily found by intersecting the bone axis with the ring line. In the case of oblique view (where the ring appears as an ellipse), the intercept of the major axis of the ellipse and the bone axis will not give the actual q_x and q_y values. Instead, it will give the projection of them, namely q_x, q_y (Figure 2.12 and Figure 2.13). To obtain the actual parameters from the projected ones, the following definitions are made:

$$q_Y = q_y + q_z \tan \beta'_{L'} \quad (2.73)$$

$$q_y = q_Y - q_z \tan \beta'_{L'} \quad (2.74)$$

$$\tan \beta'_{L'} = \frac{\Delta_Y}{q_Z} \rightarrow \Delta_Y = q_Z \tan \beta'_{L'} \quad (2.75)$$

$$\begin{bmatrix} q_X \\ q_Y \\ q_Z \end{bmatrix} = [A_{xyz}^{XYZ}]^{-1} \begin{bmatrix} q_x \\ q_y \\ 0 \end{bmatrix} = [A_{XYZ}^{xyz}] \begin{bmatrix} q_x \\ q_y \\ 0 \end{bmatrix} = [A_{xyz}^{XYZ}]^T \begin{bmatrix} q_x \\ q_y \\ 0 \end{bmatrix} \quad (2.76)$$

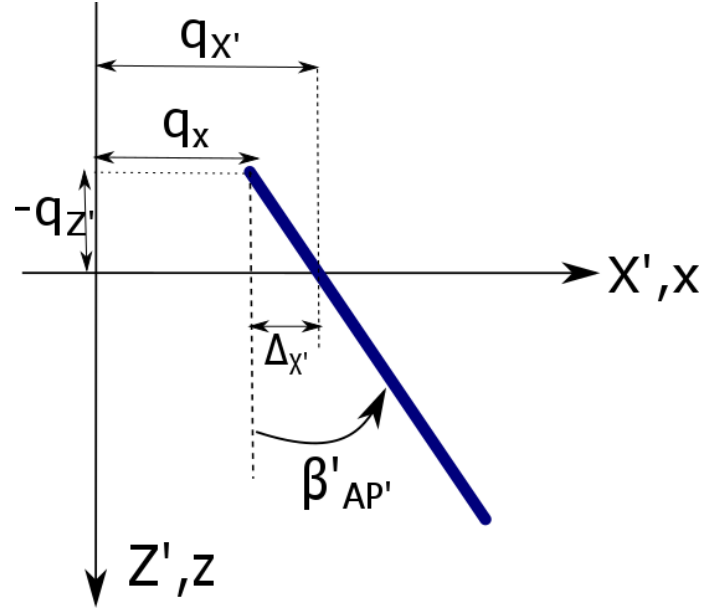
$$\begin{bmatrix} q_X \\ q_Y \\ q_Z \end{bmatrix} = \begin{bmatrix} \cos \alpha_y & 0 & -\sin \alpha_y \\ 0 & 1 & 0 \\ \sin \alpha_y & 0 & \cos \alpha_y \end{bmatrix} \begin{bmatrix} q_x \\ q_y \\ 0 \end{bmatrix} = \begin{bmatrix} \cos \alpha_y q_x \\ q_y \\ \sin \alpha_y q_x \end{bmatrix} \quad (2.77)$$

$$q_Z = \sin \alpha_y q_x \quad (2.78)$$

If we substitute Eq. (2.78) into Eq. (2.74):

$$q_y = q_Y - \sin \alpha_y q_x \tan \beta'_{L'} \quad (2.79)$$

The same procedure need to be applied to the AP' image to obtain q_x and then substitute in Eq.(2.79).


 Figure 2.13. AP' view and proximal ring plane

$$q_{X'} = q_x \quad (2.80)$$

$$\begin{aligned} \begin{bmatrix} q_{X'} \\ q_{Y'} \\ q_{Z'} \end{bmatrix} &= [A_{X'Y'Z'}^{xyz}] \begin{bmatrix} q_x \\ q_y \\ 0 \end{bmatrix} = [A_{xyz}^{X'Y'Z'}]^T \begin{bmatrix} q_x \\ q_y \\ 0 \end{bmatrix} \\ &= \begin{bmatrix} 1 & 0 & 0 \\ 0 & \cos \alpha_x & \sin \alpha_x \\ 0 & -\sin \alpha_x & \cos \alpha_x \end{bmatrix} \begin{bmatrix} q_x \\ q_y \\ 0 \end{bmatrix} = \begin{bmatrix} q_x \\ \cos \alpha_x q_y \\ -\sin \alpha_x q_y \end{bmatrix} \end{aligned} \quad (2.81)$$

$$q_{Z'} = -\sin \alpha_x q_y \quad (2.82)$$

$$\tan \beta'_{AP'} = \frac{\Delta_{X'}}{q_{Z'}} \rightarrow \Delta_{X'} = q_{Z'} \tan \beta'_{AP'} = -\sin \alpha_x q_y \tan \beta'_{AP'} \quad (2.83)$$

$$q_x = q_{X'} - \Delta_{X'} = q_{X'} + \sin \alpha_x q_y \tan \beta'_{AP'} \quad (2.84)$$

$$q_x = q_{X'} + \sin \alpha_x \tan \beta'_{AP'} (q_y - q_x \sin \alpha_y \tan \beta'_{L'}) \quad (2.85)$$

$$q_x = \frac{q_{X'} + \sin \alpha_x \tan \beta'_{AP'} q_Y}{1 + \sin \alpha_x \sin \alpha_y \tan \beta'_{AP'} \tan \beta'_{L'}} \quad (2.86)$$

and finally when we substitute Eq. (2.86) into Eq. (2.79):

$$q_y = \frac{q_Y + q_Y \sin \alpha_x \sin \alpha_y \tan \beta'_{AP'} \tan \beta'_{L'} - \sin \alpha_y \tan \beta'_{L'} q_{X'} - q_Y \sin \alpha_y \sin \alpha_x \tan \beta'_{L'} \tan \beta'_{AP'}}{(1 + \sin \alpha_x \sin \alpha_y \tan \beta'_{AP'} \tan \beta'_{L'})} \quad (2.87)$$

$$q_y = \frac{q_Y - q_{X'} \sin \alpha_y \tan \beta'_{L'}}{1 + \sin \alpha_x \sin \alpha_y \tan \beta'_{AP'} \tan \beta'_{L'}} \quad (2.88)$$

Eq. (2.86) and Eq. (2.88) can be used to obtain q_x and q_y by using $q_{X'}$, q_Y and α_x , α_y .

2.2.2. Using Point Data to Transfer Oblique Data to Normal

Nearly all the AP and L parameters of the mathematical model can be obtained from the reference points ($G, G', K, G'_1, G''_1, G_1$) given in Figure 2.14. In this part, the coordinates of the reference points in AP' and L' views will be transferred to the AP and L views and then the coordinate of these points will be used to calculate the input parameters of the mathematical model.

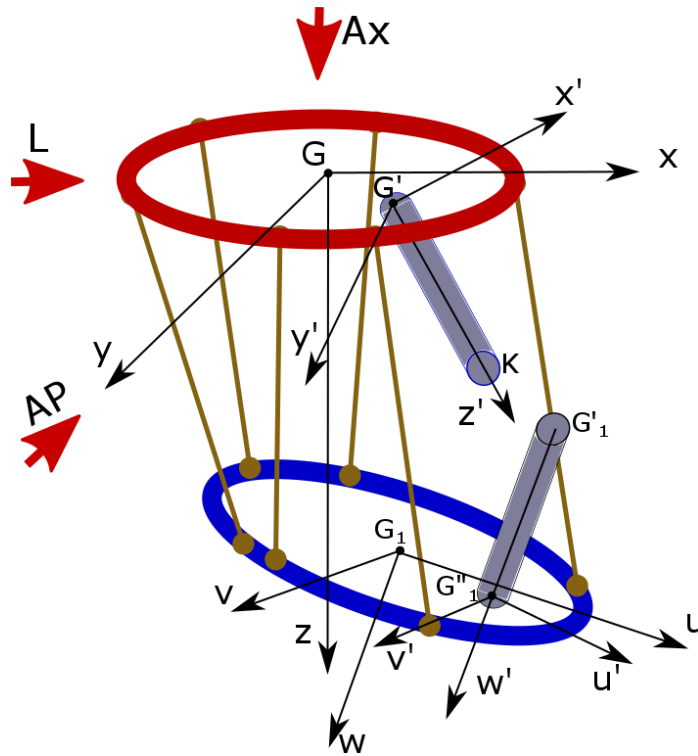


Figure 2.14. View – Position relations and reference Points

Starting from the same transformations and the relationship between L' and L given in Section 2.2.1.1, and between AP' and AP given in Section 2.2.1.2, the transformation can be defined for the points. The coordinates which can be obtained from each view are given as:

L' view : (C_Y, C_Z)

AP' view : $(C_{X'}, C_{Z'})$

If Eq. (2.53) is substituted in Eq. (2.48):

$$C_{X'} = \cos \alpha_y C_X + \sin \alpha_y C_Z \quad (2.89)$$

C_X can be written as:

$$C_X = \frac{1}{\cos \alpha_y} (C_{X'} - \sin \alpha_y C_Z) \quad (2.90)$$

the obtained C_X value is substituted in Eq. (2.50) to derive c_z as:

$$c_z = -\frac{\sin \alpha_y}{\cos \alpha_y} (C_{X'} - \sin \alpha_y C_Z) + \cos \alpha_y C_Z \quad (2.91)$$

$$c_z = -\tan \alpha_y C_{X'} + \tan \alpha_y \sin \alpha_y C_Z + \cos \alpha_y C_Z \quad (2.92)$$

$$c_z = -\tan \alpha_y C_{X'} + C_Z (\tan \alpha_y \sin \alpha_y + \cos \alpha_y) \quad (2.93)$$

Similarly, c_y can be used to derive another definition of c_z . For this, Eq. (2.49) is substituted in Eq. (2.54):

$$C_Y = \cos \alpha_x C_{Y'} - \sin \alpha_x C_{Z'} \quad (2.94)$$

$C_{Y'}$ is obtained as:

$$C_{Y'} = \frac{1}{\cos \alpha_x} (C_Y + \sin \alpha_x C_{Z'}) \quad (2.95)$$

The obtained $C_{Y'}$ substituted in Eq. (2.55) to derive c_z :

$$c_z = \frac{\sin \alpha_x}{\cos \alpha_x} (C_Y + \sin \alpha_x C_{Z'}) + \cos \alpha_x C_{Z'} \quad (2.96)$$

$$c_z = \tan \alpha_x C_Y + \tan \alpha_x \sin \alpha_x C_{Z'} + \cos \alpha_x C_{Z'} \quad (2.97)$$

$$c_z = \tan \alpha_x C_Y + C_{Z'} (\tan \alpha_x \sin \alpha_x + \cos \alpha_x) \quad (2.98)$$

Hence all the c_x, c_y, c_z values are obtained as:

$$c_x = C_{X'} \quad (2.99)$$

$$c_y = C_Y \quad (2.100)$$

$$c_z = -\tan \alpha_y C_{X'} + C_Z (\tan \alpha_y \sin \alpha_y + \cos \alpha_y) \quad (2.101)$$

or

$$c_z = \tan \alpha_x C_Y + C_{Z'} (\tan \alpha_x \sin \alpha_x + \cos \alpha_x) \quad (2.102)$$

2.2.3. Graphical User Interface to Test the Oblique View Theory

To test the algorithms, a set of theoretical oblique test data is generated from the currently available normal data. To create the test data, the normal data is written as vectors between reference points. Then, these vectors are transformed to L' and AP' system.

For data creation and the testing of the algorithm, a GUI has been prepared (Figure 2.15). The GUI has the following items: **1** – Input Vectors, **2** – Transformed vectors, **3** – Point coordinates to test Section 2.2, **4** – Theoretical data in oblique plane, **5** – Result of the algorithm: Normal Data, **6** – Rotation angles, **7** – Control Buttons.

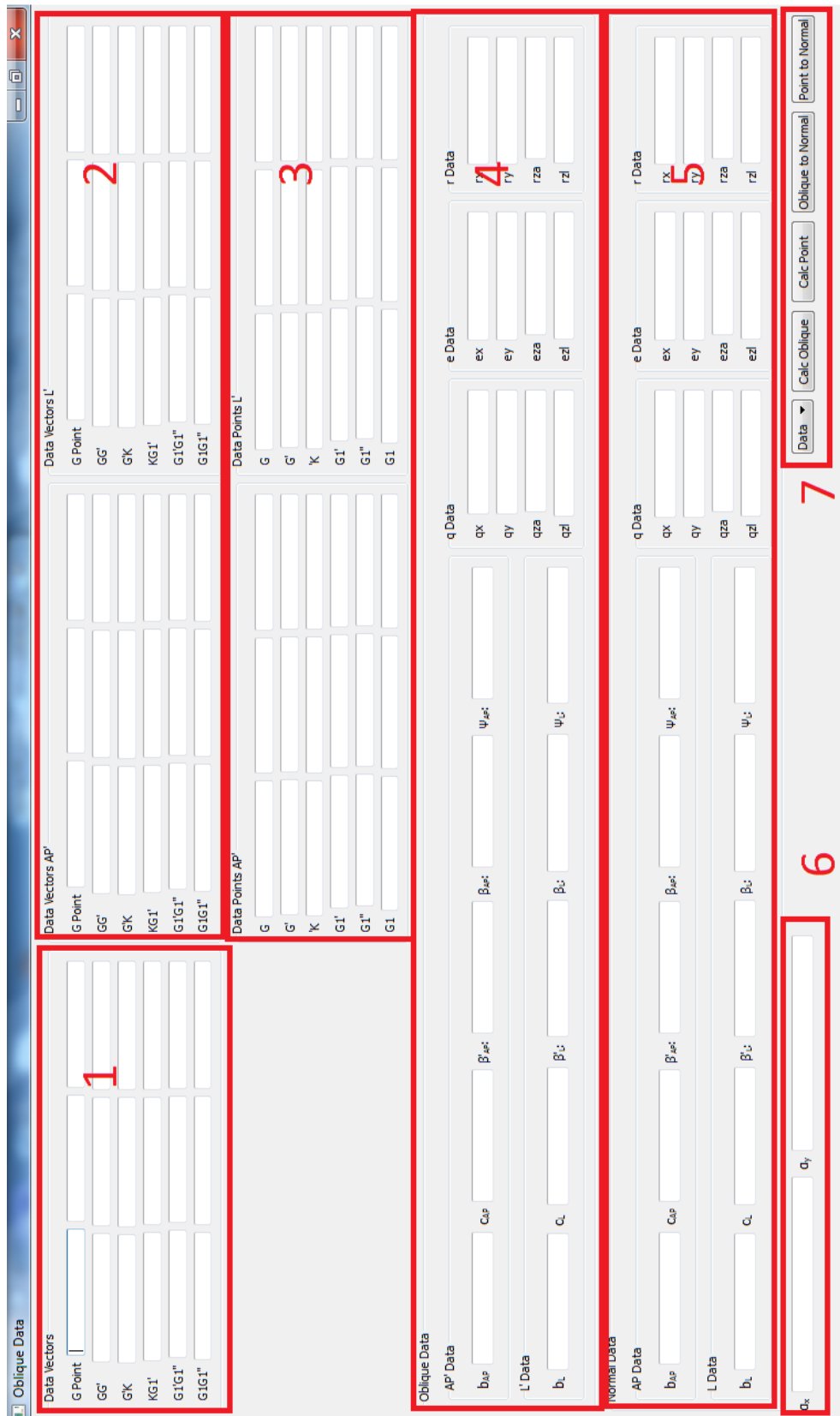


Figure 2.15. Data creation and algorithm test GUI

Currently seven theoretical data sets, which are created synthetically, are available for testing. The algorithms are tested with these data sets and validated.

With this study, the mathematical model is extended to cover the oblique view case. The calculations given in this section are used to transform the data measured from oblique view to the normal view. Then, the normal view theory is used for final calculations. The developed algorithms are tested and validated, and they can be used on real X-Ray image data.

The ability to handle the oblique view case increases the usability of the external fixator. With that, we have removed the constraint that the proximal fixator ring should be seen as a line which may be hard to achieve for the X-Ray technician.

3. A NOVEL EXTERNAL FIXATOR: THE LAMBDA FIXATOR

3.1. Motivation for the New Design

As a part of this ongoing project, different external fixator configurations have been considered. The configuration described in Chapter 2 has been studied in detail since it has certain advantages over the existing systems (as described in Chapter 1). Despite the fact that the developed system eliminates some shortcomings of the existing systems, we have realized that an improved configuration is still possible. In the system developed previously, we check mathematically if the treatment procedure encounters a singular configuration or not. The natural question that arises next is whether a singularity-free configuration is possible.

The main motivation for the new design is to develop a singularity-free fixator configuration while maintaining the advantages of the previous configuration. The *lambda fixator* constitutes a design with these properties and its mathematical theory is described in this chapter. As an additional advantage, lambda fixator seems to block the bone images less on the X-ray films compared to our previous design.

3.2. Inverse Kinematic Studies of the Lambda Fixator

Since the inverse kinematics of the lambda fixator also involves mainly the transformations between different coordinate systems defined on both rings, its theory is basically the same as outlined in Section 2.1.1. Once, the ring positions for non-aligned and aligned situations are determined, the strut lengths can be calculated. Using the strut lengths and simple geometrical considerations, the lengths of support rods can also be found.

3.2.1. Development of the Mathematical Model

In the lambda fixator, the rings are connected by three lambda modules (Figure 3.1). The lambda module consists of one long strut that is supported by a shorter rod (Figure 3.2 (a)). The module is symbolized with simple mechanical elements and a naming convention is determined (Figure 3.2 (b)). The total length of the strut (L') is composed of a constant length component (s) and a variable length component (l). The support rod and the short connection element have constant lengths, denoted as L'' and e , respectively (Figure 3.2 (b)). Finally the connection points between the lambda module and the rings are named with (A_i) and (B_i) for proximal and distal rings, respectively.

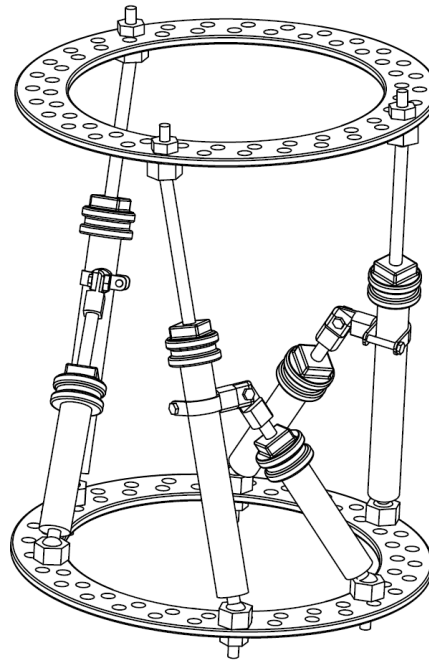


Figure 3.1. Lambda fixator.

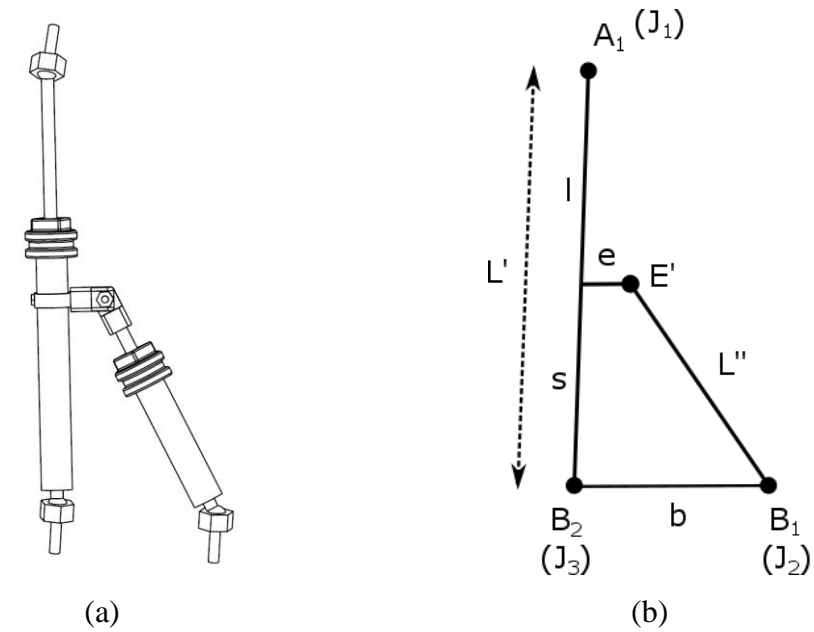


Figure 3.2. (a) Lambda module and (b) naming convention used during calculations.

Note that the variable length component of the strut can be connected to the distal or the proximal ring. Similarly, the support rod can be located on the left or on the right of the strut, and/or connected to the proximal ring or distal ring. In other words, a lambda module can be mounted in eight different ways to the rings (Figure 3.3). For the lambda fixator possessing three lambda modules, this results to $8^3=512$ different possible configurations. Yet, as pointed out earlier, once the relative ring positions are quantified, the strut lengths of each lambda module is also set. If the strut length of a lambda module is known, other related quantities can be computed depending on in which configuration the considered module is mounted (Figure 3.3). Hence, it suffices to analyze kinematically the 8 possible configurations of the lambda module.

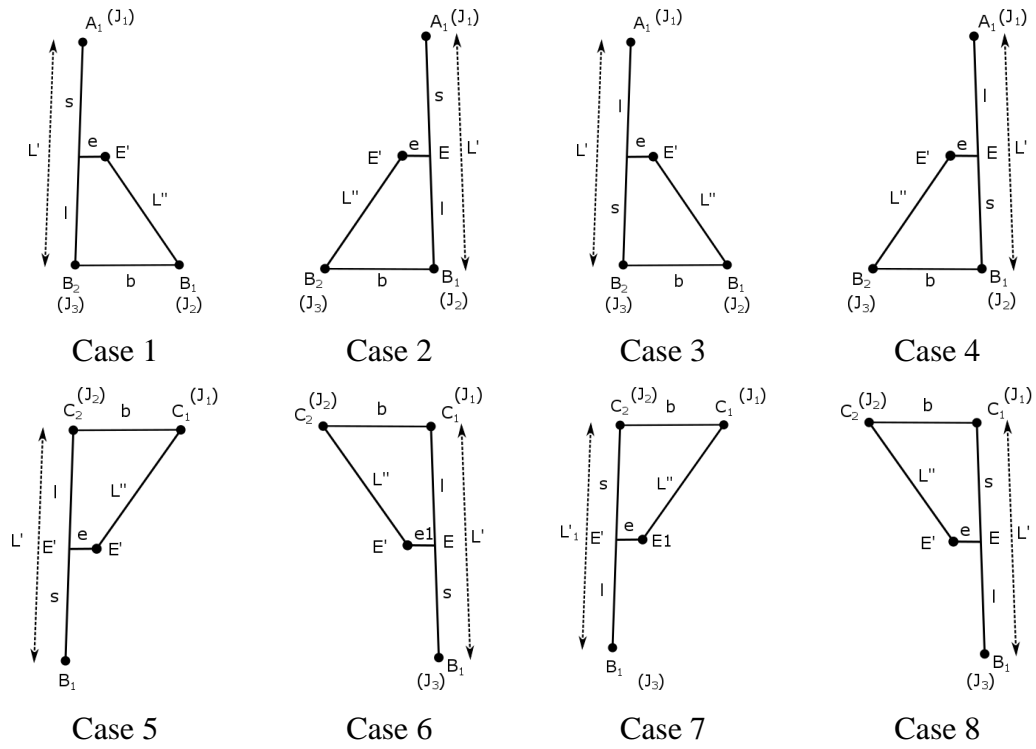


Figure 3.3. Eight different connection types.

For each lambda module, 5 inputs are needed to calculate the rod lengths of the module: two of them comes from the physical dimensions of the lambda module (e, s) and three of them are the position of the joints that connects the lambda module to the fixator rings (J_1, J_2, J_3). (e) is the junction length that connects the support rod to the strut and (s) is the fixed length of the strut.

3.2.2. Calculation of Strut and Rod Lengths

The calculation of strut and rod lengths involve similar steps for all eight cases. Here, we will summarize this calculations.

Let a strut be connected to the joint J_p on the proximal and J_d on the distal ring. The angular positions of J_p and J_d are represented with angles α and ϵ for proximal and distal rings, respectively (see Section 2.1.2).

The global coordinate system (xyz –system) is fixed to the proximal ring. Hence, we can directly calculate the global coordinates of J_p , $(x_p, y_p, 0)$, from α values and the proximal ring radius.

The coordinates of J_d are calculated first in the local coordinate system (uvw –system) located at the center of the distal ring, using the ϵ values and the distal ring radius. The local coordinates $(u_d, v_d, 0)$ are then transformed to the global coordinates (x_d, y_d, z_d) using the transformation matrix $[A_{xyz}^{uvw}]$ (Section 2.1.1) as:

$$\overrightarrow{G_1J_d} = \begin{bmatrix} x_d \\ y_d \\ z_d \end{bmatrix} = [A_{xyz}^{uvw}] \begin{bmatrix} u_d \\ v_d \\ 0 \end{bmatrix} \quad (3.1)$$

By using the distance vector between proximal and distal ring centers ($\overrightarrow{GG_1}$), the distance vector between proximal ring center and J_d is obtained as:

$$\overrightarrow{GJ_d} = \overrightarrow{GG_1} + \overrightarrow{G_1J_d} \quad (3.2)$$

The strut vector (from proximal to distal) is given as:

$$\vec{L}' = \begin{bmatrix} x_d - x_p \\ y_d - y_p \\ z_d - 0 \end{bmatrix} \quad (3.3)$$

whose magnitude L' is the strut length.

Define the unit vector $\vec{u}_{L'}$ along \vec{L}' as:

$$\vec{u}_{L'} = \frac{\vec{L}'}{L'} \quad (3.4)$$

With Eq. (3.4), we can define the vectors along the constant-length and variable-length parts of the strut as:

$$\vec{s} = s\vec{u}_{L'} \quad (3.5)$$

$$\vec{l} = l\vec{u}_{L'} \quad (3.6)$$

Note that $s + l = L'$. The vector \vec{b} , (going from the strut joint to the support rod joint) can be easily found from the support rod joint coordinates.

The segment e , connecting the strut to the support rod, is always perpendicular to the strut. To find the vector along e , first, we need a unit vector perpendicular to both \vec{b} and $\vec{u}_{L'}$. Define the unit vector along \vec{b} as:

$$\vec{u}_b = \frac{\vec{b}}{b} \quad (3.7)$$

The normalized cross product of $\vec{u}_{L'}$ with \vec{u}_b , given as:

$$\vec{n} = \frac{\vec{u}_{L'} \times \vec{u}_b}{|\vec{u}_{L'} \times \vec{u}_b|} \quad (3.8)$$

is a unit vector perpendicular to e as well. The cross product of \vec{n} with $\vec{u}_{L'}$ will produce the unit vector along e , namely \vec{u}_e :

$$\vec{u}_e = \vec{n} \times \vec{u}_{L'} \quad (3.9)$$

with which e can be written as

$$\vec{e} = e\vec{u}_e \quad (3.10)$$

At this point, all necessary vectors are quantified. Depending on which of the eight configurations is at hand, the length of the support rod L'' is calculated by one of the below equations:

$$L'' = |\vec{b} + \vec{s} - \vec{e}| \quad (3.11)$$

or

$$L'' = |\vec{b} + \vec{l} - \vec{e}| \quad (3.12)$$

The developed GUI applies the correct computation once the configuration of a lambda module is specified by the user.

3.2.3. The Graphical User Interface for Inverse Kinematic Algorithm Calculations of Lambda Fixator

For the calculations of the theory developed in Section 3.2, a GUI is developed (Figure 3.4). Some of the data is obtained from the measurements on the Anterior-Posterior and Lateral X-ray images (Figure 3.4, (a), (b), (c), (d), (e)); the rest of the input data is of clinical nature and will be entered by the orthopedist (Figure 3.4, (i), (j), (k)). The test data is selected from drop-down menu and the “Calculate” button triggers the calculation process (Figure 3.4, (h)). The results seen in Figure 3.4, (f), (g) are used as control parameters. The final results of the calculations for rod lengths are given in Figure 3.4, (l). L_1, L_2, L_3 indicate the rod lengths of the modules 1, 2, and 3 respectively.

The angular positions (J_1, J_2, J_3) of each module and physical parameters (s) and (e) are entered in the related boxes shown in Figure 3.4, (l). The connection case of the module is chosen from the drop-down menu (Figure 3.5).

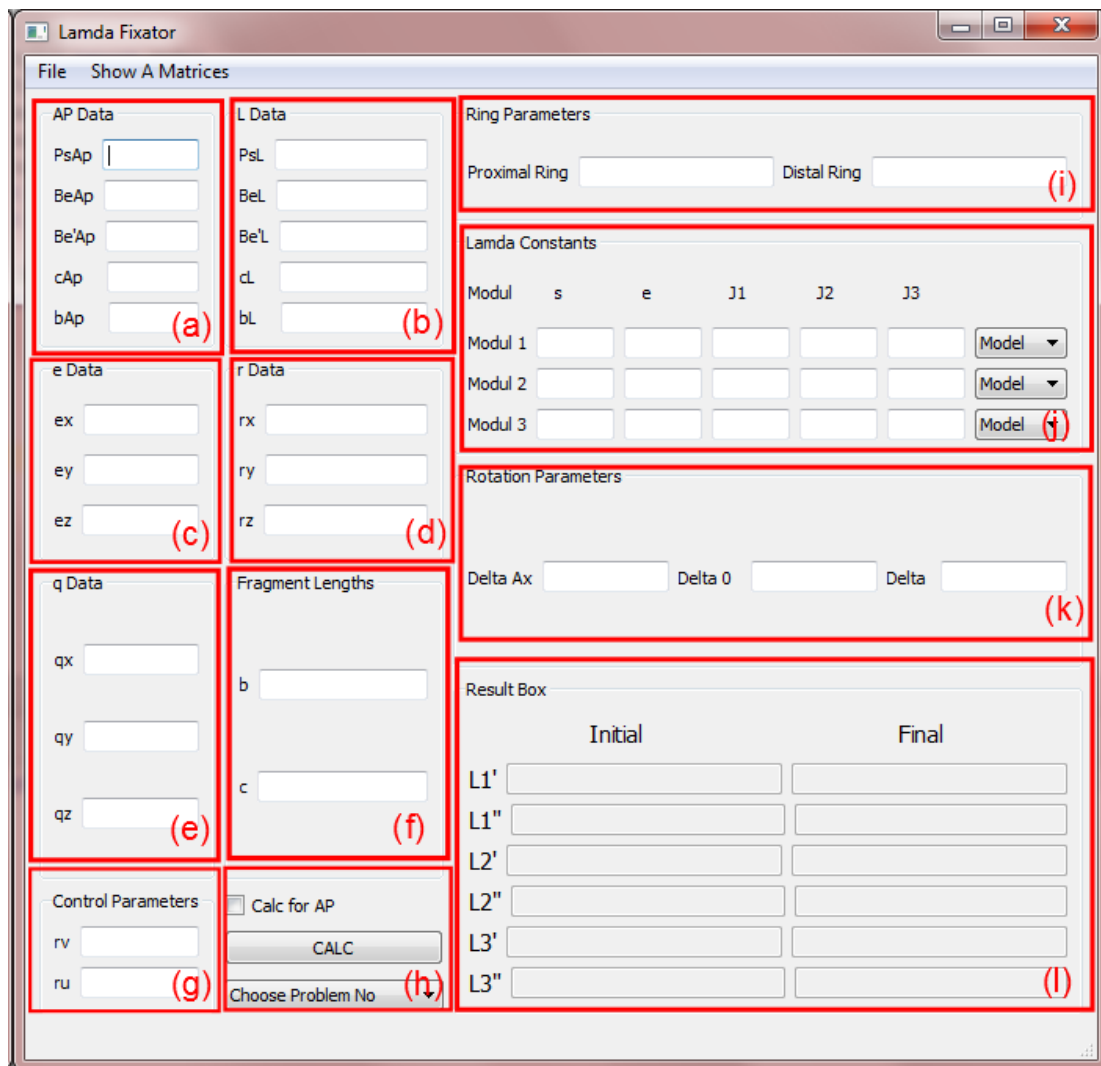


Figure 3.4. Graphical User Interface for inverse kinematic calculations of lambda fixator

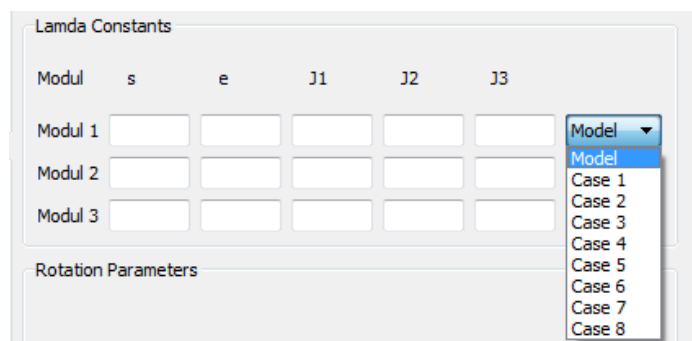


Figure 3.5. Connection case selection

3.2.4. Test of the Algorithm and GUI

To test the algorithm and the GUI, a synthetic problem is generated. A configuration of the fixator for initial (unaligned) and final (aligned) positions is prepared (Figure 3.6) and this configuration is used to test the algorithm and GUI. The GUI with the test data entered (Figure 3.7) produced expected results.

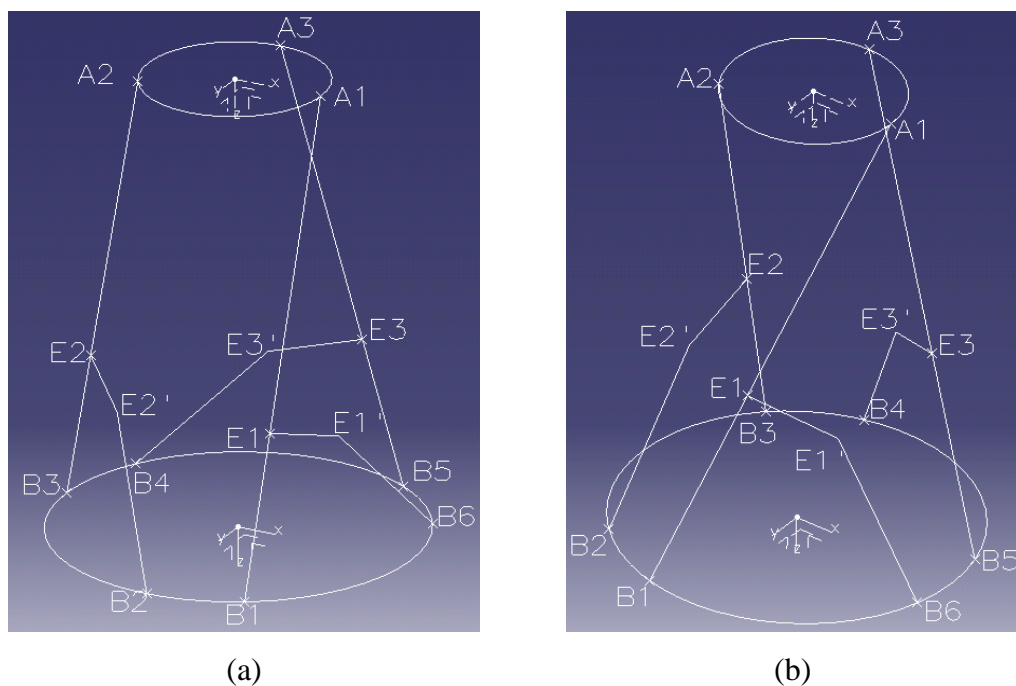


Figure 3.6. Configuration for initial (a) and final (b) positions of the lambda fixator.

Lamda Fixator

File Show A Matrices

AP Data

PsAp 0

BeAp 0

Be'Ap 0

cAp 10

bAp 15

L Data

PsL 0

BeL 0

Be'L 0

cL 10

bL 15

e Data

ex -0.7071

ey 0.2929

ez 2

r Data

rx 0

ry 1

rz 0

q Data

qx 0.7071

qy 0.7071

qz 0

Fragment Lengths

b 15.0

c 10.0

Control Parameters

Calc for AP

rv 0.70710678118

ru 0.70710678118

CALC

Lamda Numeric

Ring Parameters

Proximal Ring 5

Distal Ring 10

Lamda Constants

Modul	s	e	J1	J2	J3	
Modul 1	17.63834	5.291502	0	330	60	Case 1
Modul 2	17.17100	5.151300	150	90	180	Case 1
Modul 3	17.17100	5.151300	270	210	300	Case 1

Rotation Parameters

Delta Ax 45

Delta 0 45

Delta 0

Result Box

	Initial	Final
L1	29.6628033825	26.457510891
L1'	10.1831336926	9.21529442246
L2	28.7770411177	25.7565054001
L2'	10.7074708137	10.1878472698
L3	28.7770411177	25.7565028964
L3'	10.7074708137	10.1878514524

Figure 3.7. Test data and results

4. COMPLETION OF BONE IMAGE

4.1. Introduction

In the treatment with a ring fixator, typically, one X-ray of the bone is taken before installing the fixator (*pre-operative* image) and one after the installment of the fixator (*post-operative* image). In the post-operative image, the tip of the bone fragments and the intersection of their axes with ring planes should be visible on the X-ray film in order to be able to read certain parameters. Yet, the view of the external fixator may block the view of bone fragments making it difficult to measure these parameters. To compensate for the visual data loss caused by the presence of the fixator, we have developed some image processing tools that make use of the pre-operative X-ray images to partially restore the bone in the post-operative image.

In this approach, first, both pre-operative and post-operative images (i.e. images with and without the fixator) are segmented to distinguish the bone, fixator and the background from each other. Next, the visible parts of the bone fragments in the bone-fixator image are grouped together. Finally, a matching algorithm is applied to register the bone fragments on both images. The applied algorithm consists of several steps (Figure 4.1) as explained in detail in this chapter.

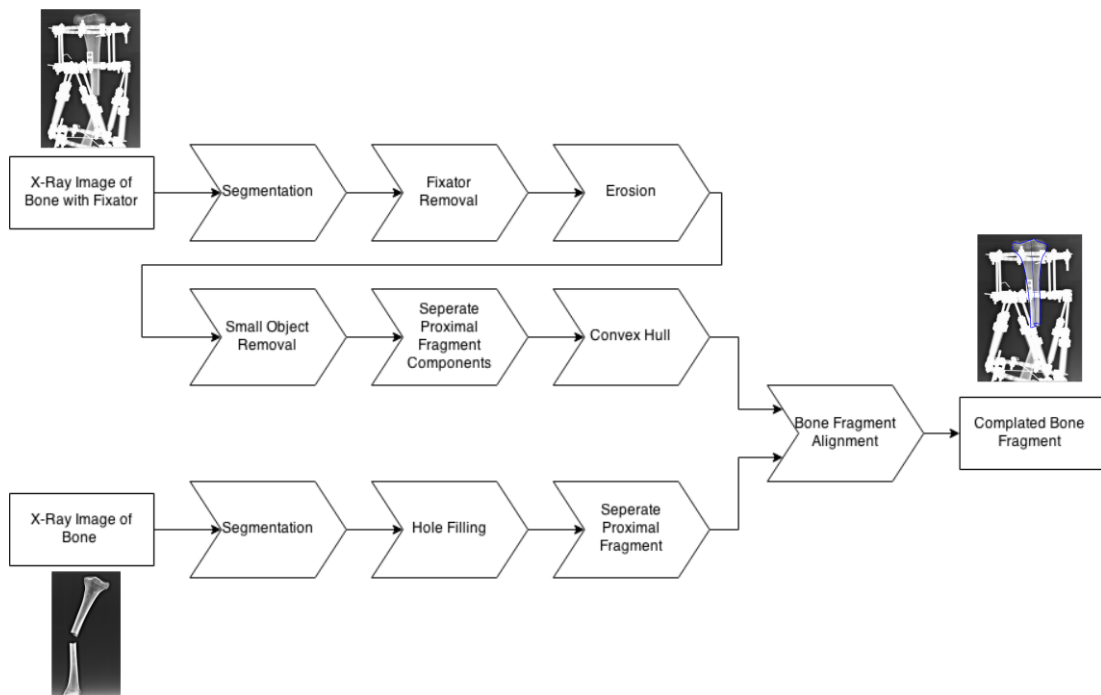


Figure 4.1. Flowchart of the bone image completion procedure

4.2. Segmentation of the Bone and the External Fixator

The segmentation procedure is applied to both pre-operative and post-operative images. 16 different segmentation methods are tested on 77 different X-ray images. The tested methods are:

1. IsoData (Ridler and Calvard, 1978): This methods has the setting of ignoring the white and/or black pixels. Therefore, the different settings are accepted as different methods,
2. Huang's Fuzzy Thresholding Method (Huang and Wang, 1995)
3. Intermodes Thresholding (Prewitt and Mendelsohn, 1966)
4. Li's Minimum Cross Entropy (Li and Tam, 1998)
5. Kapur-Sahoo-Wong (Maximum Entropy) Thresholding Method (Kapur et al., 1985)
6. Mean of Gray Levels Thresholding (Glasbey, 1993)
7. Kittler and Illingworth's Minimum Error Thresholding (Kittler and Illingworth, 1986)

8. Minimum Thresholding Method (Prewitt and Mendelsohn, 1966)
9. Moment-preserving Thresholding (Tsai, 1985)
10. Otsu Thresholding (Otsu, 1979)
11. Percentile Thresholding (Doyle, 1962)
12. Renyi Entropy Method (Kapur et al., 1985)
13. Shanbhag Method (Shanbhag, 1994)
14. Triangle Method (Zack et al., 1977)
15. Yen's Thresholding Method (Yen et al., 1995)

Two different examples are given to compare the performance of these algorithms. The first example involves the segmentation of bone from soft tissue (Figure 4.2). In the second example, the external fixator is segmented from bone and soft tissue (Figure 4.3). We have observed that, for most of the input images processed, the Minimum Thresholding Method performs better than the others (Figure 4.4-5).



Figure 4.2. Input image used to segment bone from soft tissue.



Figure 4.3. Input image used to segment the external fixator from bone and soft tissue.

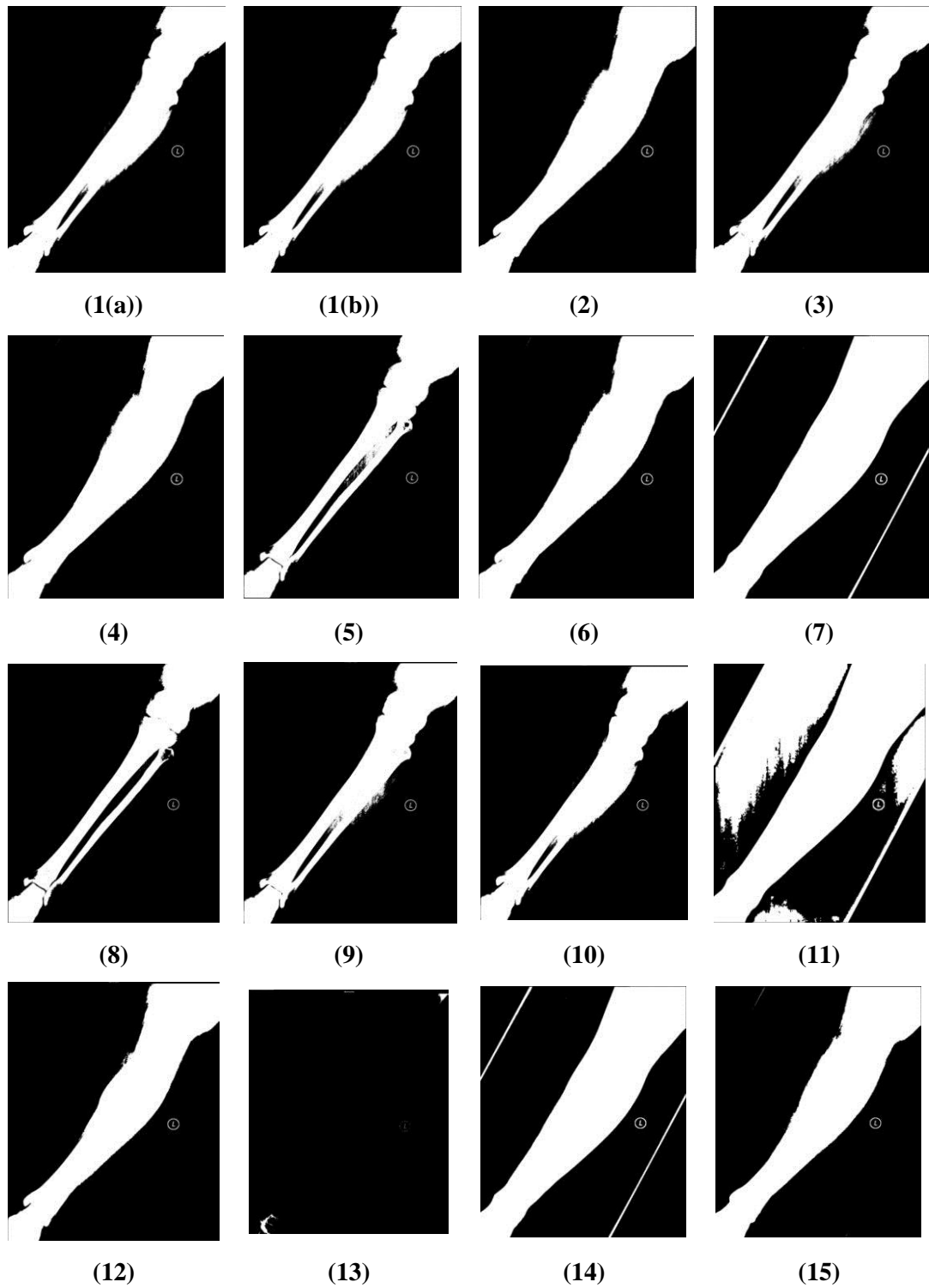


Figure 4.4. Results for segmentation of the bone from the soft tissue. The numbers indicate the test method.

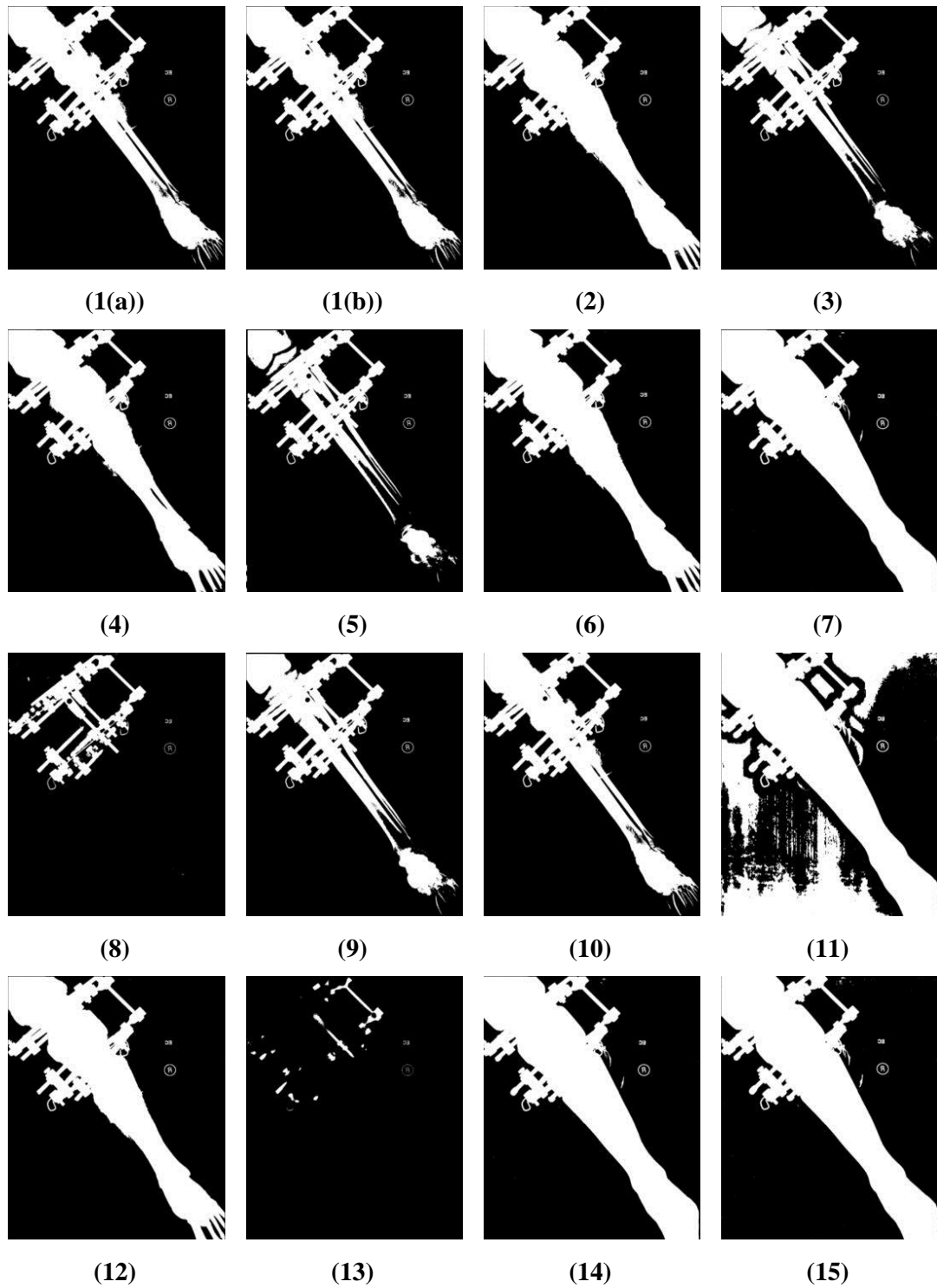


Figure 4.5. Results for segmentation of the fixator from rest of the image. The numbers indicate the test method.

The level of radiation exposure may be differently adjusted in different X-ray machines, which causes different intensities for the fixator and makes the X-ray images difficult to be automatically segmented. In such cases, the optimum threshold value for segmentation is determined manually using a simple developed GUI (Figure 4.6). Using the GUI, the threshold value for segmentation can be changed with a slider and the segmentation result is seen superposed with the original image (Figure 4.7).

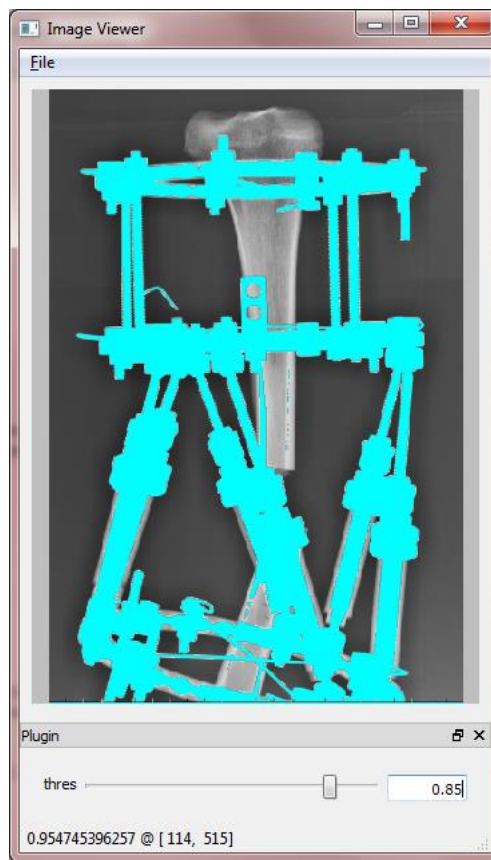


Figure 4.6. Interactive threshold selection in the GUI.

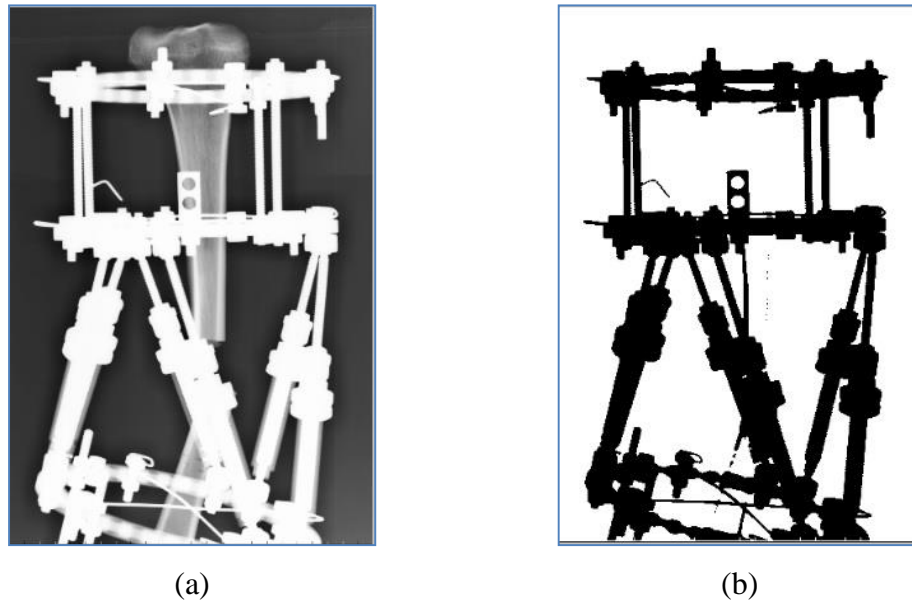


Figure 4.7 (a) The original input image and (b) the segmented fixator (image inverted for better visualization)

4.3. Removing the Fixator in the X-ray Image

The segmented fixator is used as a mask and the input image is filtered to remove the fixator to leave only the bone fragments in the image (Figure 4.7 (b)). Not only have different structural parts different thicknesses in the fixator systems, but they also can be made of different materials (e.g. metal and composite). These factors lead for different fixator parts to different image intensity values, some of which may be close to the intensity of the bone. Therefore, if the threshold is set to a value that contains intensities of all fixator components, some parts of bone will be segmented together with the fixator parts. To overcome this problem, the threshold is set to a value such that only the main structure of the fixator is segmented and used for filtering. Correspondingly, there are some debris remaining from the fixator after filtering (Figure 4.8 (a)) which can be cleared to a great extent with morphological erosion (see Appendix A.3) (Figure 4.8 (b)). Finally, the last remaining pixel clusters are cleared with small object removal algorithm (see Appendix A.4) (Figure 4.9).

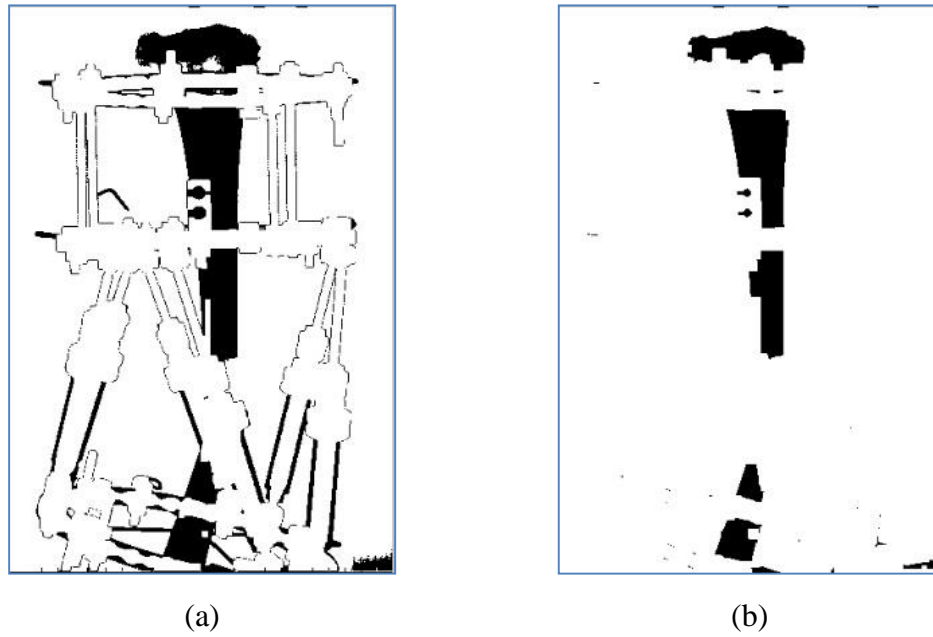


Figure 4.8. (a) The image after filtering the fixator and (b) the result of the morphological erosion (images are inverted for better visualization).

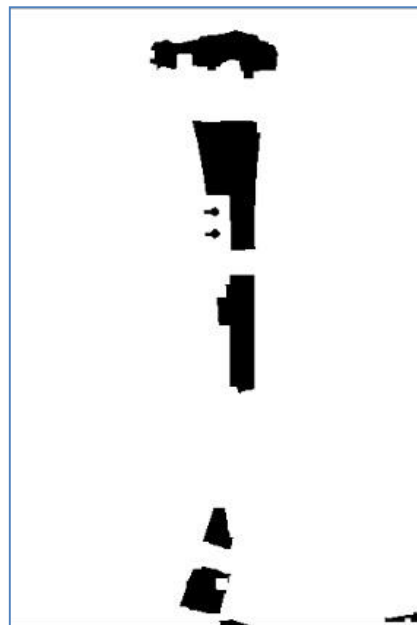


Figure 4.9. Result of the small object removal algorithm.

4.4. Combining Bone Parts through Convex Hull

The convex hull of a set of points is defined as the smallest convex polygon that includes all the points in this set. It is considered as the most efficient and non-ambiguous representation of the considered set of points. The convex hull concept is used in numerous applications such as robotics, pattern recognition and image processing. In robotics, it is used for collision detection (Kuffner et al., 2002), (Streinu, 2000) and for robotic grasping (Miller and Allen, 2004). In pattern recognition and image processing, it is mostly used for shape analysis applications (Du et al., 2007).

After the removal of the fixator, what remains from the bone image are some disjoint pixel clusters (Figure 4.9). These pixel clusters are combined with a convex hull to form a connected image of bone. In the image, the location of the fracture region is approximately indicated by the user after which the convex hulls of proximal and distal bone fragments are formed separately (Figure 4.10 (a,b)). Bone fragment images formed in this manner can be aligned with the pre-operative bone image.

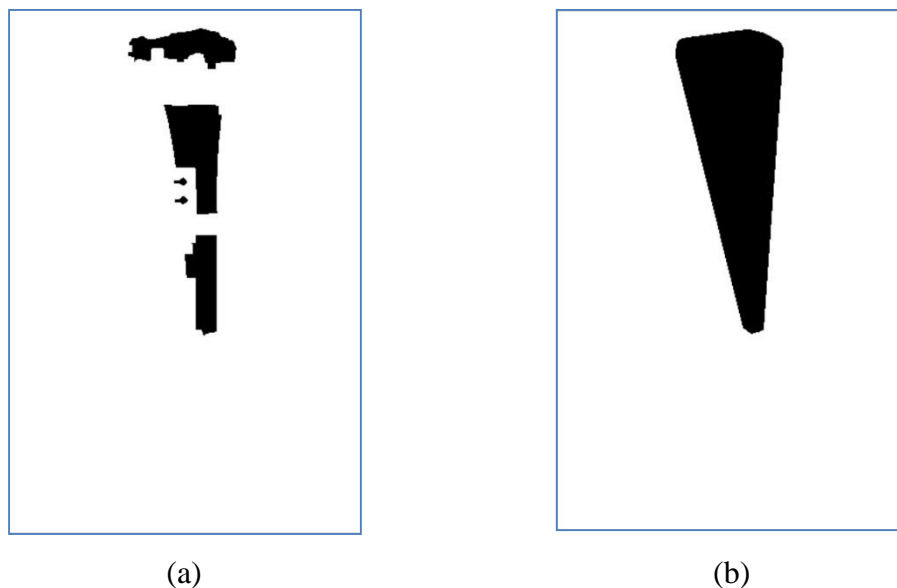


Figure 4.10. (a) Pixel clusters of proximal bone fragment and (b) the associated convex hull.

4.5. Alignment with Pre-operation Bone Fragments

4.5.1. Alignment using Grid Search

The convex hull representation of the bone fragments, described in the previous section, is aligned with the pre-operative bone fragment images.

The success of this procedure, where two images are matched, is measured with a metric that involves the number of overlapping foreground pixels in both images. However, the segmented bone fragments in the pre-operation image may have some areas that have the same intensity as the background (Figure 4.11 (a)). For a proper image matching, these *holes* must be filled (i.e. brought to bone intensity) before the alignment process, which is accomplished with a morphological hole filling algorithm (Soille, 2004) (Figure 4.11 (b)).



Figure 4.11. (a) The bone fragment segmented from pre-operation X-ray image and (b) the result of the hole filling algorithm.

The alignment process begins by computing the center of mass and the orientation for both pre-operative and post-operative bone images. The raw image moments are calculated as:

$$M_{ij} = \sum_x \sum_y x^i y^j I(x, y) \quad (4.1)$$

The x and y coordinates of the center of the mass (\bar{x}, \bar{y}) can be found as:

$$\bar{x} = \frac{M_{10}}{M_{00}}, \quad \bar{y} = \frac{M_{01}}{M_{00}} \quad (4.2)$$

Using central moments, the orientation of the bone fragments is given as:

$$\Theta = \frac{1}{2} \arctan \left(\frac{2\mu'_{11}}{\mu'_{20} - \mu'_{02}} \right) \quad (4.3)$$

where:

$$\mu'_{20} = \frac{M_{20}}{M_{00}} - \bar{x}^2 \quad (4.4)$$

$$\mu'_{02} = \frac{M_{02}}{M_{00}} - \bar{y}^2 \quad (4.5)$$

$$\mu'_{11} = \frac{M_{11}}{M_{00}} - \bar{x}\bar{y} \quad (4.6)$$

After the mass center and orientation of bone fragments from both images are obtained, an alignment process, based on a grid search algorithm, is applied. The process is initialized by overlaying the pre-operative bone and the post-operative bone images such that their mass center and orientation overlap. Starting from this position, the pre-operative image is translated in $\pm x$ and $\pm y$ directions in 2 pixel increments such that its mass center moves in $[-10,10]$ pixel xy -coordinate range with respect to the mass center of the post-operative image. At each new position, the pre-operative image is rotated in 1 degree increments in $[-5,5]$ degrees range. The overlap between the images are calculated at each new position/orientation and the position/orientation with the maximum overlap is selected. The contour and axis of the pre-operative bone fragment is drawn on the post-operative image (Figure 4.12). The result of the

alignment process shows that it is possible to use the pre-operative image to complete the missing parts of the bone fragments in the post-operative image when they are not visible enough to make measurements.

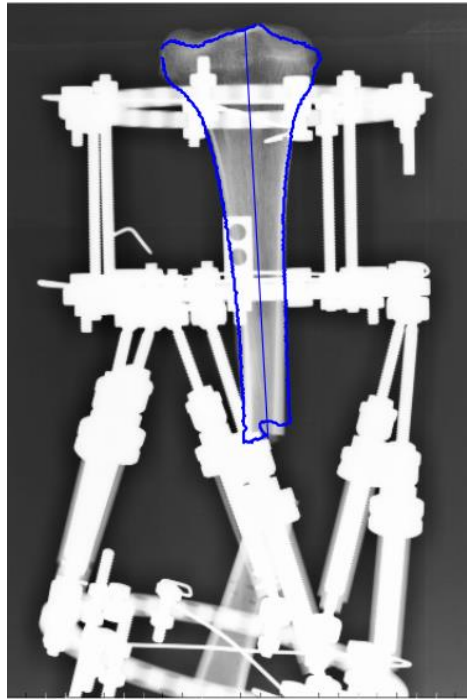


Figure 4.12. Result of the bone alignment process. The contour and center line obtained from pre-operation X-ray image is drawn on the fixator system image after alignment process (blue line).

4.5.2. Alignment using Bone Axes

In this method, the bone fragments in the pre-operative and the post-operative images are aligned by overlapping the bone axes in both images.

Let α is be the angle between the bone axes in the pre-operative and post-operative images. Similarly, let s be the ratio of the length of the bone axis segment (which is a measure for the fragment length) in the preoperative image to the same quantity in the post-operative image. Then, the pre-operative image pixels (x, y) can be transformed to the post-operative image pixels (x', y') as:

$$\begin{bmatrix} x' \\ y' \end{bmatrix} = s \begin{bmatrix} \cos \alpha & \sin \alpha \\ -\sin \alpha & \cos \alpha \end{bmatrix} \begin{bmatrix} x - x_d \\ y - y_d \end{bmatrix} \quad (4.7)$$

where (x_d, y_d) refers to the translation required to be applied in x and y directions to match the images. Note that all necessary parameters can be calculated by quantifying the bone axes in both images.

In this procedure, the pre-operative image is divided into two pieces across the osteotomy path to separate the distal and proximal fragment images from each other. Each fragment image is transformed with Eq. (4.7) to match its counterpart in the post-operative image.

An example, involving the shown pre-operative and post-operative images (Figure 4.13) is given here. After bone fragment axes and osteotomy paths are drawn on both images (Figure 4.14), the pre-operative image is divided into distal and proximal pieces across the osteotomy path (Figure 4.15) and each piece is aligned with the corresponding fragment on the post-operative image (Figure 4.16).

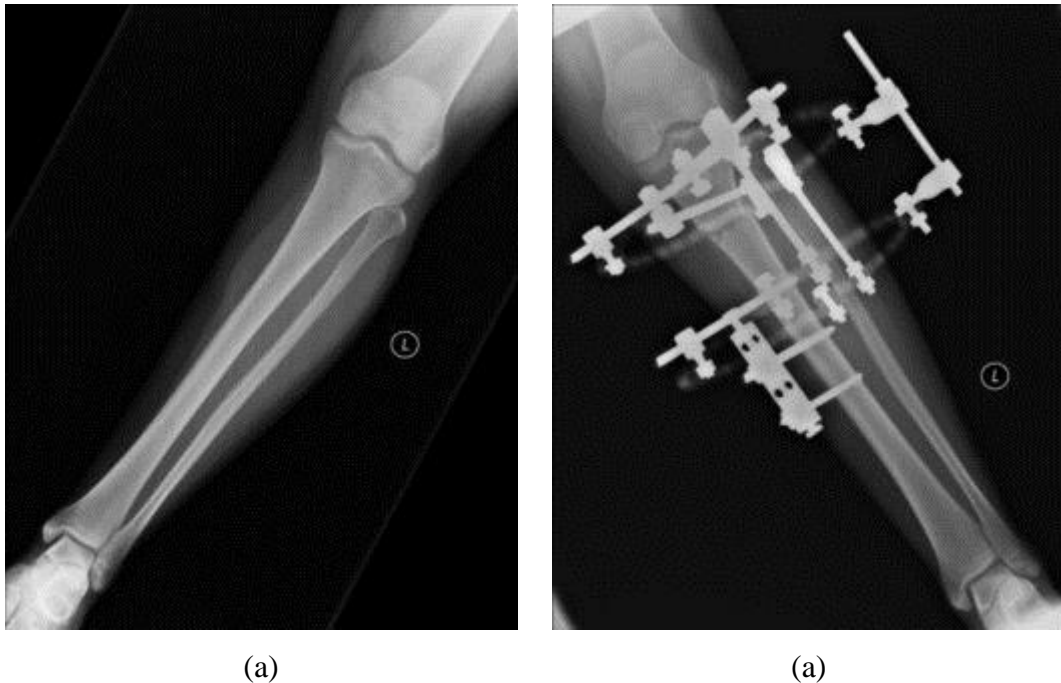


Figure 4.13 The (a) pre-operative and (b) post-operative images used

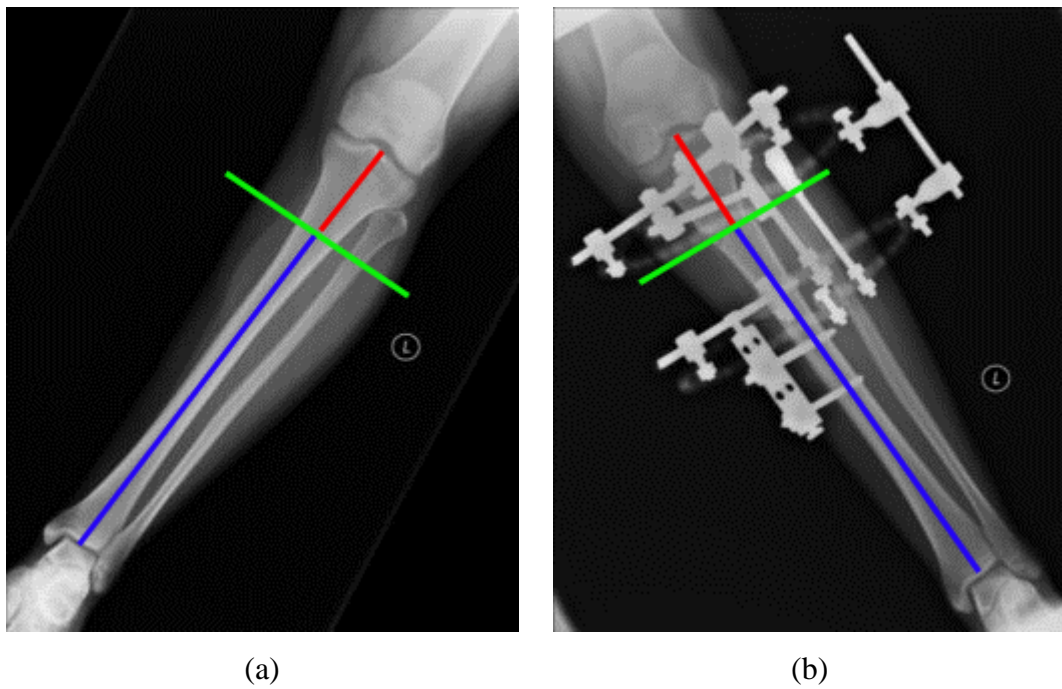


Figure 4.14 The bone fragment axes and osteotomy path drawn on the (a) pre-operative and (b) post-operative images.

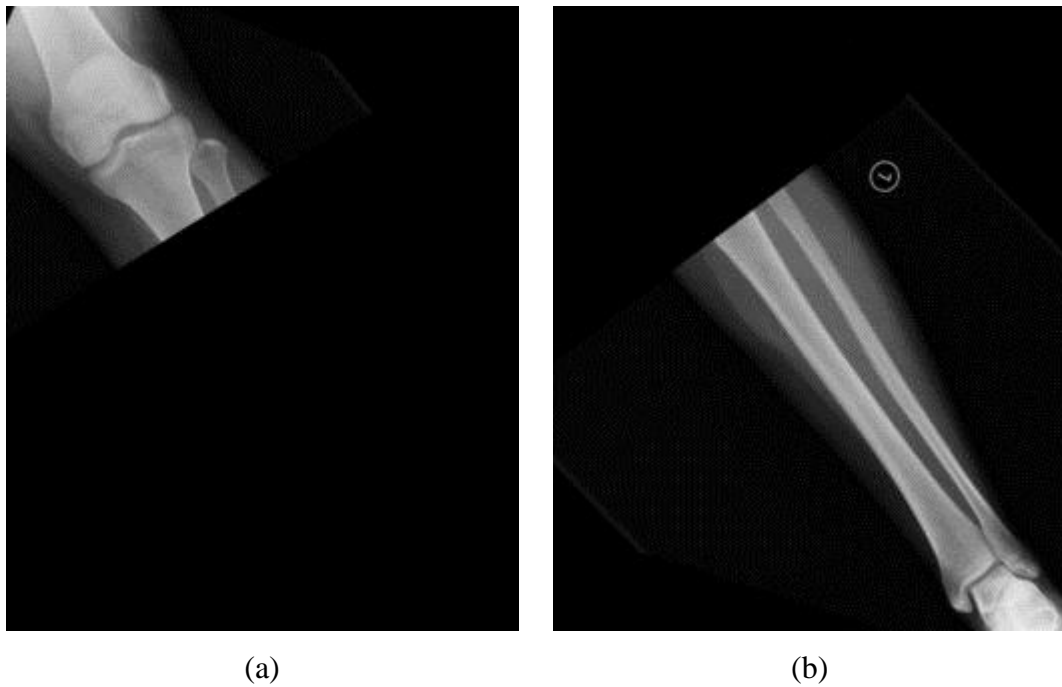


Figure 4.15 (a) Proximal and (b) distal fragments of the pre-operative image

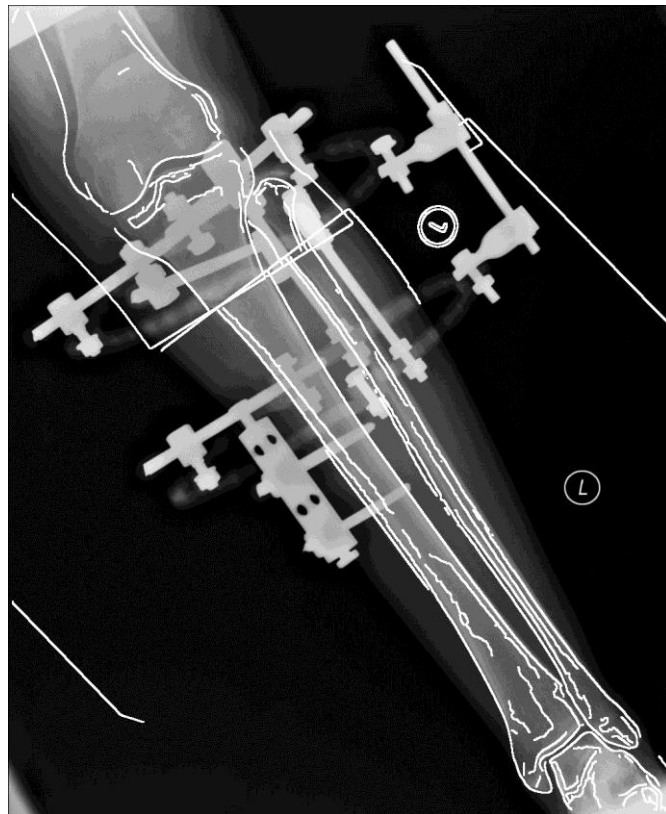


Figure 4.16 The edges of the aligned fragments drawn on the post-operative image.

5. LOCATING THE DISTAL RING IN THE FIXATOR IMAGE

5.1. Introduction

Certain geometric parameters, utilized in the mathematical model, are measured on the distal ring. Hence, it is important that the distal ring is identified properly on the X-ray image.

The distal ring usually appears as an ellipse in the X-ray images and it is located manually by the user in the existing systems. To automatize the measurements on the distal ring, we have developed an ellipse fitting approach which is described in this chapter. The procedure relies on locating the appropriate data points on the distal ring and fitting an ellipse on these points with or without a constraint related to the major axis of the ellipse.

5.2. Finding Interpolation Points on Distal Ring

Ellipse fitting is done with the data points known to be located on the distal ring. Those points are found with sequential image processing algorithms, as detailed in this section.

As the first step, the loaded image is resized to one quarter of its original size for faster processing and (if color image) converted to gray scale image. Using Otsu thresholding method (Otsu, 1979), the gray scale image is converted to a black-white image (Figure 5.1 (b)). Next, a morphological erosion operation (see Appendix A.3 for details) is applied to the image twice to trim big blocks from the image (Figure 5.2 (a)). After this operation, pixel clusters with an area larger than 50 pixels are removed from the image (Figure 5.2 (b)). The topmost coordinate of the distal ring is fed by the user as an input and pixel clusters, which has a median y coordinate larger than this user-picked coordinate, are used for ellipse fitting (Figure 5.3).

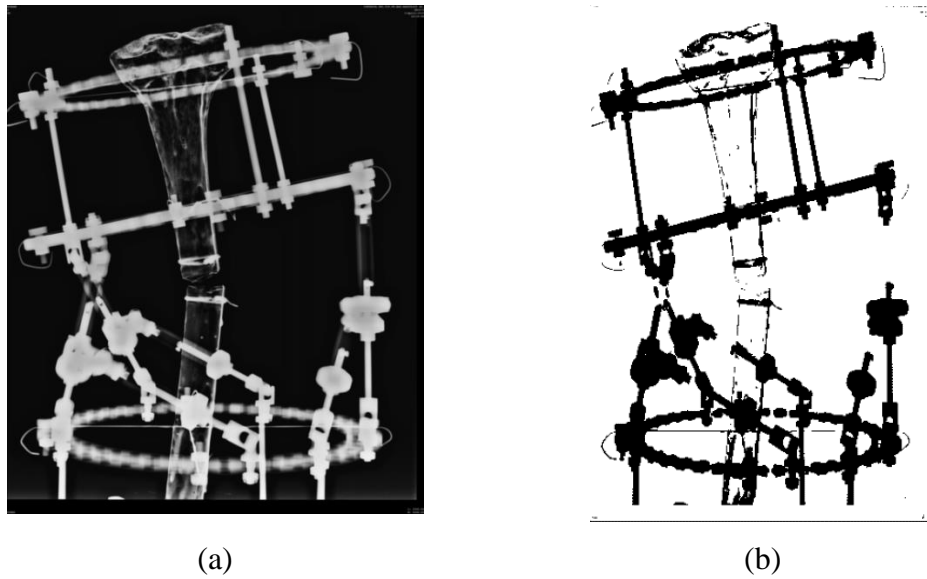


Figure 5.1. (a) Input image for ellipse fitting and (b) the output after Otsu Thresholding

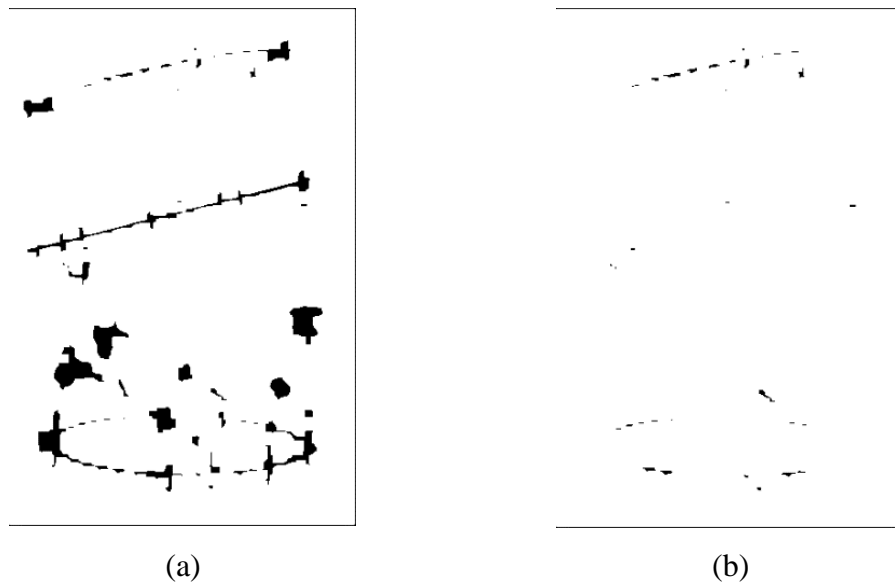


Figure 5.2. (a) The thresholded image after morphological erosion (b) and after the removal of the pixel clusters with area larger than 50 pixels.

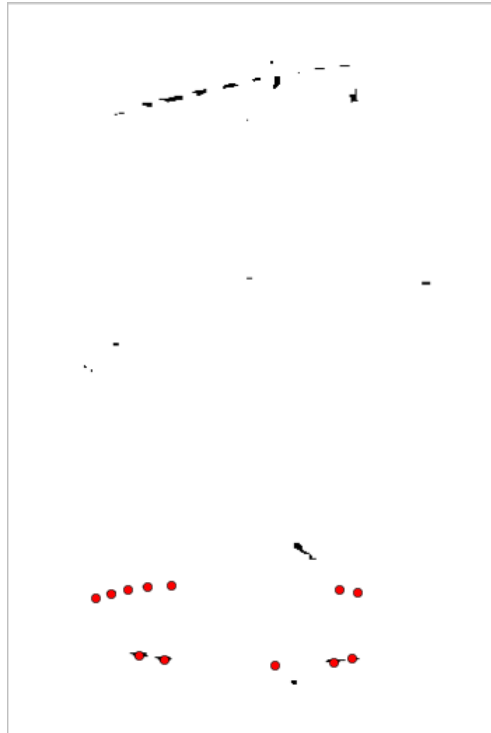


Figure 5.3. The obtained data points are shown with red dots

5.3. Ellipse Fitting without Major Axis Constraint

5.3.1. Direct Fitting Method

In this part, an approach involving the direct least square fitting of the ellipse (Fitzgibbon et al., 1999) is applied by using the reference points that are found (Section 5.2). The method is robust such that a proper ellipse can be fitted even with data that is less than ideal.

A general conic can be defined as

$$F(\mathbf{a}, \mathbf{x}) = \mathbf{a}\mathbf{x}^T = ax^2 + bxy + cy^2 + dx + ey + f = 0 \quad (5.1)$$

where $\mathbf{a} = [a \ b \ c \ d \ e \ f]$ and $\mathbf{x} = [x^2 \ xy \ y^2 \ x \ y \ 1]^T$. $F(\mathbf{a}, \mathbf{x})$ represents the algebraic distance of the data points to the conic. By minimizing the sum of squared algebraic distance of the curve to the n data points, namely,

$$D_A(\mathbf{a}) = \sum_{i=1}^n F(\mathbf{a}, \mathbf{x}_i)^2 \quad (5.2)$$

the parameter vector \mathbf{a} can be found. By using the parameter vector \mathbf{a} , the discriminant, $b^2 - 4ac$, is calculated. If $b^2 - 4ac < 0$, than this conic represents an ellipse.

In direct ellipse-specific fitting, the condition $b^2 - 4ac < 0$ is used as a constraint. However, this inequality constraint is hard to enforce. Note that Eq.(5.1) can be multiplied through with any constant and still remain correct, which means that we are free to scale the parameters as we wish. By exploiting this freedom to scale, the inequality constraint can be converted to an equality constraint. The equality constraint is chosen arbitrarily as $4ac - b^2 = 1$. This is a nonlinear constraint and can be expressed in matrix quadratic form as:

$$\mathbf{a}^T \mathbf{C} \mathbf{a} = 1 \quad (5.3)$$

where \mathbf{C} is given as:

$$\mathbf{C} = \begin{bmatrix} 0 & 0 & 2 & 0 & 0 & 0 \\ 0 & -1 & 0 & 0 & 0 & 0 \\ 2 & 0 & 0 & 0 & 0 & 0 \\ 0 & 0 & 0 & 0 & 0 & 0 \\ 0 & 0 & 0 & 0 & 0 & 0 \\ 0 & 0 & 0 & 0 & 0 & 0 \end{bmatrix} \quad (5.4)$$

Bookstein (Bookstein, 1979) showed that when a quadratic constraint, expressed in terms of the matrix \mathbf{C} , is set on the parameters, the given distance minimization can be achieved by solving the generalized eigenvalue problem:

$$\mathbf{D}^T \mathbf{D} \mathbf{a} = \lambda \mathbf{C} \mathbf{a} \quad (5.5)$$

where $\mathbf{D} = [\mathbf{x}_1 \ \mathbf{x}_2 \ \mathbf{x}_3 \ \dots \ \mathbf{x}_n]^T$ is the *design matrix* and \mathbf{x}_i are the vector \mathbf{x} evaluated at n data points.

The solution to Eq.(5.5) gives a set of eigenvalues λ and eigenvectors \mathbf{a} . The eigenvector \mathbf{a} , which corresponds to the only negative λ (which is -1 in this case), provides us the parameters that minimizes the error in Eq.(5.2). Since any constant multiple of \mathbf{a} is also an eigenvector, \mathbf{a} can be scaled to satisfy the constraint in Eq. (5.3). Define \mathbf{u} as:

$$\mathbf{a} = \mu \mathbf{u} \quad (5.6)$$

with this definition, Eq.(5.3) becomes:

$$\mu^2 \mathbf{u}^T \mathbf{C} \mathbf{u} = 1 \quad (5.7)$$

which can be solved for μ to give us the correct scaling factor:

$$\mu_i = \sqrt{\frac{1}{\mathbf{u}_i^T \mathbf{C} \mathbf{u}_i}} \quad (5.8)$$

5.3.2. Fitting with Least Squares Minimization

When an ellipse is fit on n data points with coordinates (x_i, y_i) , the residual of Eq.(5.1) for the i^{th} point is given as:

$$F(x_i, y_i, \mathbf{a}) = ax_i^2 + bx_iy_i + cy_i^2 + dx_i + ey_i + f \quad (5.9)$$

The total residual equals to:

$$E = \sum_{i=1}^n F(x_i, y_i, \mathbf{a})^2 \quad (5.10)$$

The least squares approach requires the total residual to be minimized with respect to the system parameters $\mathbf{a} = [a \ b \ c \ d \ e \ f]$:

$$\frac{\partial E}{\partial a_i} = 0 \quad (5.11)$$

This results to a set of six linear equations whose solution provides us the optimal parameter set.

5.3.3. Testing of the Direct Ellipse Fitting Algorithm

To test the direct ellipse fitting method (see Section 5.3.1), a simple GUI is programmed. The test data is created randomly by clicking on different part of the GUI and an ellipse is fitted (Figure 5.4). The algorithm has been tested also on reference points obtained from the X-Ray images of the Gough-Stewart platform external fixator and the lambda fixator (Figure 5.5).

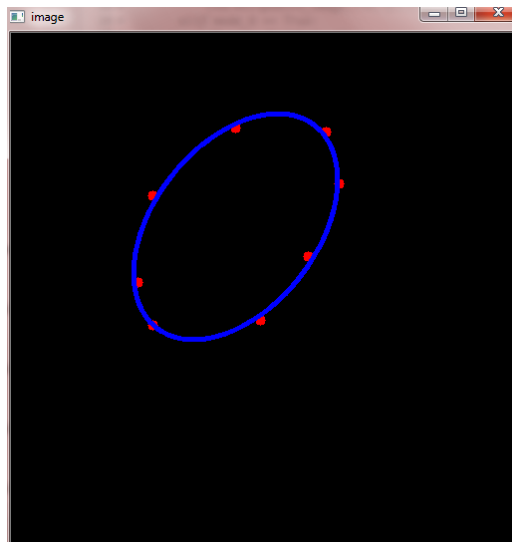


Figure 5.4. Result of the direct ellipse fitting method. By clicking on the screen, random points are created (red dots). An ellipse is fitted on these points (blue curve).

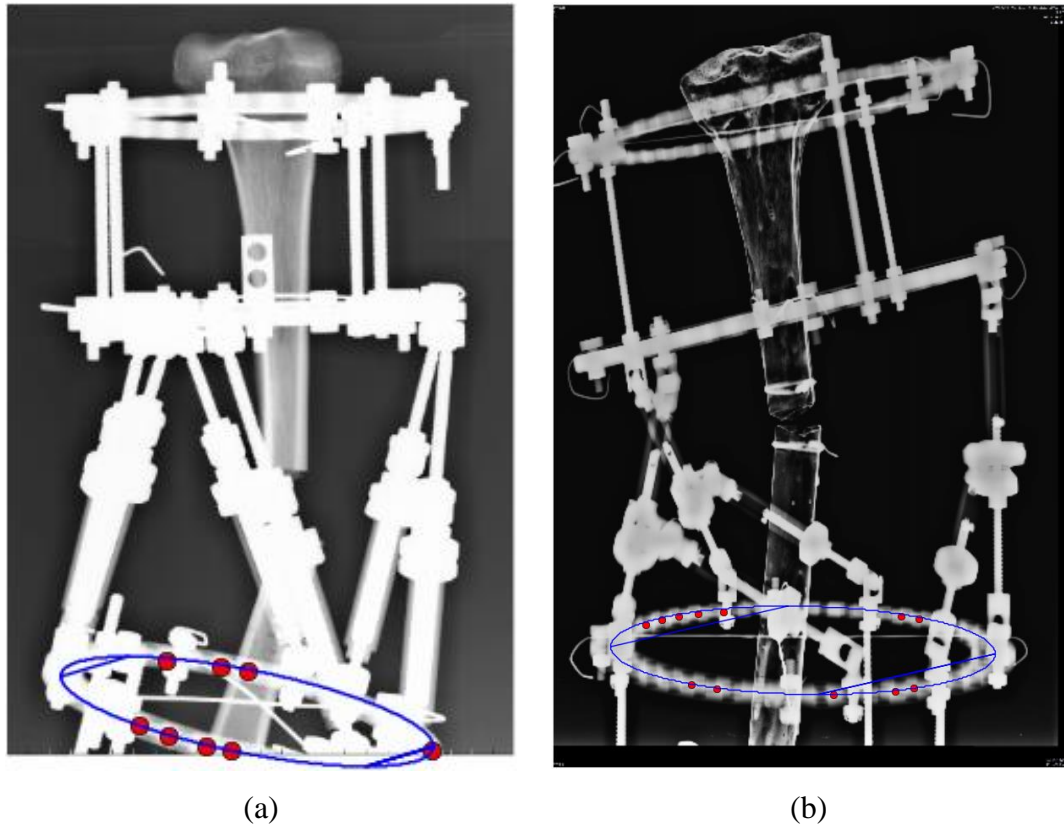


Figure 5.5. The result of the direct ellipse fitting method applied on reference points (shown in red) obtained at the image processing stage from (a) Gough-Stewart Platform External Fixator and (b) Lambda Fixator.

5.3.4. Testing of the Least Squares Ellipse Fitting Algorithm

To test how the ellipse fitting with least squares minimization method (see Section 5.3.2) performs in different conditions, a python script is prepared. In this script, a numerically created ellipse is sampled and then some Gaussian noise is added to these data. The noisy data points provides the input to the method and the result is evaluated visually and numerically.

For the test, the following steps are taken:

- An ellipse with the following parameters are created:
 - semi minor axis = 25
 - semi major axis = 100
 - ellipse center coordinate = (50,150)
 - rotation angle = 22.50 degrees

- Six data points are sampled from the ellipse.
- Gaussian noise with 5% magnitude of the minor axis is added to obtain input data.
- The obtained data is fed to the least squares fitting algorithm.
- The numerical results after fitting are:
 - semi minor axis = 25.306
 - semi major axis = 99.154
 - ellipse center coordinate = (50.229, 150.203)
 - rotation angle = 22.87 degrees

(See Figure 5.6.)

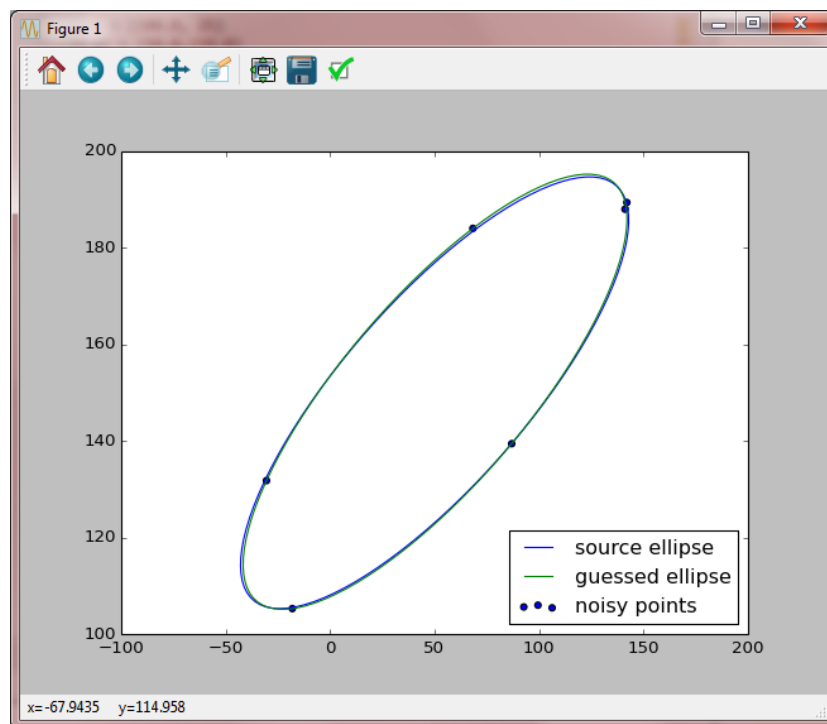


Figure 5.6. The result of the least square fitting method without constraints. The source ellipse is given in blue line, the guessed ellipse in green line and noisy data point in blue dots.

It can be seen from the numerical and visual results that the method works as expected and can be tested on actual X-Ray images. The obtained result is given in Figure 5.7.

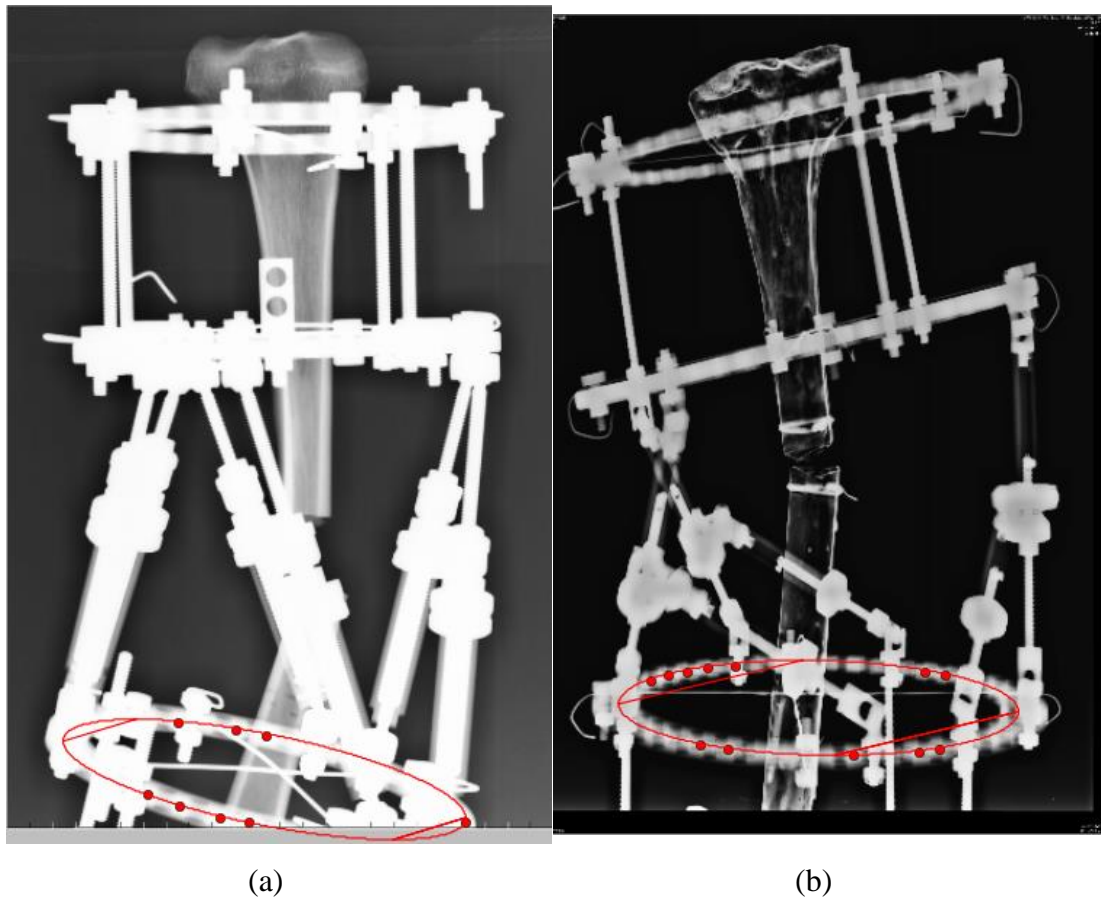


Figure 5.7. The result of the least square fitting method applied on reference points (shown in red) obtained at the image processing stage from (a) Gough-Stewart Platform External Fixator and (b) Lambda Fixator

5.4. Ellipse Fitting with Major Axis Constraints

Even if we can fit an ellipse to the available points, the obtained ellipse might not represent the distal ring perfectly. For instance, if the right most reference point is removed from the input data (Figure 5.8), the algorithms described earlier may produce an ellipse of improper size (Figure 5.9). On the other hand, standard rings with known diameters are utilized in clinical practice, such that the major axis of the ellipse on the X-ray must be equal to the diameter of the related ring. If the known semi major axis length of the ellipse (which equals the ring diameter) is used as a constraint, a better ellipse fit is possible even if the available interpolation points are not well distributed.

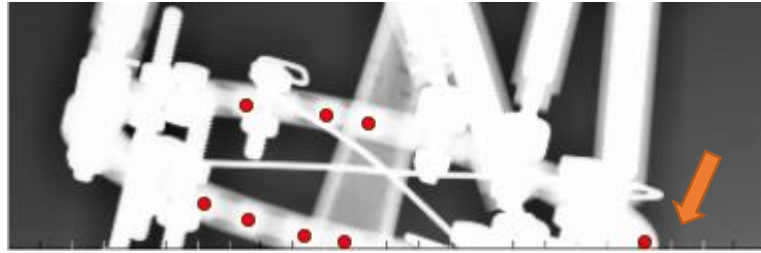


Figure 5.8. The reference point indicated with the arrow is removed.

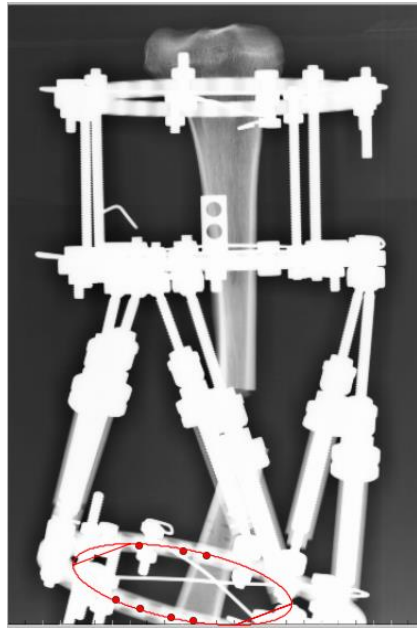


Figure 5.9. The result of the ellipse fitting without the rightmost reference points.

5.4.1. Constrained Direct Fitting

In direct fitting, the axis constraint is enforced with an approach similar to the one described in Section 5.3.1. The only difference is that the constraint matrix \mathbf{C} looks different because it imposes a different constraint. In this part, the constraint matrix will be updated for semi major axis constraint. In one study (Liu and Dong, 2010), the details of this method for semi minor axis constraint is explained. Taking this study as a reference point and using the approximate definition of the semi major axis given elsewhere (Rosin, 1999), the constraint matrix can be updated. With respect to Eq. (5.1), the semi major axis A of an ellipse can be given as:

$$A = 2 \sqrt{\frac{2f}{\left(a + c - \sqrt{b^2 + \left(\frac{a-c}{f}\right)^2}\right)}} \quad (5.12)$$

Eq.(5.12) is put into the following quadratic form whose is assigned, again, arbitrarily a value of 1 considering the scalability of the parameters (Liu and Dong, 2010):

$$\frac{(a-c)^2}{f^2} = a^2 - b^2 + c^2 + 2ac + \frac{16}{A^2}af + \frac{16}{A^2}cf + \frac{64}{A^4}f^2 = 1 \quad (5.13)$$

The constraint given in Eq.(5.13) can be again written in matrix quadratic form $\mathbf{a}^T \mathbf{C} \mathbf{a} = 1$ where the constraint matrix \mathbf{C} , introduced earlier, in this case takes the form:

$$\mathbf{C} = \begin{bmatrix} 1 & 0 & 1 & 0 & 0 & \frac{8}{A^2} \\ 0 & -1 & 0 & 0 & 0 & 0 \\ 1 & 0 & 1 & 0 & 0 & \frac{8}{A^2} \\ 0 & 0 & 0 & 0 & 0 & 0 \\ 0 & 0 & 0 & 0 & 0 & 0 \\ \frac{8}{A^2} & 0 & \frac{8}{A^2} & 0 & 0 & \frac{64}{A^4} \end{bmatrix} \quad (5.14)$$

With this constraint matrix, the method given in Section 5.4.1 can be used.

5.4.2. Constrained Fitting with Least Squares Minimization

In order to use the semi major axis (ra) as a constraint, it should be defined in terms of general ellipse equation coefficients.

For the ellipse equation given as:

$$ax^2 + bxy + cy^2 + dx + ey + f = 0 \quad (5.15)$$

M and M_0 matrices can be written as

$$M_0 = \begin{bmatrix} f & \frac{d}{2} & \frac{e}{2} \\ \frac{d}{2} & a & \frac{b}{2} \\ \frac{e}{2} & \frac{b}{2} & c \end{bmatrix} \quad M = \begin{bmatrix} a & \frac{b}{2} \\ \frac{b}{2} & c \end{bmatrix} \quad (5.16)$$

The eigenvalues of the M are calculated as

$$\lambda_1, \lambda_2 = \frac{a}{2} + \frac{c}{2} \mp \frac{1}{2} \sqrt{a^2 - 2ac + b^2 + c^2} \quad (5.17)$$

Finally, semi major (ra) and semi minor (rb) axes can be calculated as

$$ra = \sqrt{-\frac{\det(M_0)}{\det(M) \lambda_1}} \quad rb = \sqrt{-\frac{\det(M_0)}{\det(M) \lambda_2}} \quad (5.18)$$

to obtain

$$\{ra, rb\} = \sqrt{2} \sqrt{\frac{-4acf + ae^2 + b^2f - bde + cd^2}{(4ac - b^2) \left(a + c \mp \sqrt{(a-c)^2 + b^2} \right)}} \quad (5.19)$$

The obtained equation is imposed to the least square minimization as a constraint.

5.4.3. Test of the Constrained Ellipse Fitting Algorithms

The result of constrained direct ellipse fitting as applied to the X-Ray image is given in Figure 5.10. This method has not performed as well as we expected.

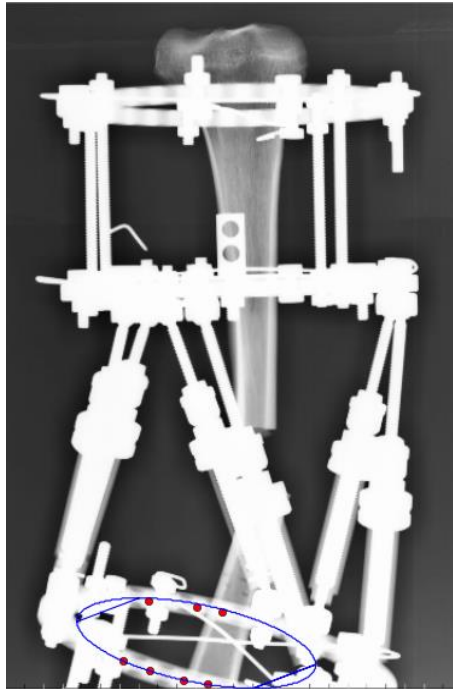


Figure 5.10. Semi major axis constrained direct ellipse fitting applied to the X-Ray image.

For the performance test of the constrained ellipse fitting with least square minimization algorithm (see Section 5.4.2), a script is prepared. With this script, a source ellipse is created with the parametric data given in Table 5.1; then Gaussian noise with magnitude equal to 5% of the minor axis is added to the points of the source ellipse. The test data is created by random sampling of the noisy data from a small portion of ellipse. Finally the constrained and unconstrained ellipse fitting algorithms are applied to this data and the parametric results of the both algorithms are given in Table 5.1 and Figure 5.11. As we see, the constraint has a big impact on the performance of the ellipse fitting.

Table 5.1. Parameters of the source ellipse and the ellipses obtained as a result of the unconstrained and constrained least square minimization fitting algorithms.

	Semi Minor	Semi Major	Center Point	Rotation
	Axis	Axis	Coordinate	Angle
Source Ellipse	5.00	40.00	(50.00,50.00)	22.50
Unconstrained	3.27	13.36	(74.54, 60.05)	22.79
Constrained	4.77	40.00	(50.14, 49.98)	22.42

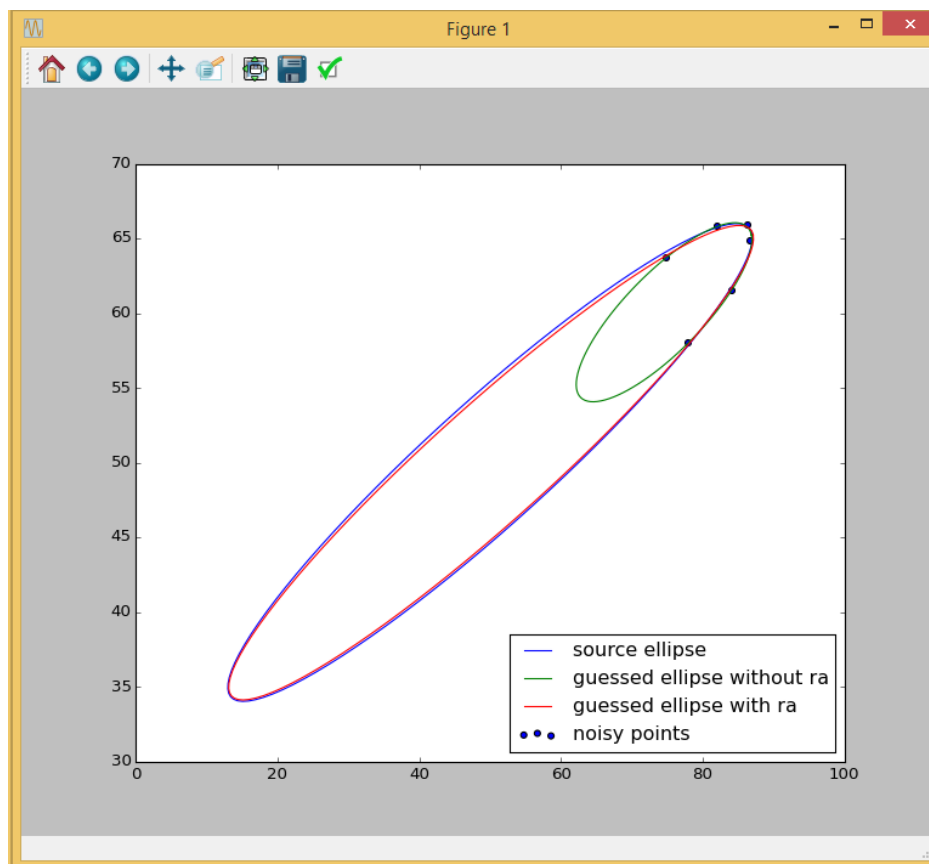


Figure 5.11. The visual result of the least square fitting method. The blue ellipse is the source ellipse used to create data points. The green ellipse is obtained without ra constraints, and the red ellipse is obtained with ra constraints.

The method is also applied to the X-Ray image data and the result is shown in Figure 5.12.

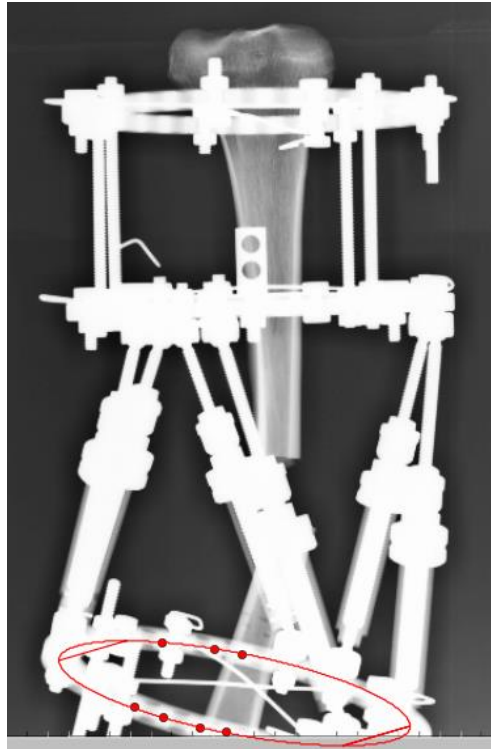


Figure 5.12. The result of the least square fitting method with semi major axis constraint.

5.5. Manuel Fitting: Moving Ellipse

In order to apply the automatic ellipse fitting method, at least five interpolation points are needed on the image. In some cases, the number of available points for interpolation might be less than the required minimum of five. Hence, the functionality where the user can fit an ellipse manually on the distal ring has been also implemented to the GUI. The user can also scale, rotate and translate the ellipse with the mouse (Figure 5.13).

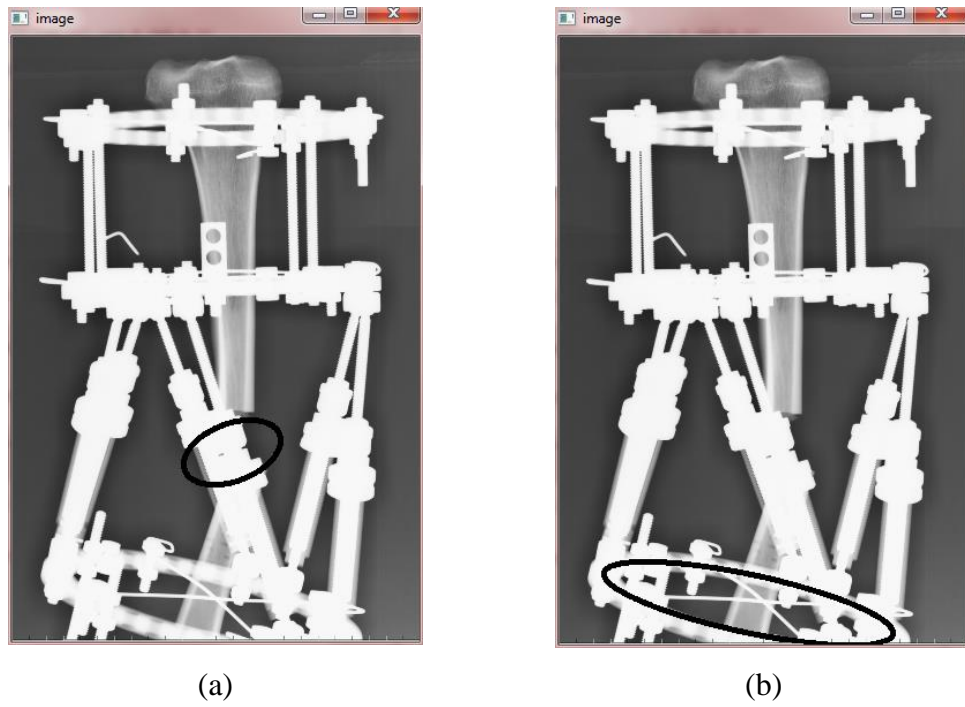


Figure 5.13. Ellipse created on the image (a) and its position after manual fitting (b).

6. INTEGRATED GRAPHICAL USER INTERFACE

As a part of this doctoral research, a new external fixator system is designed and the underlying mathematical theory has been developed. With this new design, the clinician has the flexibility of connecting the lambda fixator modules between proximal and distal ring without any constraint. However, fewer constraints lead to a more complex mathematical theory. To hide this mathematical theory and allow the clinician to interact easily with the fixator system and prescribe a treatment, an accompanying GUI has been developed (Figure 6.1). With the GUI, parametric data is collected from *AP* and *L* X-ray images either automatically, semi-automatically or manually as described in earlier chapters. The developed GUI and its functionalities are described in this chapter.

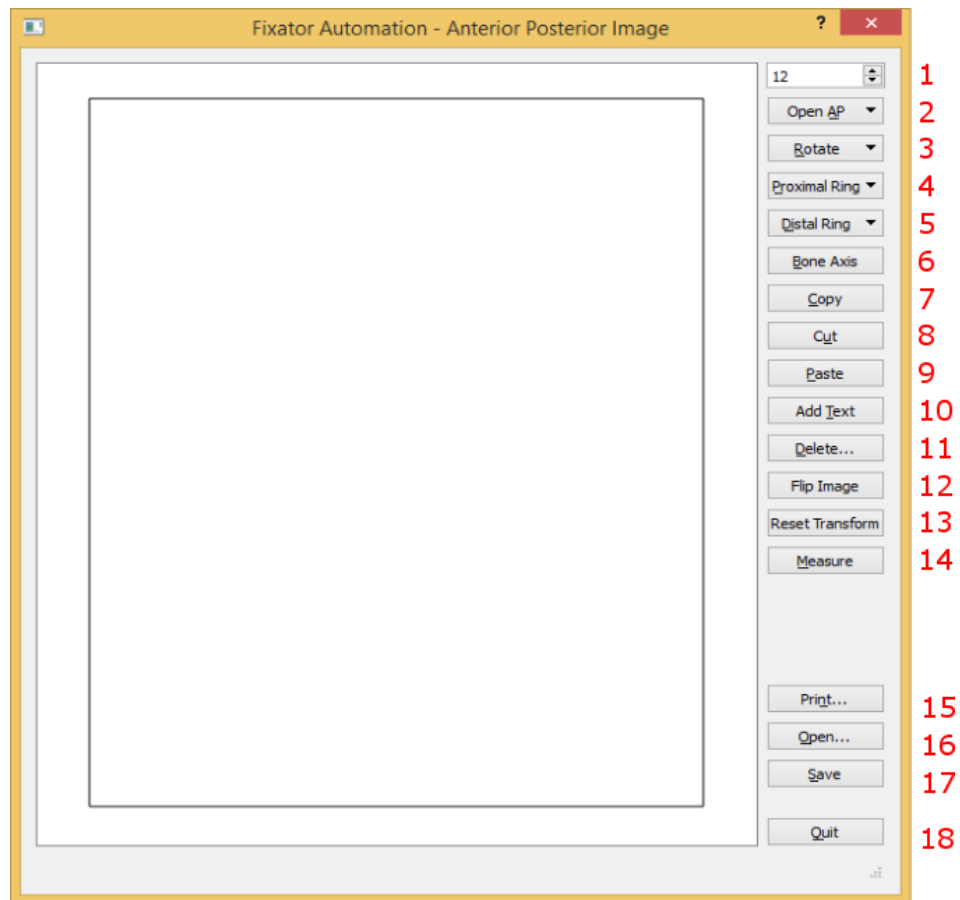


Figure 6.1. The GUI with its items numbered

6.1. Preparation for Measurement

The preparation for measurement involve basically opening the images files and rotating/flipping them:

- **Opening:**

Digital X-Ray images are imported to the GUI for measurement. The default output format of the current X-Ray devices is DICOM, but the GUI can import images in JPG or DICOM format. With this functionality, the image can be easily imported to the GUI by the clinician. Opening the image file is done by pressing the “Open AP” or “Open L” buttons for *AP* and *L* images, respectively (Figure 6.1, item 2).

- **Rotate:**

Using the “Rotate” pull-down menu of the GUI, the input images can be rotated about the image center (Figure 6.1 (3)). There are options for 90, -90, 180, 1 (fine rotation) and 20 (coarse rotation) degrees rotations (Figure 6.2).

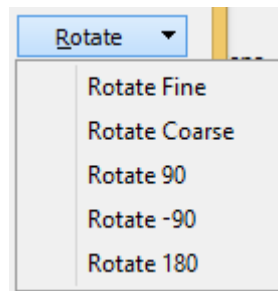


Figure 6.2. Rotate menu

- **Flip Image:**

Sometimes the input image can be flipped with respect to the vertical. In such cases, the image must be flipped back to its correct orientation before starting with the measurements. This is done using the “Flip Image” button of the GUI (Figure 6.1, item 12)).

6.2. Measurement Procedure

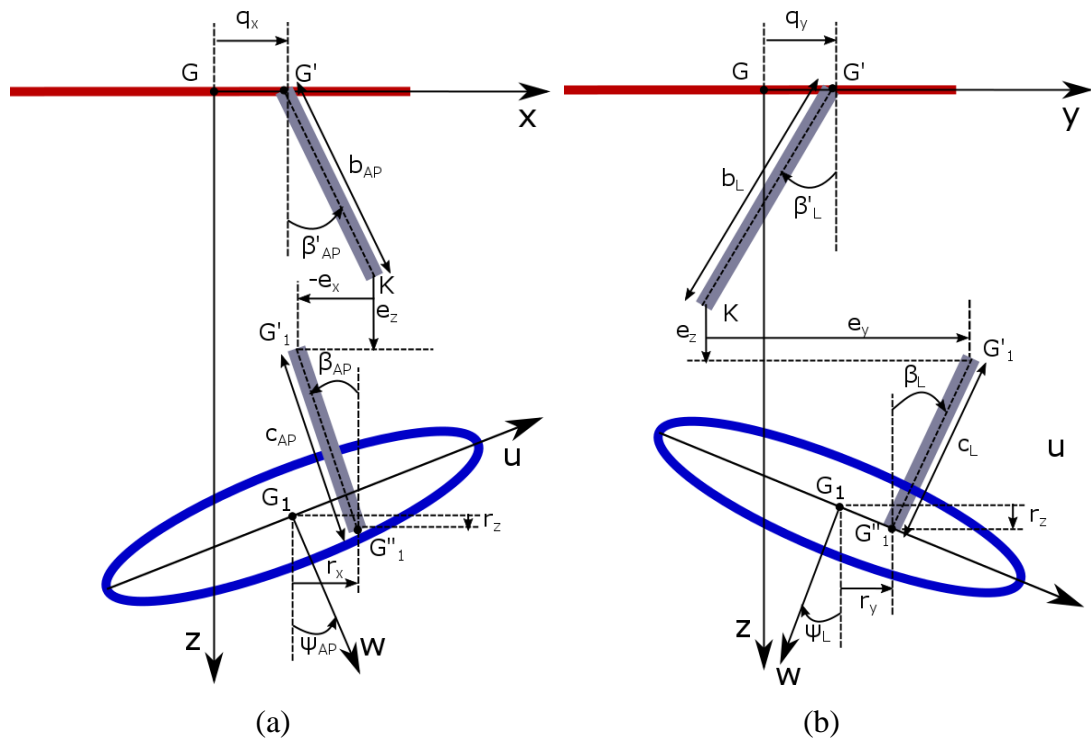


Figure 6.3. Parameters measured from (a) Anterior – Posterior and (b) Lateral X-ray images

The parameters which will be collected semi-automatically with the developed GUI are β'_{AP} , β_{AP} , q_x , e_x , e_z , r_x , r_z , b_{AP} , c_{AP} and Ψ_{AP} (Figure 6.3, (a)) for the AP view and β'_L , β_L , q_y , e_y , e_z , r_y , r_z , b_L , c_L and Ψ_L (Figure 6.3, (b)) for L view. All these parameters are measured with respect to ring axes and bone fragment which need to be defined by the clinician on the images using the GUI functionalities.

- **Proximal Ring:**

The origin of the global coordinate system used for all the measurements is located at the center of the proximal ring. If the X-Ray image is taken as it is described in the theory, the proximal ring will be seen as a line. To locate the proximal ring on the image, the “Proximal Ring” button is pressed (Figure 6.1, item 4) and then two opposite corners are selected (Figure 6.4).

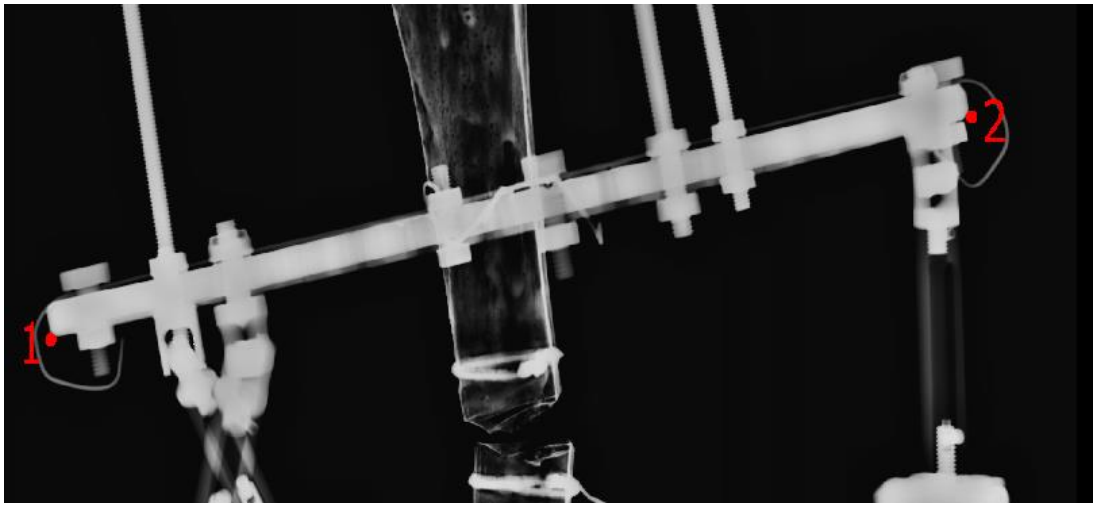


Figure 6.4. Proximal ring axis point selection

All length measurements on the X-Ray images are obtained as pixel values while the real system values are in millimeters (mm). By selecting the two corner points, we do not just define the ring location but we also indirectly determine a conversion factor between pixel and mm units, since the defined distance, in terms of pixels, is equal to the ring diameter which is a known system parameter. Hence, from the ring diameter it is possible to find the metric equivalent of one pixel.

In reality, rather than directly to the rings, the struts connect to mechanical elements attached to the rings in Taylor-like ring fixators. As a result, the plane of connection points is parallel to the ring plane but slightly shifted by a known amount. This *virtual ring plane* is the one that bears significance with respect to the mathematical model and its distance to the actual ring is input in the GUI (Figure 6.1, item 1). After the proximal ring is located on the image, the virtual ring plane is

automatically drawn on the image. Its center point, which represent the origin of the global coordinate system, is located and the z-axis of the global system is drawn (Figure 6.5)

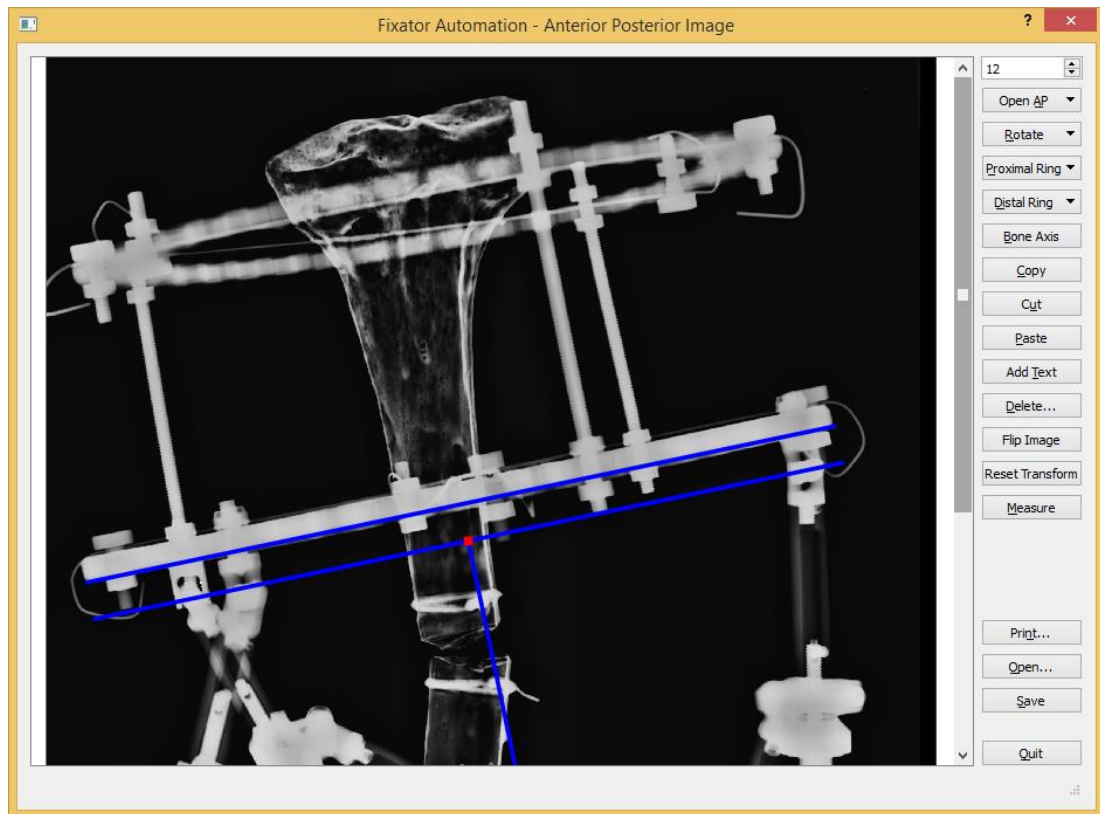


Figure 6.5. Virtual and actual proximal ring axes and z –axis.

The GUI allows manual intervention to the drawn axes and lines if the clinician is not satisfied with the outcome.

- **Distal Ring:**

Another reference coordinate system, designated as (uvw) system in the earlier chapters and located at the center of the distal ring, is also required for measurement purposes. Distal ring is usually seen as an ellipse in the X-Ray images. As described in Chapter 5, the ellipse can be fitted automatically or manually.

Distal ring drawing procedure is started by pressing “Distal Ring” button of the GUI (Figure 6.1, item 5). In the manual fitting, the four vertices of the ellipse are located by the user and the semi-major and semi-minor axes are automatically calculated. The virtual ring plane passing through the connection points (as we have described earlier in connection with the proximal ring) lies a known distance from the actual ring. The major axis of the virtual ring is automatically drawn parallel to the major axis of the actual ring. This time, the distance between the two ring planes is a projected distance and slightly smaller than its actual value. The projected distance can be easily computed from the major axis/minor axis length ratio of the ellipse in the image. The origin of the uvw –coordinate system is located at the center of the virtual ring axis (Figure 6.6). Again, if the clinician is not satisfied with the obtained ellipse and/or the ring axes, the GUI allows them to be changed manually.

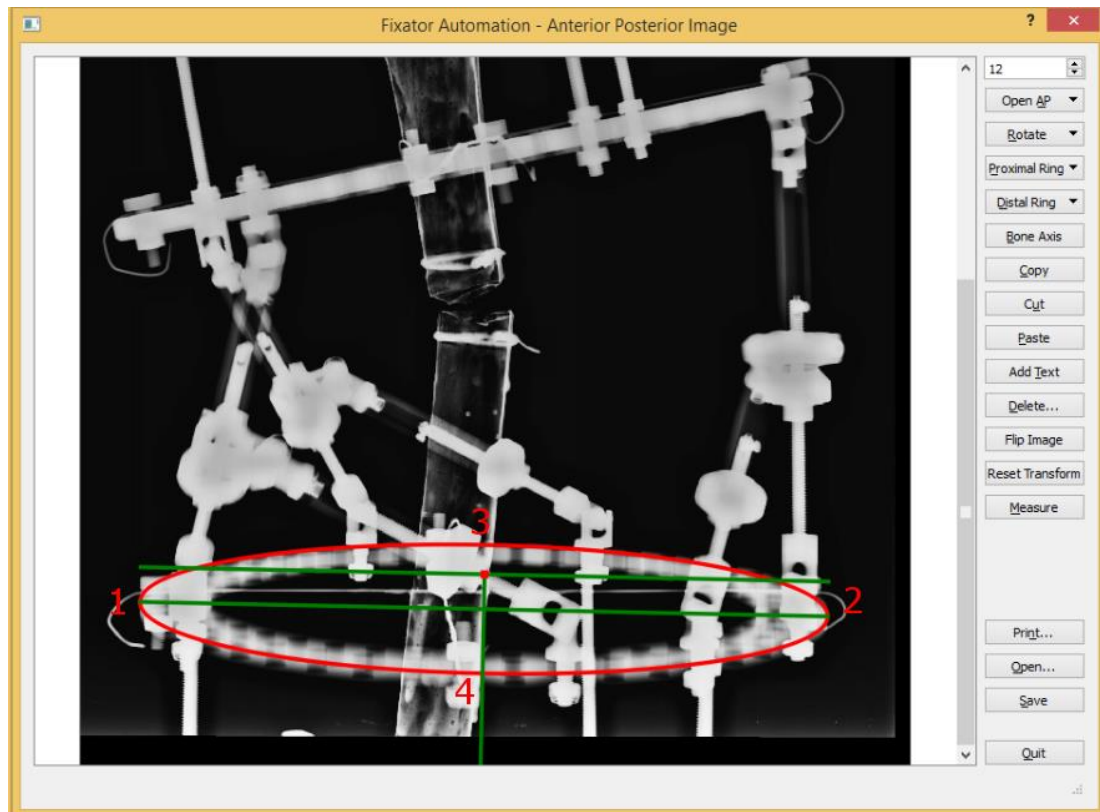


Figure 6.6. Distal Ring: selected points (1, 2, 3, 4) and obtained ellipse with w –axis of the uvw –coordinate system.

- **Bone Axis:**

The main purpose of the treatment is to align the axes of bone fragments to their anatomical position. For deformed bones, these axes may be difficult to locate automatically. Hence, the fragment axes are located manually by the clinician using the GUI.

The procedure is started by pressing the “Bone Axis” button of the GUI (Figure 6.1, item 6). The clinician selects one point on the approximate bone axis and another at the end of the bone fragment, and both points are automatically connected with a line (Figure 6.7). The drawn line represents the bone axis and can be moved for a finer tuned axis.

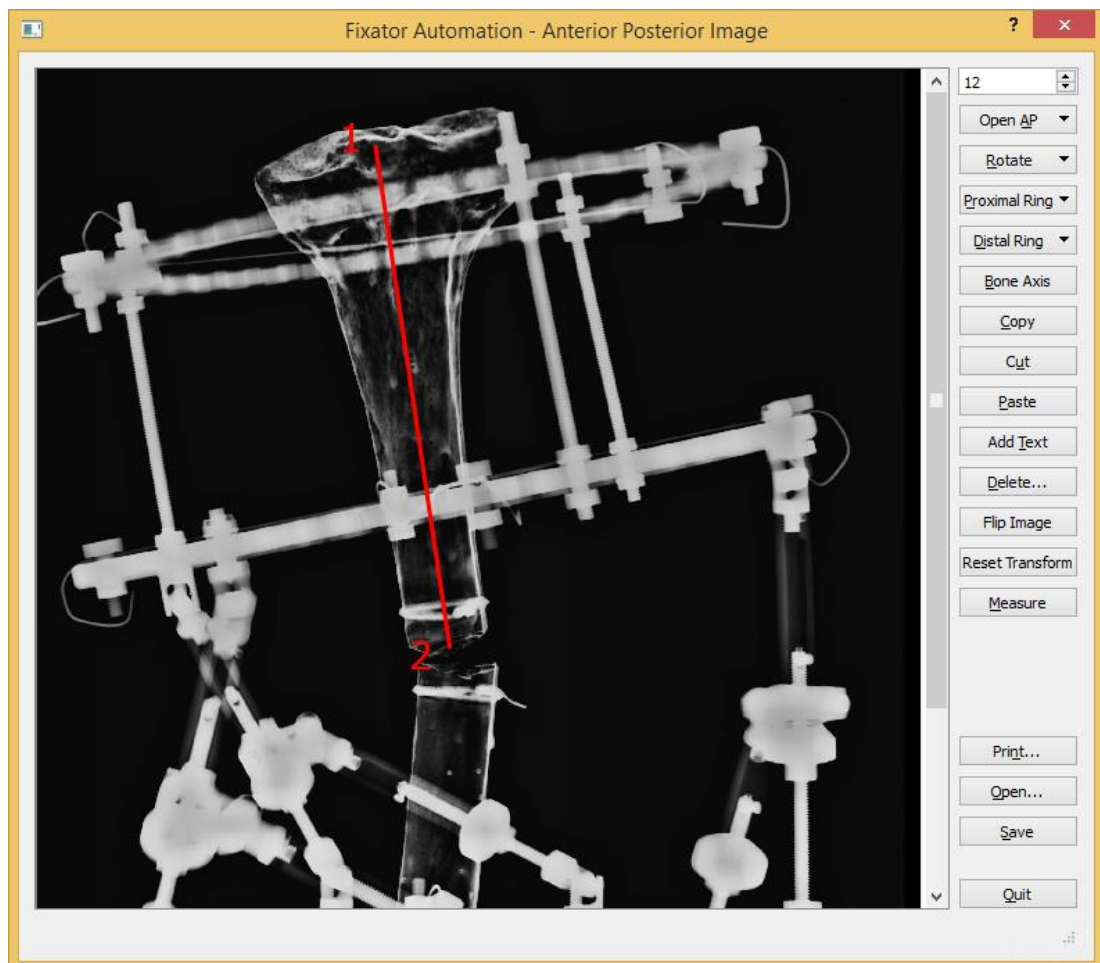


Figure 6.7. Bone Axis: Selected points (1, 2) and the resulting bone fragment axis

- **Measurement:**

After the rings and axes are located (Figure 6.8), the measured parameters are transferred to the calculation window of the GUI by pressing the “Measure” button.

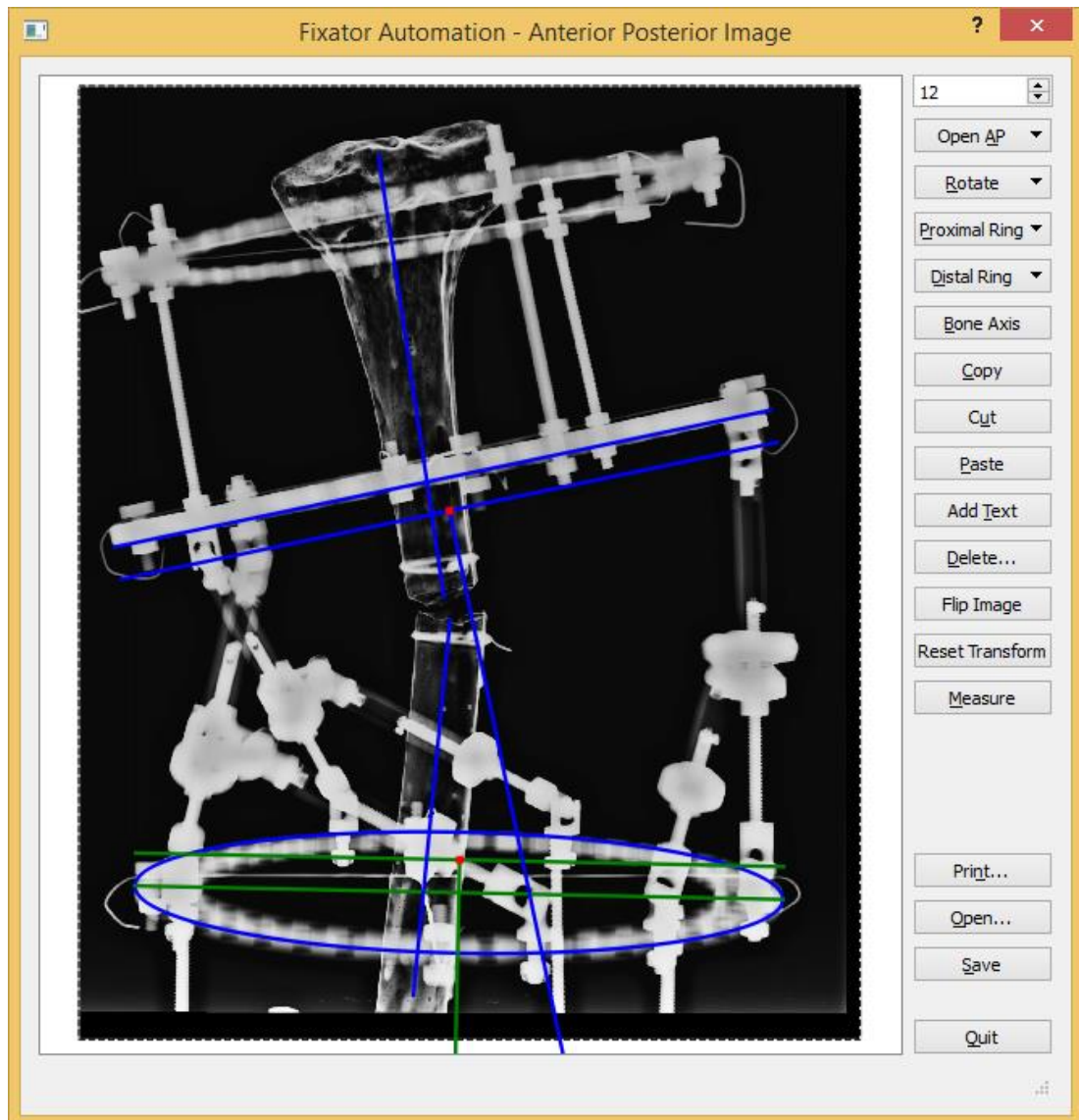


Figure 6.8. Measurement screen.

6.3. Helper Functions and Tools

The measurement GUI has some helper functions and tools that can be used during measurements. “Copy”, “Cut”, “Paste” and “Delete” buttons can be used to manipulate the graphical elements that are put on the images as described earlier (Figure 6.1, items 7, 8, 9 and 11).

Text can be added to the image for labeling and explanations using text adding functionality of the GUI. After pressing the “Add Text” button, the text can be formatted in a pop-up window before being added to the text (Figure 6.9).

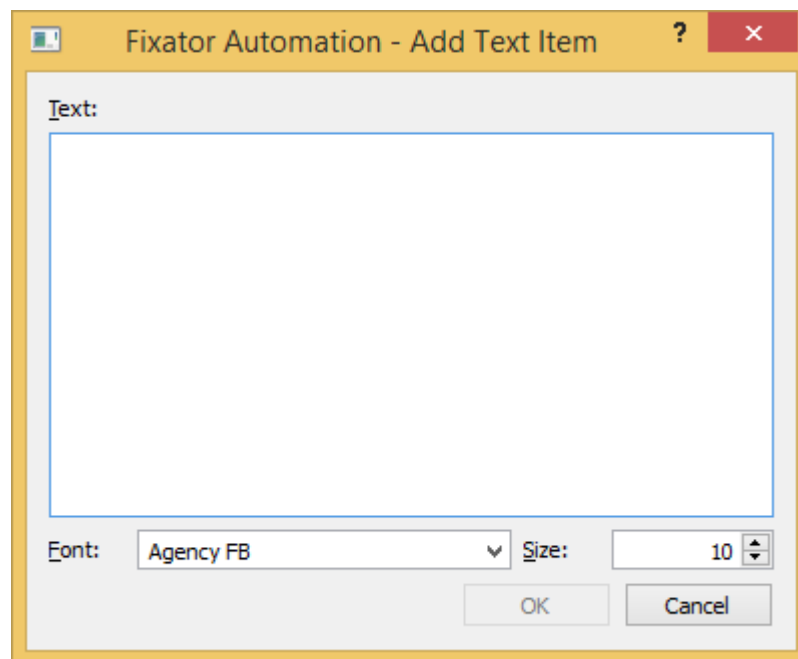


Figure 6.9. Dialog window to add text.

“Reset Transform” button is used to reset the rotation imposed on an object and return it to its original position (Figure 6.1, item 13).

The “Print” button allows the user to print the X-ray image with measurement drawings on it (Figure 6.1, item 15).

The “Save” and “Open” buttons (Figure 6.1, items 16-17) are used to save and load all the measurement elements to/from a file. With this functionality, it is possible to open a previously saved measurement and manipulate all its elements and, if

necessary, repeat the measurement operation. For this purpose, a special formatting standard has been defined in an effort to efficiently save and load files.

Finally, the “Quit” button is used to close the measurement GUI (Figure 6.1, item 18).

6.4. Complete System Test – 1

The whole treatment procedure consists of five main steps: Preparation of the Fixator System, Preparation of the X-ray Images, Measurement of X-ray Parameters, Obtaining Clinical Data and Evaluation of the Results. A treatment scenario is prepared to test all these steps.

6.4.1. Preparation of the Fixator System

The test of the system and developed GUI is performed on a lambda fixator system to which artificial tibia bone fragments are mounted. The lambda fixator has three lambda modules (Figure 6.10). Note that there are two rings each at the distal and proximal side of the fracture site. The ones connected to the lambda modules (and closer to the fracture site) are those we have referred to as proximal and distal rings so far. The frame initially is set to a position where the bone fragments are far from their anatomically aligned orientation.



Figure 6.10. Lambda fixator with an artificial bone

6.4.2. Preparation of the X-ray images

The main input of the system is two perpendicular X-ray images taken in the *AP* and *L* direction. The X-ray images of the prepared fixator frame have been taken at the Radiology Department of Çukurova University to provide the input images (Figure 6.11).

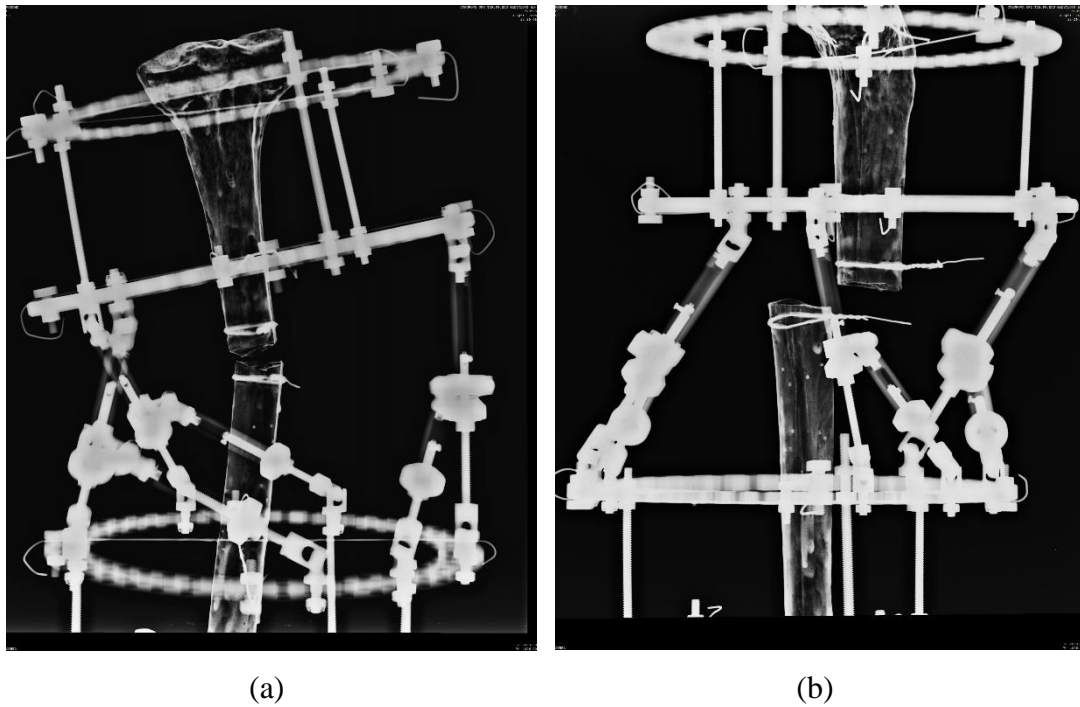
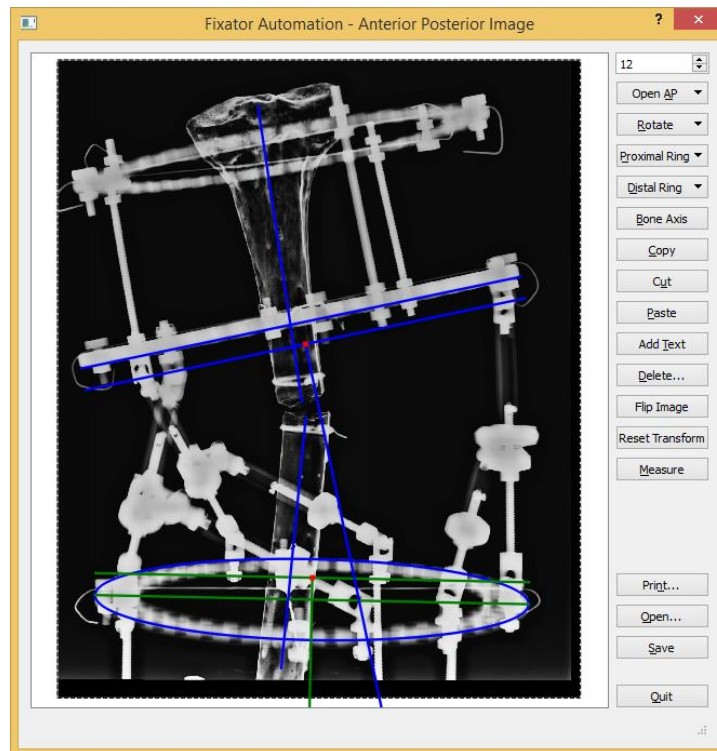
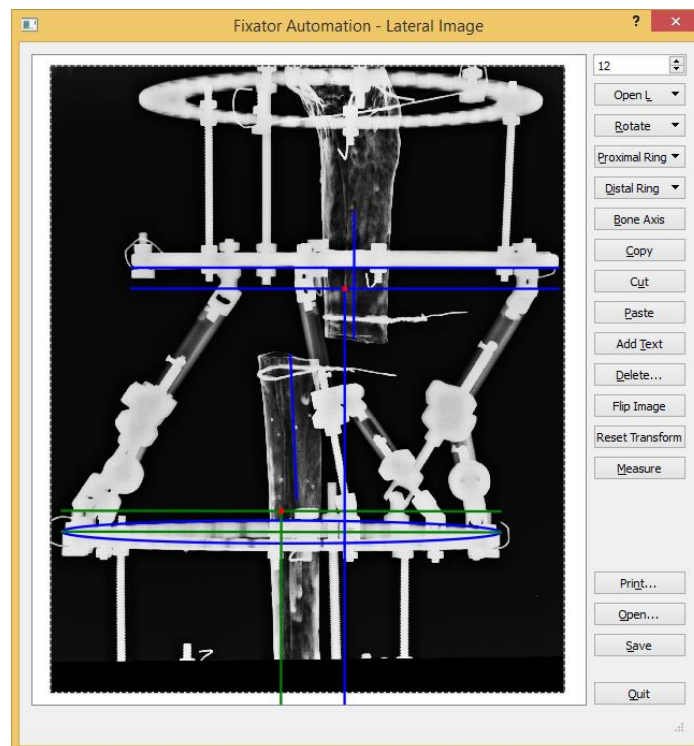


Figure 6.11. X-ray images of the fixator system from (a) *AP* and (b) *L* views.

6.4.3. Measurement of X-ray Parameters

The input images are in DICOM format. Therefore, they are loaded to the GUI using the “Open Dicom” button. Sometimes, DICOM files contains a data tag named “Pixel Spacing” which, if specified, can be used for metric conversion of pixel size. In our case, this value is not specified and the conversion factor is calculated automatically from the known diameter of the proximal ring (see Section 6.2).

The measurements have been done as described in Section 6.2 for *AP* (Figure 6.12) and *L* (Figure 6.13) images. The results are transferred to the calculation window.

Figure 6.12. Measurement GUI with measured *AP* X-ray imageFigure 6.13. Measurement GUI with measured *L* X-ray image

6.4.4. Obtaining the Clinical Data

The clinical data, especially the rotation between bone fragments and fixator rings, needs to be defined by the orthopedist. For experimental purposes, these two parameters are measured from axial digital image of the system, (Figure 6.14). The rest of the clinical data are the proximal and distal ring radii; and the lambda module connection configuration parameters are given in Table 6.1 to 6.3 for the three modules.

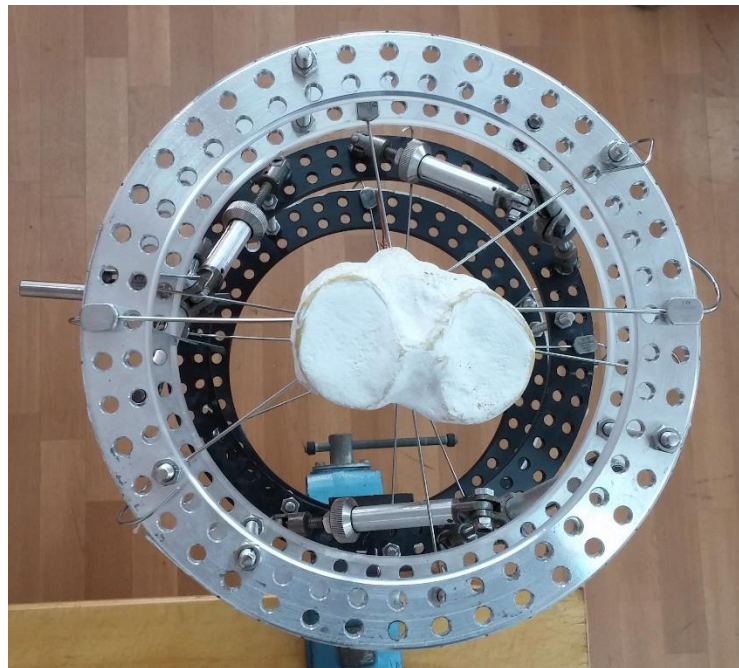
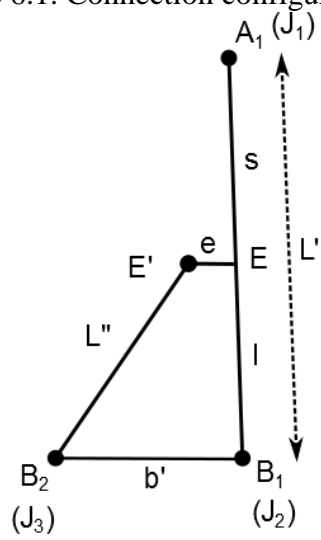


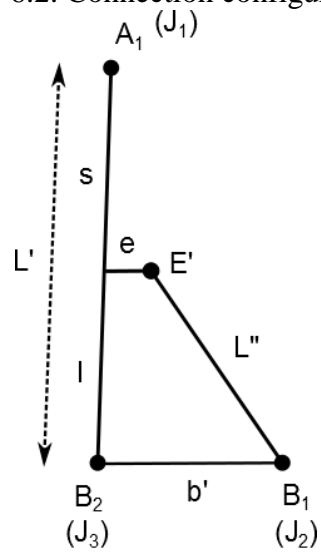
Figure 6.14. Axial image of the system.

Table 6.1. Connection configuration for module 1



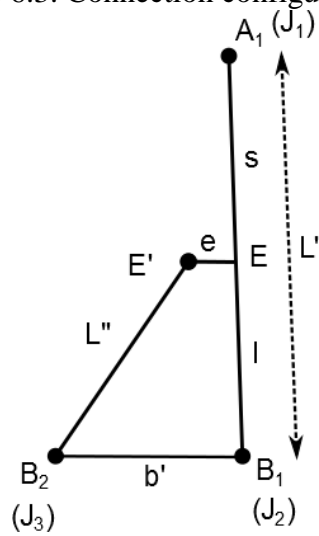
J_1 : 346 Degrees
 J_2 : 26 Degrees
 J_3 : 58 Degrees
 s : 75 mm
 e : 15 mm
Case: 2

Table 6.2. Connection configuration for module 2



J_1 : 122 Degrees
 J_2 : 82 Degrees
 J_3 : 154 Degrees
 s : 75 mm
 e : 15 mm
Case: 1

Table 6.3. Connection configuration for module 3

 J_1 : 210 Degrees J_2 : 250 Degrees J_3 : 298 Degrees s : 75 mm e : 15 mm

Case: 2

6.4.5. Calculating the System Configuration and Test of the GUI Results

The data obtained from X-ray images is transferred to the GUI. Then, the clinical data is entered by the orthopedist. At this point, all the data required for the calculation is input to the calculation GUI (Figure 6.15). The system configuration for initial and final states of the system is calculated based on the theory given in Section 3.2. The initial configuration can be easily checked on the system. The strut lengths are changed to their final values as obtained from the GUI (Figure 6.16). The bone fragments are visually confirmed to be anatomically aligned. The opinion of a professional orthopedist is also sought in order to ensure the clinical validity of the results.

Lamda Fixator

File Show A Matrices

AP Data

Ψ_{AP} -12.4377399231

β_{AP} -17.2426776602

β'_{AP} -2.21405683139

C_{AP} 89.4949298176

b_{AP} 31.1878714344

L Data

Ψ_L 0.0620273423506

β_L -2.58148021097

β'_L 0.325869163855

C_L 89.3663144077

b_L 28.725452244

Theta Values

	θ_x	θ_y	θ_z
Proxi Bone	0.325625	-2.214056	0.0
Distal Bone	1.713521	-17.33085	-14.0
Distal Ring	1.542841	-12.34332	-6.9

e Data

e_x -0.03655 e_y -36.2978 e_z 9.758382

r Data

r_x -10.71934 r_y 9.234593 r_z 0.0099972

q Data

q_x -4.48730 q_y 5.275294 q_z 0

Rotation Parameters

δ_{Ax} -14 δ_0 -6.9 δ 0

Lamda Constants

Modul	s	e	J1	J2	J3	
Modul 1	75	15	346	26	58	Case 2
Modul 2	75	15	122	82	154	Case 1
Modul 3	75	15	210	250	298	Case 2

Ring Parameters

Proximal Ring 115.5 Distal Ring 115.5

Control Parameters

r_u -11.4773525496 r_v 7.94496256738

GG1_0 -22.62338 -36.39550 127.74899

GG1_n 3.0993796 -1.9434112 121.37190

Fragment Lengths

c 93.5632863123 b 28.7469120303

Result Box

	Initial	Final
L1'	156.712361293	148.046180834
L1''	102.408999716	112.367361589
L2'	140.577569949	149.259497524
L2''	110.242386248	102.330061682
L3'	144.784216586	152.846186077
L3''	127.649881113	134.754211887

Choose Problem No Calc for AP

CALC

Figure 6.15. Calculation GUI with input data entered and the results are calculated.



Figure 6.16. System configuration after the strut lengths are set to their final values as obtained from the GUI.

6.5. Complete System Test – 2

A second test with a different initial configuration is applied to the system (Figure 6.17). The prepared X-ray images are loaded to the GUI and the measurement is done as described in Section 6.2 (Figure 6.18 and Figure 6.19). The clinical data is obtained from the axial image (Figure 6.20). The final system configuration is calculated (Figure 6.21) and the obtained strut lengths are imposed. The proper alignment of the fragments are once again achieved (Figure 6.22).

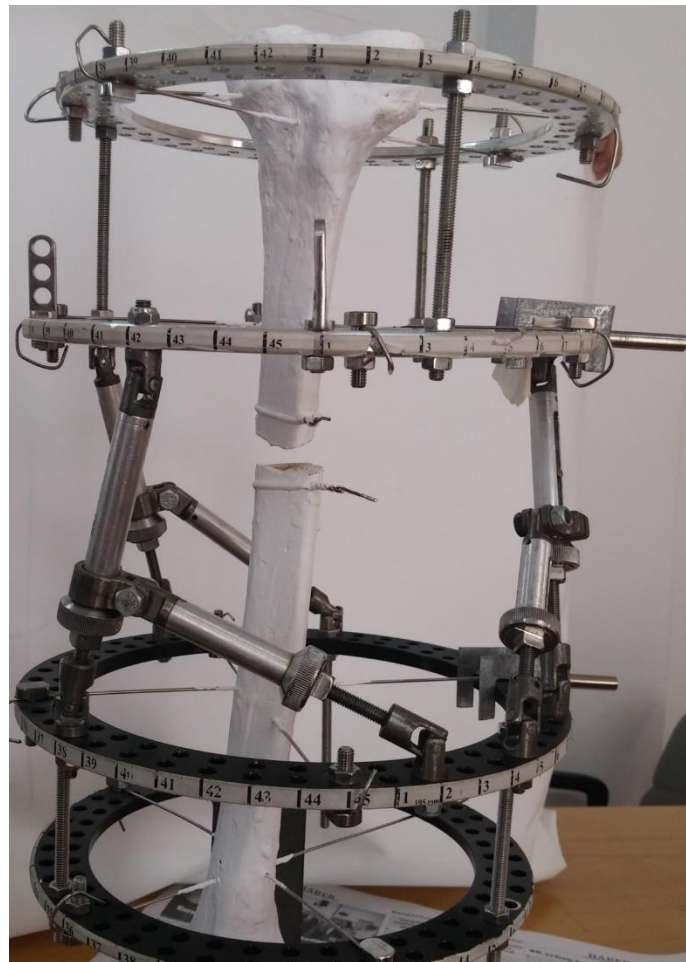


Figure 6.17 Initial configuration of the system for Test -2.

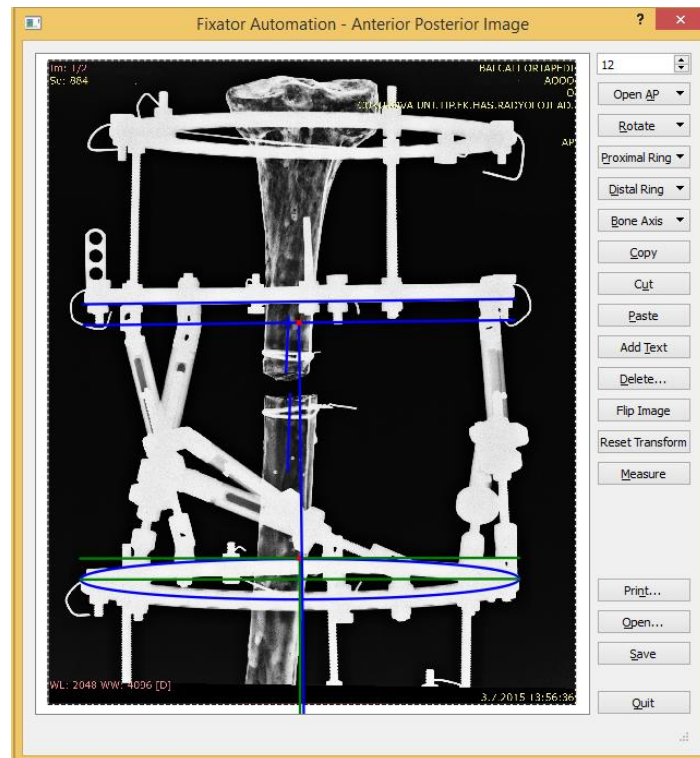


Figure 6.18 Measured AP image of Test -2

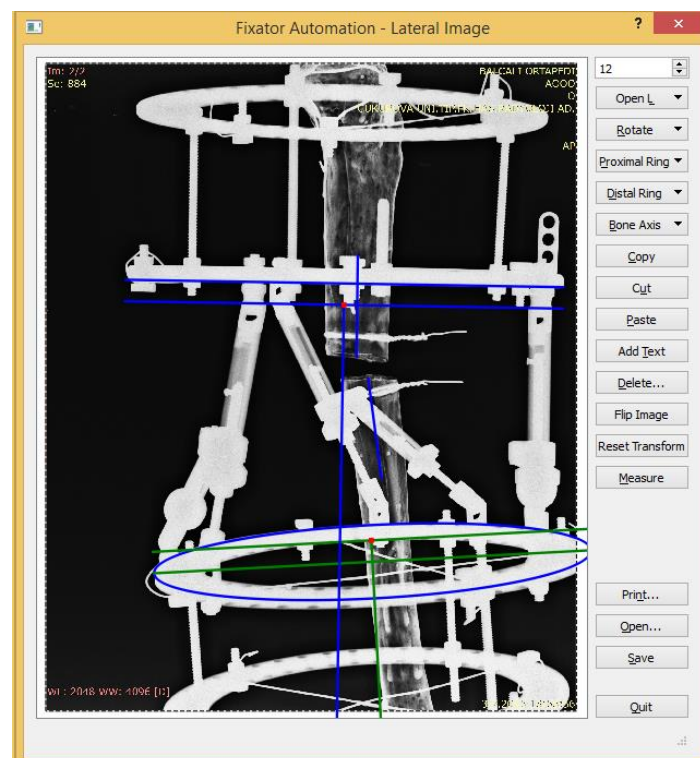


Figure 6.19 Measured L image of Test -2

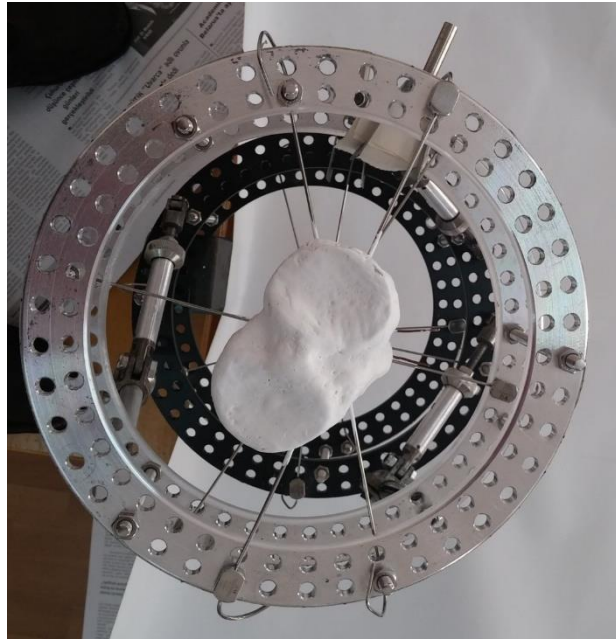


Figure 6.20 Axial image of the system for Test -2

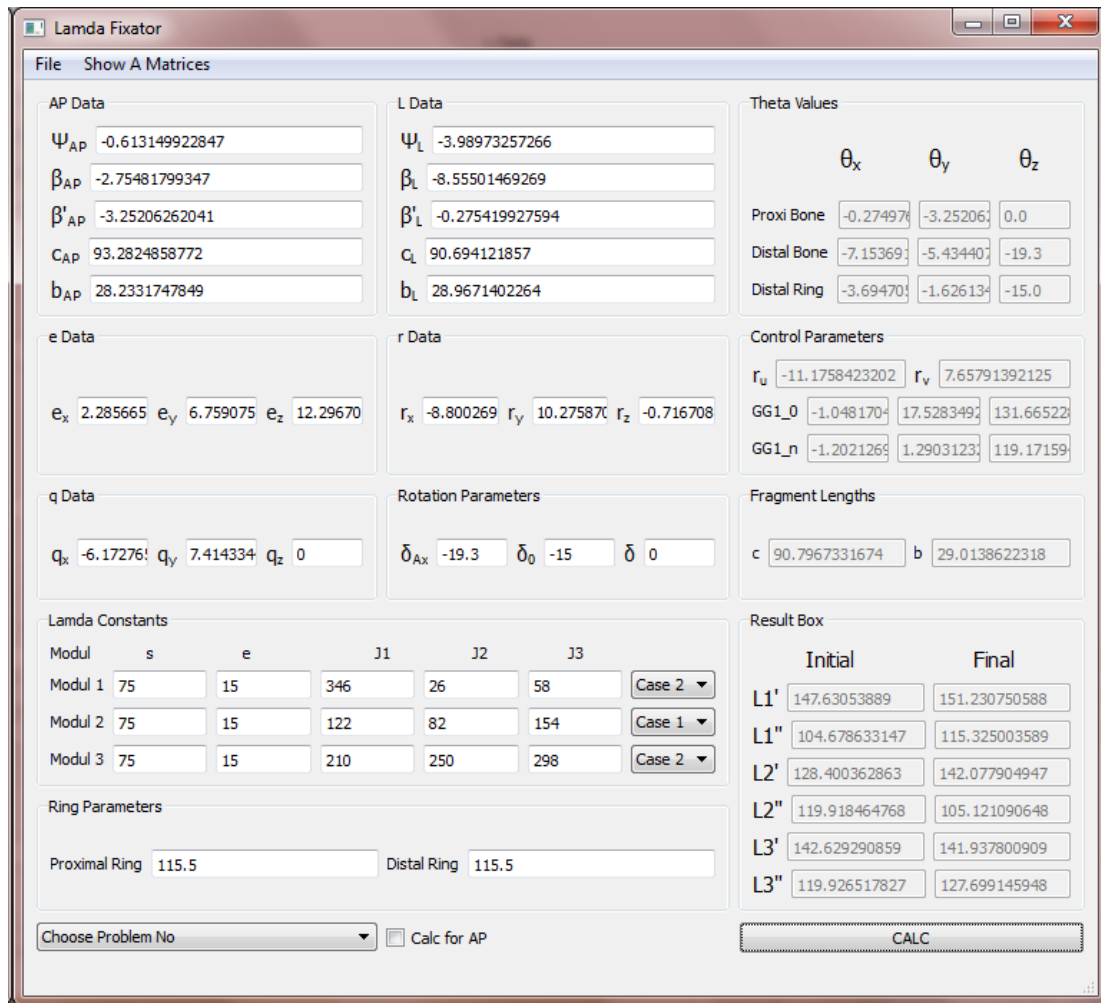


Figure 6.21 The measurement data and the calculation results for Test -2.

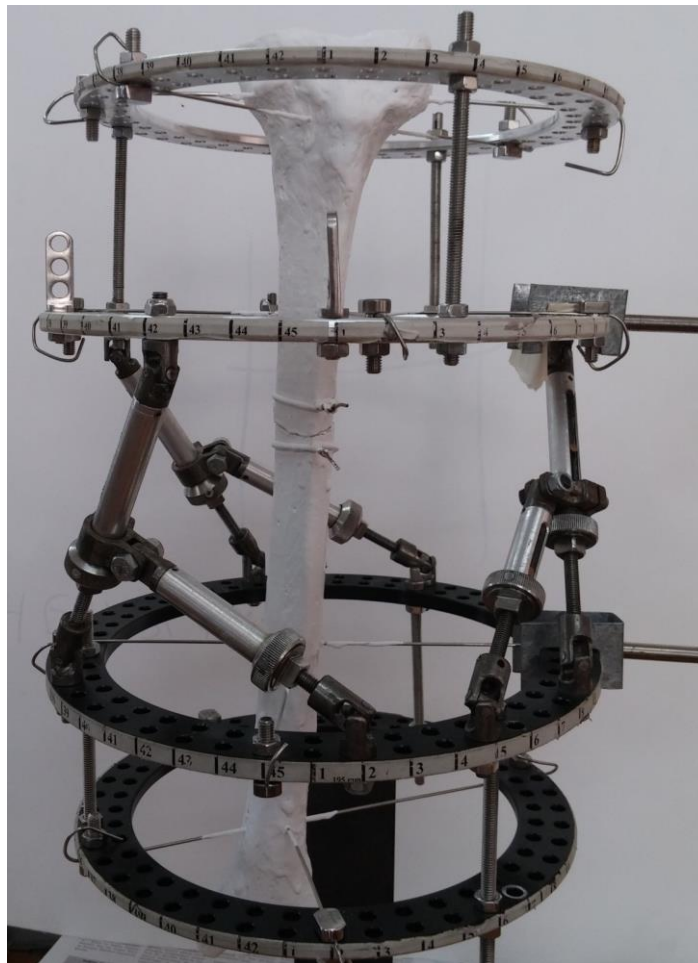


Figure 6.22 Result of the Test – 2: the aligned position of the system

7. CONCLUSION

7.1. Concluding Remarks and Discussion

In this doctoral research, we have developed a computer-assisted external fixation system with its several aspects. The work has included the design of two different external fixators, development of the inverse kinematics that can be applied to both fixator designs, a mathematical approach that can be used in case of oblique X-ray view and the development of a GUI that automatizes the measurement of several parameters.

External fixation systems come usually with some constraints regarding its physical installment and the way some associated measurements are performed using its GUI. These constraints, that simplify the mathematical model, however, may not be easy to impose in practice. The mathematical theory presented here provides a lot of flexibility with respect to the installment of the fixator. The developed mathematical tools handle the cases where the proximal bone fragment is not perpendicular to the ring plane, or the proximal ring does not appear as a straight line on the X-ray image.

The developed GUI allows the automatic measurement of several important parameters including the bone fragment lengths and the oblique view angle. In this work, we have always tried to develop a mathematical approach whenever the related parameter is suitable for automatic measurement. In many cases, we have tried multiple ways to achieve an objective. The ones that show promise are reported in this work, while others that show little or no success are omitted.

The GUI not only implements the mathematical theory behind automatized fixation procedure but also hides the mathematical theory from the clinician who has most likely limited mathematical background. It is important that the GUI is user-friendly such that it can be easily used by the clinician. We have tried to design the GUI with this understanding.

The lambda fixator described in this work has some advantages over the hexapod-type fixators. The inverse kinematics developed for the hexapod fixator could be easily adopted to the lambda fixator and the fixator itself is singularity-free. We

believe that the lambda fixator can find more frequent clinical applications in the future. In fact, a system that is made commercial relatively recently in Russia (Solomin et al., 2015) uses a design similar to the lambda fixator.

There are different types of deformities where a ring fixator is used for treatment. The X-ray images of these deformities are taken with different X-ray machines with varying exposure levels. It has been pointed out that the fixator itself can block the bone view in the X-ray images. Significant effort has been given to make the algorithms, developed in this work for automatized measurement, as robust as possible. Yet, there may be extreme images in the sense that one or more of the developed algorithms may fail. We believe that, while it may be possible to increase the success rate with further research, a computer-assisted automatized fixation system cannot work with 100% effectiveness. Therefore, we have also integrated manual measurement tools to the developed GUI to be used when necessary.

During the automatized fixation procedure, we measure many parameters. Since each measurement has a potential error associated with it, it is safe to say that the automatized process has several error sources. There are also other potential errors that do not originate from the measurement process. For example, the values of the relative axial rotation between bone fragments and fixator rings (δ_{Ax}, δ_0) are entered by the clinician to the GUI rather than being measured on the X-ray images and their accuracy depends on his/her level of expertise. Similarly, the *AP* and *L* images may deviate slightly from being perpendicular to each other depending on how appropriately these X-ray images are taken by the X-ray technician. An independent sensitivity analysis (Sahlar, 2010) performed has revealed that the outcome (i.e. the final strut lengths) are most sensitive to c_L, b_L, c_{AP}, b_{AP} parameters. Therefore, it is especially important to measure these parameters with minimal error.

7.2. Future Research

Various aspects of the research accomplished in this work can be furthered in the future or provide inspiration for other studies.

The kinematic theory utilized assumes the *AP* and *L* images to be perpendicular to each other which may be sometimes difficult to fulfill clinically. To overcome this problem, a simple support frame can be designed in an independent project that ensures that the images are taken perpendicular to each other. Another possible future study to overcome the same problem is to extend the kinematic theory such that this constraint is relaxed. If it is also equipped with the ability to handle non-perpendicular views, the resulting theory will be very general and cover a wide variety of situations.

As mentioned earlier, relative axial rotation between bone fragments and fixator rings (δ_{Ax}, δ_0) is guessed by the clinician. It will be useful to develop a theory where this quantities are also derived from the available X-ray images or possibly by taking extra images.

We have utilized various image processing algorithms when processing the X-ray images and we have tried different methods to achieve specific objectives. Since image processing is a vast research area, it may be possible to find or even develop algorithms that will be more effective. For example, the effective segmentation of the bone from the fixator is a topic that can be further researched at different levels.

The developed software currently produces a prescription for the treatment by processing X-ray images. With some modification, it can be also utilized as a treatment planning tool where the clinician can visualize and evaluate different treatments scenarios. This requires first and foremost a visualization tool to be implemented within the GUI.

REFERENCES

- AGLIETTI, P. and BUZZI, R., 2002. Correction of combined deformity. Surgical Techniques in Total Knee Arthroplasty, Springer: 216-223.
- AKCALI, I. D., SAHLAR, M. O., UN, K., AYDIN, A., IBRIKCI, T., ESEN, R., GULSEN, M. and BAYRAM, H., 2010. A Mathematical Model in the Implementation of a Stewart-Gough Platform as an External Fixator. World Congress on Medical Physics and Biomedical Engineering, Vol 25, Pt 4: Image Processing, Biosignal Processing, Modelling and Simulation, Biomechanics. O. Dossel and W. C. Schlegel. **25**: 708-711.
- AKÇALI, İ. D., ŞAHLAR, M. O., AYDIN, A., İBRIKÇI, T., ÜN, M. K., ESEN, R., GÜLŞEN, M. and BAYRAM, H., 2009. Alignment of Bone Fragments Through the Deployment of A Stewart Platform Mechanism. 2. Ulusal Yapay Organ ve Destek Sistemleri Kongresi. Antalya, TURKEY.
- AKÇALI, İ. D., ŞAHLAR, M. O., AYDIN, A., İBRIKÇI, T., ÜN, M. K., ESEN, R., GÜLŞEN, M. and BAYRAM, H., 2009. Ortopedik Klinik Uygulamalar İçin Bir Fiksatorün Tasarımı İmalatı ve Kullanılışı. III. Ulusal Tıbbi Cihazlar İmalatı Sanayi Kongre ve Sergisi. Samsun, TURKEY.
- AUSTIN, E., SCHNEIDER, J. and MULLANEY, M., 2004. Orthopaedic fixation method and device with delivery and presentation features, Google Patents.
- AYDIN, A., 2009. Applications of Medical Image Processing Techniques on a Biomechanics System. MSc, Çukurova University.
- BEHRENS, F., 1982. Unilateral external fixation for severe lower extremity lesions: experience with the ASIF (AO) tubular frame. Concepts in External Fixation, Grune & Stratton Philadelphia, PA: 279-291.
- BOOKSTEIN, F. L., 1979. Fitting conic sections to scattered data. Computer Graphics and Image Processing **9**(1): 56-71.
- BRIDWELL, K. 2010. Spinal Curvature Problems: Fixed Sagittal Imbalance. Retrieved 18.06.2015, from <http://www.spineuniverse.com/conditions/kyphosis/spinal-curvature-problems-fixed-sagittal-imbalance>.

- CANNY, J., 1986. A computational approach to edge detection. *Pattern Analysis and Machine Intelligence, IEEE Transactions on*(6): 679-698.
- ÇAKMAK, M., KOCAOĞLU, M, 1999. Ilizarov cerrahisi ve prensipleri.
- DOUGHERTY, E. R., LOTUFO, R. A. and SPIE, T. I. S. F. O. E., 2003. Hands-on morphological image processing, SPIE press Bellingham.
- DOYLE, W., 1962. Operations useful for similarity-invariant pattern recognition. *Journal of the ACM (JACM)* **9**(2): 259-267.
- DU, J.-X., WANG, X.-F. and ZHANG, G.-J., 2007. Leaf shape based plant species recognition. *Applied mathematics and computation* **185**(2): 883-893.
- EREN, A. and ERALP, L., 1999. Ilizarov sisteminin dünyada ve Türkiye'deki gelişimi. Çakmak M, Kocaoğlu M, editörler. Ilizarov cerrahisi ve prensipleri. İstanbul: Doruk Grafik: 1-4.
- FERNÁNDEZ, A., 1985. External fixation of the leg using unilateral biplanar frames. *Archives of orthopaedic and traumatic surgery* **104**(3): 182-186.
- FITZGIBBON, A., PILU, M. and FISHER, R. B., 1999. Direct least square fitting of ellipses. *Pattern Analysis and Machine Intelligence, IEEE Transactions on* **21**(5): 476-480.
- GLASBEY, C. A., 1993. An analysis of histogram-based thresholding algorithms. *CVGIP: Graphical models and image processing* **55**(6): 532-537.
- GOUGH, V. and WHITEHALL, S., 1962. Universal tyre test machine. Proc. FISITA 9th Int. Technical Congress.
- HASKELL, A., 2014. External Fixator Deformity Correction Systems and Methods, Google Patents.
- HUANG, L.-K. and WANG, M.-J. J., 1995. Image thresholding by minimizing the measures of fuzziness. *Pattern recognition* **28**(1): 41-51.
- HUGHES, J. and SAUER, B., 1982. Wagner apparatus: A portable traction device. *Concepts in External Fixation. Gruñe & Stratum. New York.*
- ILIZAROV, G., 1992. *Transosseous osteosynthesis* Springer-Verlag, Heidelberg.
- KAPUR, J. N., SAHOO, P. K. and WONG, A. K., 1985. A new method for gray-level picture thresholding using the entropy of the histogram. *Computer vision, graphics, and image processing* **29**(3): 273-285.

- KARIDIS, J. P., 2009. Fixator apparatus with radiotransparent apertures for orthopaedic applications, Google Patents.
- KARIDIS, J. P. and STEVENS, P. M., 2009. Adjustable length strut apparatus for orthopaedic applications, Google Patents.
- KITTLER, J. and ILLINGWORTH, J., 1986. Minimum error thresholding. *Pattern recognition* **19**(1): 41-47.
- KOO, J. K., HAN, J. S., HAN, C. S., CHOI, I. H., SIM, H. J., PARK, B. S., KIM, J. S., KIM, B. S., KIM, K. T. and SHIN, C. S., 2002. Frame fixator and operation system thereof, Google Patents.
- KUFFNER, J., NISHIWAKI, K., KAGAMI, S., KUNİYOSHI, Y., INABA, M. and INOUE, H., 2002. Self-collision detection and prevention for humanoid robots. *Robotics and Automation, 2002. Proceedings. ICRA'02. IEEE International Conference on*, IEEE.
- LI, C. and TAM, P. K.-S., 1998. An iterative algorithm for minimum cross entropy thresholding. *Pattern Recognition Letters* **19**(8): 771-776.
- LIU, Y. and DONG, X., 2010. Constrained least squares fitting of ellipse. *Computational Intelligence and Software Engineering (CiSE), 2010 International Conference on*, IEEE.
- MILLER, A. T. and ALLEN, P. K., 2004. Graspit! a versatile simulator for robotic grasping. *Robotics & Automation Magazine*, IEEE **11**(4): 110-122.
- MOESLUND, T. 2009. Canny Edge Detection. Retrieved 25.04.2015, from <http://www.cse.iitd.ernet.in/~pkalra/csl783/canny.pdf>.
- ORTHO, R. 2015. Smart Correction® Computer Assisted Circular Hexapod Fixator. Retrieved 17.06.2015, from <http://www.responseortho.com/products/external-fixators/smart-correction-hexapod-fixator/>.
- ORTHOFIX. 2015. Orthofix. Retrieved 27.06.2015, 2015, from <http://www.orthofix.it/>.
- OTSU, N., 1979. A threshold selection method from gray-level histograms. *IEEE Transactions on Systems, Man and Cybernetics* **9**(1): 62-69.
- PALEY, D., 2002. Principles of deformity correction, Springer.

- PALEY, D., 2011. History and science behind the six-axis correction external fixation devices in orthopaedic surgery. *Operative Techniques in Orthopaedics* **21**(2): 125-128.
- PALEY, D. 2015. The history of external fixation. Retrieved 09.07.2015, 2015, from http://limblengtheningdoc.org/history_of_external_fixation.html.
- PARKHILL, C., 1983. A New Apparatus for the Fixation of Bones after Resection and in Fractures with a Tendency to Displacement: With Report of Cases. *Clinical Orthopaedics and Related Research* **180**: 3-6.
- PAUL, G. W., 2003. The history of external fixation. *Clinics in podiatric medicine and surgery* **20**(1): 1-8.
- PIZER, S. M., AMBURN, E. P., AUSTIN, J. D., CROMARTIE, R., GESELOWITZ, A., GREER, T., TER HAAR ROMENY, B., ZIMMERMAN, J. B. and ZUIDERVELD, K., 1987. Adaptive histogram equalization and its variations. *Computer vision, graphics, and image processing* **39**(3): 355-368.
- POPE, M. and EVANS, M., 1982. Design considerations in external fixation. *Concepts in External Fixation*, Grune and Stratton New York: 109-135.
- PREWITT, J. M. and MENDELSON, M. L., 1966. The analysis of cell images. *Ann. NY Acad. Sci* **128**(3): 1035-1053.
- RIDLER, T. and CALVARD, S., 1978. Picture thresholding using an iterative selection method. *IEEE transactions on Systems, Man and Cybernetics* **8**(8): 630-632.
- ROBERT FISHER, S. P., ASHLEY WALKER, ERIK WOLFART 2004. *Hypermedia Image Processing Reference*. Retrieved 28.04.2015, from <http://homepages.inf.ed.ac.uk/rbf/HIPR2/erode.htm>.
- ROSIN, P. L., 1999. Further five-point fit ellipse fitting. *Graphical Models and Image Processing* **61**(5): 245-259.
- ROSS, J. D., SAMCHUKOV, M. L., CHERKASHIN, A. M. and BIRCH, J. G., 2013. External fixator strut, Google Patents.
- SAALFELD, S. 2010. Enhance Local Contrast (CLAHE). Retrieved 28.04.2015, from http://fiji.sc/wiki/index.php/Enhance_Local_Contrast_%28CLAHE%29.

- SAHLAR, M. O., 2010. Library Based Image Reconstruction on X-ray Films for External Fixator Automation MSc. Thesis, Çukurova University.
- SAMET, H. and TAMMINEN, M., 1988. Efficient component labeling of images of arbitrary dimension represented by linear bintrees. *Pattern Analysis and Machine Intelligence, IEEE Transactions on* **10**(4): 579-586.
- SELIGSON, D. and POPE, M., 1982. Concepts in external fixation, Grune and Stratton.
- SHANBHAG, A. G., 1994. Utilization of information measure as a means of image thresholding. *CVGIP: Graphical Models and Image Processing* **56**(5): 414-419.
- SISK, T. D., 1983. External Fixation: Historic Review, Advantages, Disadvantages, Complications, and Indications. *Clinical Orthopaedics and Related Research* **180**: 15-22.
- SMITH&NEPHEW. 2015. What is the TAYLOR SPATIAL FRAME. Retrieved 18.06.2015, from <http://www.smith-nephew.com/patient/treatments/limb-restoration/what-is-the-taylor-spatial-frame-----/>.
- SOILLE, P., 2004. Morphological image analysis: principles and applications, Springer-Verlag New York, Inc.
- SOLOMIN, L. N., UTEKHIN, A. I. and VILENSKIY, V. A. 2015. ORTHO-SUV - Art of Deformity Correction. Retrieved 27.06.2015, 2015, from <http://ortho-suv.org>.
- SPIEGELBERG, B., PARRATT, T., DHEERENDRA, S. K., KHAN, W. S., JENNINGS, R. and MARSH, D. R., 2010. Ilizarov principles of deformity correction. *Annals of The Royal College of Surgeons of England* **92**(2): 101-105.
- STEWART, D., 1965. A platform with six degrees of freedom. *Proceedings of the institution of mechanical engineers* **180**(1): 371-386.
- STREINU, I., 2000. A combinatorial approach to planar non-colliding robot arm motion planning. *Foundations of Computer Science, 2000. Proceedings. 41st Annual Symposium on, IEEE*.

- TAKATA, M., VILENSKY, V. A., TSUCHIYA, H. and SOLOMIN, L. N., 2013. Foot deformity correction with hexapod external fixator, the Ortho-SUV Frame™. *The Journal of Foot and Ankle Surgery* **52**(3): 324-330.
- TANG, P., HU, L., DU, H., GONG, M. and ZHANG, L., 2012. Novel 3D hexapod computer-assisted orthopaedic surgery system for closed diaphyseal fracture reduction. *The International Journal of Medical Robotics and Computer Assisted Surgery* **8**(1): 17-24.
- TASARIMMED. 2015. Spider Frame® Bilgisayar-Destekli Dairesel Eksternal Fiksator. Retrieved 18.06.2015, from <https://www.spiderframes.com/anasayfa>.
- TAYLOR, H. S. and TAYLOR, J. C., 2000. Six axis external fixator strut, Google Patents.
- TAYLOR, J. C., AUSTIN, G. E. and TAYLOR, H. S., 1999. Method of using an orthopaedic fixation device, Google Patents.
- TSAI, W.-H., 1985. Moment-preserving thresholding: A new approach. *Computer Vision, Graphics, and Image Processing* **29**(3): 377-393.
- WIKIPEDIA. 2015, 03.02.2015. Adaptive histogram equalization. Retrieved 28.04.2015, from http://en.wikipedia.org/wiki/Adaptive_histogram_equalization.
- YEN, J.-C., CHANG, F.-J. and CHANG, S., 1995. A new criterion for automatic multilevel thresholding. *Image Processing, IEEE Transactions on* **4**(3): 370-378.
- ZACK, G., ROGERS, W. and LATT, S., 1977. Automatic measurement of sister chromatid exchange frequency. *Journal of Histochemistry & Cytochemistry* **25**(7): 741-753.
- ZHOU, P., YE, W., XIA, Y. and WANG, Q., 2011. An improved Canny algorithm for edge detection. *Journal of Computational Information Systems* **7**(5): 1516-1523.
- ZUIDERVELD, K., 1994. Contrast limited adaptive histogram equalization. *Graphics gems IV*. S. H. Paul, Academic Press Professional, Inc.: 474-485.

CURRICULUM VITAE

Ahmet Aydın was born in Antakya, in 1985. He graduated from Osman Ötken Anatolian High School in 2003. He completed his undergraduate education in Electrical and Electronics Engineering Department at Çukurova University in 2007 and received his MSc. degree from the same department in 2009.

He has been working as a research assistant at Electrical and Electronics Engineering Department of Çukurova University since 2007. During this time, he has taken part in national research projects as scholarship holder and international research projects as visiting researcher.

APPENDIX

APPENDIX A: COMMON IMAGE PROCESSING TOOLS

A.1. Contrast Limited Adaptive Histogram Equalization

Histogram equalization is an image processing algorithm utilized to improve the contrast in images. The adaptive histogram equalization methods are different from the ordinary methods such that it computes several histograms in different tiles of the image and uses these histograms to redistribute the illumination values. However, adaptive histogram equalization methods over-amplify noise in homogeneous regions. Contrast-Limited Adaptive Histogram Equalization (CLAHE) is a variant of the adaptive methods that limits the amplification to prevent the over-amplification of the noise (Zuiderveld, 1994).

CLAHE clips the histogram at a predefined level to limit the amplification. The advantage of this method is that, it distributes the clipped values equally among all histogram bins instead of discarding (Figure A.1) (Pizer et al., 1987).

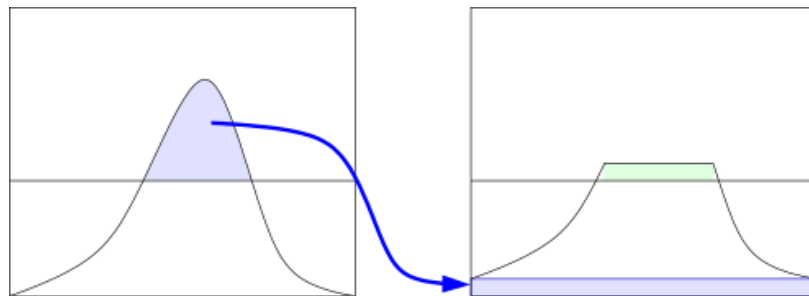


Figure A.1. Redistributing the clipped histogram values among all the bins at CLAHE, (Wikipedia, 2015)

The algorithm has three parameters:

- **Block Size:** It is the size of the local region. The image is divided into blocks in the specified size.
- **Histogram Bins:** This parameter is used for histogram equalization. The images have a maximum of 256 gray levels. If the number of gray levels is less than 256 the pixel intensity values will be grouped into this number.

- **Max Slope:** This parameter limits the contrast in the intensity transfer function. A large value results to a high local contrast and a value of one returns the original image.

The performance of the algorithm on a gray scale test image is shown on Figure A.2. In such images, the algorithm is applied prior to the feature extraction and edge detection algorithms.

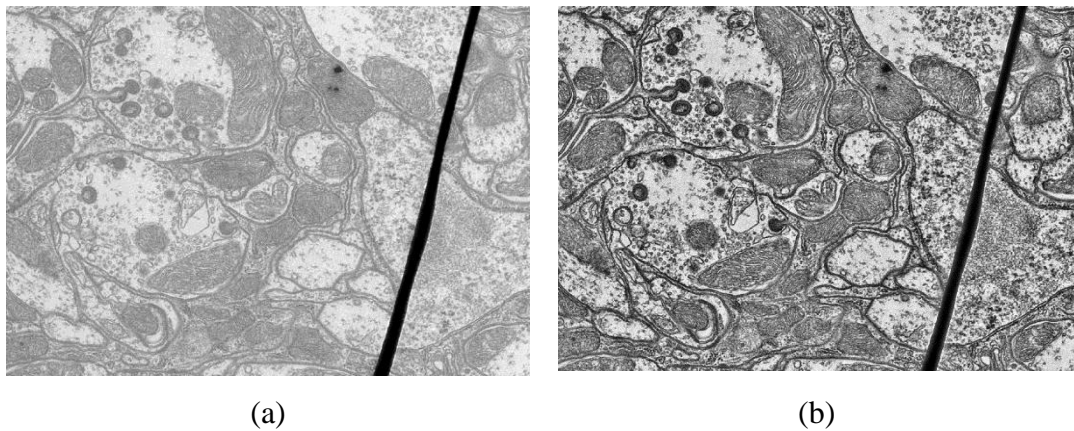


Figure A.2. (a) Input image taken from Transmission Electron Micrograph and (b) after applying CLAHE with 50 block size 256 histogram bins and 2.5 maximum slope (Saalfeld, 2010).

A.2. Canny Edge Detection Algorithm

Edges contains valuable information about the objects and structures in images. Many properties can be obtained from the edges and for most cases edge information reduces the data to be processed. Hence, edge detection is a core algorithm in most image processing software. Canny algorithm is developed by John F. Canny in 1986 and it is one of the most effective edge detection algorithms (Canny, 1986). The algorithm has five steps (Moeslund, 2009):

- i. Gaussian filter is applied to remove noise.
- ii. The intensity gradient of the image is calculated.
- iii. Non-maximum suppression is applied to get rid of false edges.

- iv. Double threshold is applied to the image to determine potential edges.
- v. The weak edges are removed by hysteresis.

Here, the steps ii and iv depend on adjustable parameters. The Gaussian filter used for smoothing directly affects the result of the algorithm. A filter with a smaller kernel results to less blur and consequently allows the detection of thin and sharp lines. A filter with larger kernel results to more blur and allows the detection of larger and smoother edges. That means if the kernel size is smaller than the optimum value some false edges will be found. On the other hand, if the kernel size is larger, some edges will be smoothed with noise. Kernel size is selected experimentally based on the input image.

If the threshold is set too high, some important information might be missed. On the other hand, if it is set too low, some irrelevant information will appear on the output image. Experimental determination of the threshold values for each input image is a difficult task. As an improved version of the canny algorithm, Zhou et. al. (Zhou et al., 2011) used Otsu thresholding method (Otsu, 1979) for optimum selection of the threshold. The result of their study suggest that, the upper border of the threshold must be selected as Otsu threshold (T_H) and the lower border must be half of that value ($T_L = 0.5 * T_H$).

A.3. Morphological Erosion

Erosion is one of the core operators in mathematical morphology. It is mostly applied to binary images, but there are some variants which can be used for grayscale images. In the binary images, all pixels can only take two different values, namely 0 or 1. The pixels with a value of 1 form the *foreground* and the ones with a 0 value form the *background* object. The main operation of the morphological erosion is eroding the foreground pixels and as a result of this operator, the foreground object will be smaller and background holes will be larger (Dougherty et al., 2003).

The morphological erosion takes two inputs; the binary image to be processed and a structure element (also known as *kernel*). The structure element is a matrix which

is smaller than the input image. It consists of 1's and 0's and these entries can form any pattern (Figure A.3). The origin of the structure element is defined prior to the operation.

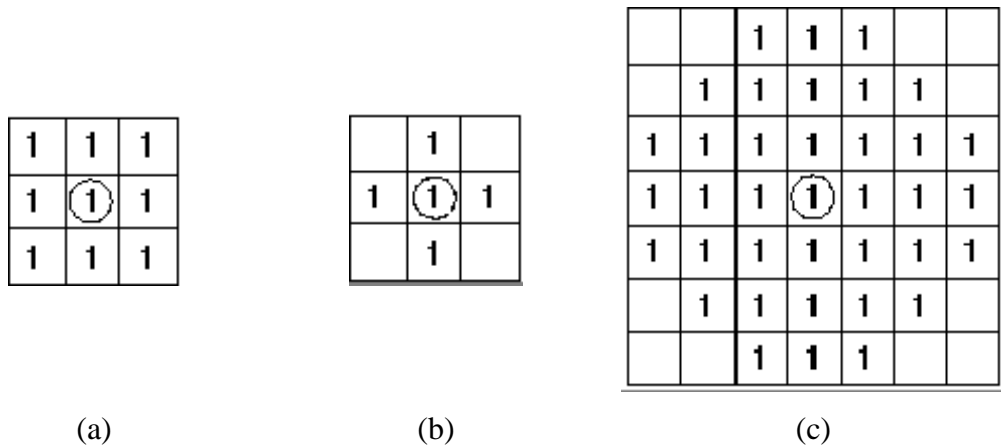


Figure A.3. Different structure elements with their origin is in the center. (a) 3x3 Square, (b) 3x3 Star and (c) 7x7 Disk structure element.

In this method, the structure element is convolved through the image. If the structure element matches with all pixels in the current position of the input image; the pixel in the current position is set to 1 for the output image. If not, it is set to 0.

As an example (Figure A.4), an image is processed with a 3x3 square structure element (Figure A.3(a)).

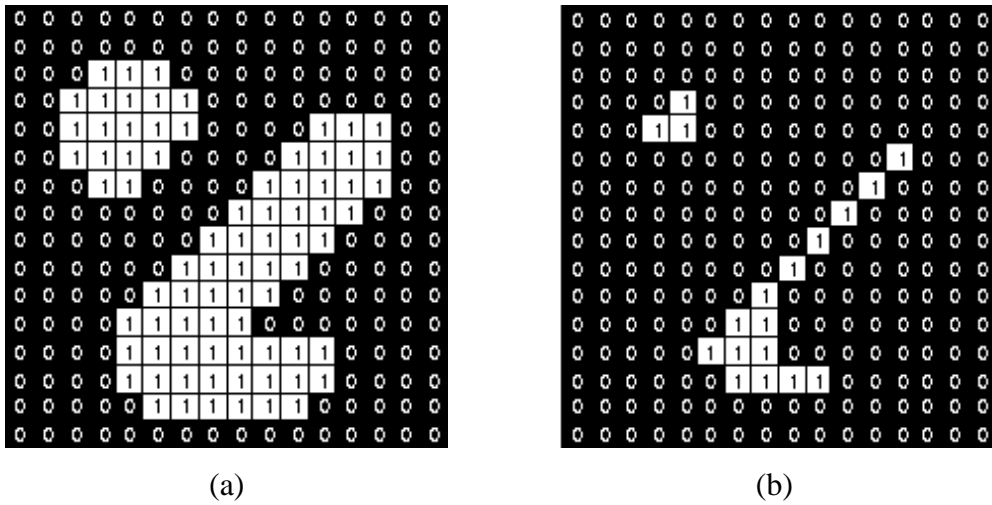


Figure A.4. (a) Binary input image and (b) the output after erosion with 3x3 Square structure element (Robert Fisher, 2004)

A.4. Removing Small Objects in a Binary Image

In some cases, the size of the pixel clusters is important in some problems and needs to be calculated. For binary images, connected component analysis is used to identify the pixel clusters (Samet and Tamminen, 1988). Different properties such as area, perimeter, bounding box, orientation etc., can be calculated for the identified clusters. By analyzing these properties, some pixel clusters can be deleted while others kept.

In this thesis, the area property of the pixel clusters is used mostly. For example, if only the pixel clusters related with the bone fragments are to be kept, the pixel clusters smaller than a predefined value are removed.